Doctoral Dissertation

p-electron Magnetism in Alkali-metal Superoxides probed by μSR

(μSR で探るアルカリ金属超酸化物の p 電子磁性)

Fahmi Astuti

Department of Condensed Matter Physics

Graduate School of Science, Hokkaido University

March 2019

Acknowldegment

It's hard to believe that I have finished my PhD for 3 years already. But time moves, so do we. It is therefore; time to thank the many helpful individuals that have played an important part, directly and indirectly, in the successful completion of my thesis. It fills me with immense pleasure to be able to express my gratitude.

First, I choose to express my sincere gratitude to my supervisor Isao Watanabe. I thank to his support and kindness. When I came to Japan for the first time, I have not enough knowledge especially on μSR technique. He taught me a lot of think about physics and measurement technique so that I can improve my experimental skills. On a more personal level, I enjoyed visiting UK and Switzerland for doing μSR experiment. I did not imagine before that I can perform my own experiment in such a big facility in the world like PSI and ISIS muon facilities. I am very thankful to him for all his help and support during my PhD.

Second, I thank Prof. Takashi Kambe from Okayama University for giving me permission to do sample synthesis in his laboratory and allowing me to use MPMS and XRD machine. My thanks giving also goes to his students, Mizuki Miyajima and Takeshi Kakuto. They help me so much during sample synthesis. I am very fortunate to meet you all and would like to thank all for your support. I also thank Dr. Takehito Nakano for the fruitful comments.

I want to express my gratitude to the various instrument scientist at the different facilities, which made possible most of the experiments relevant for this thesis. They are Dr. Jean Christophe Orain at the Swiss muon source SμS, Paul Scherrer Institut, Switzerland, and Dr. Majed A. Jawad, Dr. Adam Berlie and Dr. James Lord at the RIKEN-RAL and the STFC-ISIS Muon Facility, UK. I am grateful for the provision of beam time at both facilities.

I would like to express my gratitude to Prof. Masahiko Iwasaki for giving me the opportunity to join in his laboratory, Meson Science Laboratory at RIKEN. I thank to Mrs. Yoko Fujita, Mrs. Mitsue Yamamoto, Ms. Tomoko Iwanami and Mrs. Noriko Asakawa for their kind help and supports.

I acknowledge Lembaga Pengelola Dana Pendidikan (LPDP) Indonesia for the financial support on my doctoral study in Japan and Junior Research Associate (JRA) program for the research support at RIKEN.

Thanks to all of my labmates in RIKEN: Kak Aina, Kak Akin, Retno, Dita, Pak Darwis, Mas Irwan, Julia, Harison, Redo, Suci and Tami. Because all of you, I felt like Japan is my second home country. Last but not least, my father, my mother, my sisters and my brothers. Thanks for your support and encouragement.

Contents

Chapter 1
Introductions

1.1. Magnetism in p-electron system and Its properties

In the field of magnetism, nature has been fascinating us by revealing new materials with potential scientific and technological applications. Moreover, unexpected magnetic compounds are still being discovered frequently. Magnetism in solids and molecules is understood to originate from atoms in that part of the periodic table where a particular value on the angular momentum appears first, for instance: the 2p, 3d and 4f series. The vast majority of magnetic materials that have been widely studied are materials containing 3d and 4f cations associated with elements in either the transition metal or rare earth series of the periodic table. Magnetic materials arise from 2p-electrons has been much less explored than those containing magnetic d- or f-series. This is largely due to the limited number of examples of such materials; 2p-electrons tend to be paired in covalent bonds and a strong tendency toward valence electron delocalization. However, further dicoveries of 2p-electron magnetism are currently taking place.

Unpaired p-electrons can show novel magnetic properties which are sometimes different from those observed in other systems which contain local magnetic moments at ionic positions. Properties such as extremely high magnetic ordering temperatures and stable quantum states can thus be expected, with possible applications in devices such as in quntum computing and spin transistors [1]. Typical examples to show the p-electron magnetism are organic molecular magnets which are consists of light elements. Mainly, it referred to organic radicals, that is, systems with unpaired electron that contain carbon atoms. Almost all the organic compounds are comprised of even number of electrons and covalent bonds are formed with two pieces of electron in a pair. Accordingly, the magnetic moments of the electrons in each pair compensate each other resulting in diamagnetism. There are, of course, exceptional compounds called free radicals that are comprised of odd number of electrons and exhibit the magnetism caused by the spin of an unpaired electron. The first discovery of the organic magnet, p-NPNN, shows ferromagnetic transition at 0.65 K opening this research field [2]. After that, more organic molecular magnets with different basic molecules are discovered [3,4].

Compared to those organic molecular magnets, there are less inorganic molecular system which possess the p-orbital magnetism. One typical example is molecular oxygen (see

the detail in Chapter 1.2) which orders antiferomagnetically at ~24 K and becomes superconductor at high pressure and low temperature [5]. According to valence shell electron pair repulsion theory (covalent bonds which are shown in Lewis structure), O_2 has no unpaired electrons but according to molecular orbital theory it does have unpaired electrons.

Further discovery of 2p-electron magnetism is currently taking place in alkali-metal superoxide. Inorganic radicals such as superoxide are now appearing in dedicated studies. This material is a kind of magnetic system in which the magnetic moment is carried exclusively by the p-electrons of the oxygen anions. Detailed discussions on the magnetic properties of the alkali-metal superoxides (AO_2; A = Na, K, Rb, Cs) started in the late 1960's [6]. Following earlier reports, authors started to correlate the magnetism with the crystallographic properties of the materials [7,8]. Alkali-metal superoxides (AO_2) are interesting materials to study in terms of their magnetic properties. The unpaired electron located in the antibonding molecular orbital of the superoxide anion is responsible for the magnetic moment in this class of materials. There were several reports in the past confirming the structural phase transition from diffraction data [8,9,10,11]. Further investigations have been performed to understand magnetic ordering in this class of compounds and its relation to the structural phase transition, for instance: magnetic susceptibility [10,12,13], heat capacity [14] electron paramagnetic resonance (EPR) and antiferromagnetic resonance (AFMR) [15,16,17], nuclear paramagnetic resonance (NMR) [18] and elastic neutron scattering [6]. Morover, both the structural transition temperature together with its low-temperature structure and the magnetic ground state are still under debate.

Several magnetic interactions are active in solids including AO_2. Spin interactions on longer length scales result in magnetic order. Strong spin interactions can generate long-range (3D) ordered arrangements of spins. At temperatures lower than an antiferromagnetic or ferromagnetic ordering temperature, neighbouring magnetic moments in solids are always coupled to give long range ordering (LRO) by exchange interactions. Direct exchange and superexchange are thought to play the main roles in the magnetic exchange interactions of AO_2. Direct exchange requires the direct overlap of orbitals on neighboring magnetic atoms. In this case, the exchange interaction proceeds directly without the need for an intermediary. Superexchange can be defined as an indirect exchange interaction between non-neighboring magnetic ions which is mediated by a non-magnetic ion which placed in between the magnetic ions [19].

In the absence of long-range order, short-range order (low-dimensional magnet) 1D or 2D can be existed. Experimental observations of low-dimensional magnetic systems are usually marked by a broad peak in the magnetic susceptibility or heat capacity versus

temperature curve [20,21]. It is well-known that an ideal 1D spin chain system does not show LRO above T= 0 K due to strong quantum spin fluctuation and often display exotic behavior which lead to a dimerized spin-singlet state with a finite energy gap as in $CuGeO_3$, TTF-CuBDT and $MEM(TCNQ)_2$ [22,23,24]. Those three systems are examples of spin gapped quantum magnet. Spin gap antiferromagnetic have spin-disordered ground states. The ground states, in the absence of LRO, is favoured by quantum fluctuations, the effect of which is prominent in low dimensions and for low values of the spin. In experiments, the presence of the gap Δ is confirmed through measurement of quantities like the susceptibility, χ, which goes to zero exponentially at low T as $\chi \sim \exp\left(\frac{\Delta}{k_B T}\right)$ [25]. The structural phase transition is also observed in some spin gap systems due to the lattice dimerization [24]. However, almost quasi-one-dimensional spin systems display LRO at their ground states due to weak interchain interaction because there might be small interchain interaction which can couple the chains together [26,27]. In other cases, the absence of LRO in some materials can be due to the competing interactions which can lead to a number of different ground states including: spin liquid [28], spin ice [29], spin glasses [30] etc.

The low dimensionality and the interplay between spin, orbital and lattice degrees of freedom yield a variety of fascinating phenomena like superconductivity, quantum liquid and spin gap states. AO_2 is a candidate of the system which has mechanism of the interplay between the spin, orbital and lattice degrees of freedom results in intricate physics related to reorientation of O_2^- molecular p-orbitals (see the detail in Chapter 1.3). Moreover, some AO_2 system also show the presence of low dimensionality making this system is interesting to be studied. A prototype system is CsO_2, where, similar to the Cu^{2+} compound $KCuF_3$, a quasi-one-dimensional magnetic ordering was observed, which is driven by orbital ordering [26]. The orbital ordering involves a reorientation of the molecular anions, which is an important degree of freedom in molecular anionic p-electron systems. We point out that our results provide a well-defined starting point for further investigations of spin, lattice and orbital degrees of freedom in a class of p-electron system which is a very interesting issue in condensed matter physics. The interplay between spin, orbital and lattice degrees of freedom yield a variety of fascinating magnetic phenomena.

1.2. Study on Magnetism in Molecular Solid System

1.2.1. Magnetism in Solid Oxygen

Molecular oxygen has attracted significant interest as a ubiquitous but exotic molecular magnet since Faraday discovered that it is paramagnetic in 1850 [31]. Molecular oxygen, O_2, forms a diatomic molecule with a bond length of 1.21 Angstrom. When two oxygen atoms bind, the individual 1s, 2s and 2p orbitals combine to molecular σ and π orbitals, where the π* orbital contains two electrons. According to Hund's rule, the two spins combine in the ground state to be S=1 which makes O_2 paramagnetic with a magnetic moment of formally $2\mu_B$. In condensed oxygen, the exchange interaction between oxygen molecules develops and contributes to the cohesive energy in addition to the van der Waals force. O_2 molecules are crystallized at low temperatures (*henceforth called solid oxygen*). As is typical for a Van der Waals solid, the magnetic interactions and crystal structure of solid oxygen are closely linked [32]. At atmospheric pressure, it has three phases (γ, β and α) with different magnetic and crystal structures [33, 34]. High temperature γ solid oxygen (43.5 K up to the melting point T_m=54 K) is a paramagnetic phase. The γ-β transition occurs at 43.5 K because of the ordering of the molecular axis parallel to the *c*-axis, and the short-range antiferromagnetic correlation develops. Short-range magnetic order (SRO) is indicated by the presence of a weak broad peak in neutron diffraction spectra which does not appear in X-ray diffraction data [35]. The crystal symmetry changes from cubic $Pm3m$ to rhombohedral $R\bar{3}m$. From μSR, V. Storchak et al. reported the absence of any magnetic ordering in β-phase of solid oxygen [36].

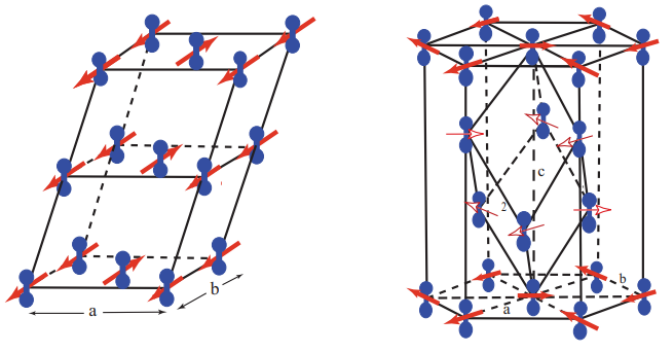

Figure 1.1. Crystal structure of solid oxygen in α- and β-phase. The arrows represent the spin stucture [37].

As the temperature is reduced further, the β-α transition occurs at 23.5 K in where crystal transforms from rhombohedral $R\bar{3}m$ to monoclinic $C2/m$. The formation of LRO in α-

phase solid oxygen is observed from μSR measurement as shown in Fig. 1.2 (a). From the temperature dependence of magnetic field, the internal field at the ground state is estimated to be $B(0)$= 1257.4 (2) G [32] comparable to the result from V. Strochak et al. [36] that showed abrupt reduction in B in the vicinity of $T_{\alpha\beta}$. It indicates that the ordinary magnetic transition of the second order does not take place in solid oxygen.

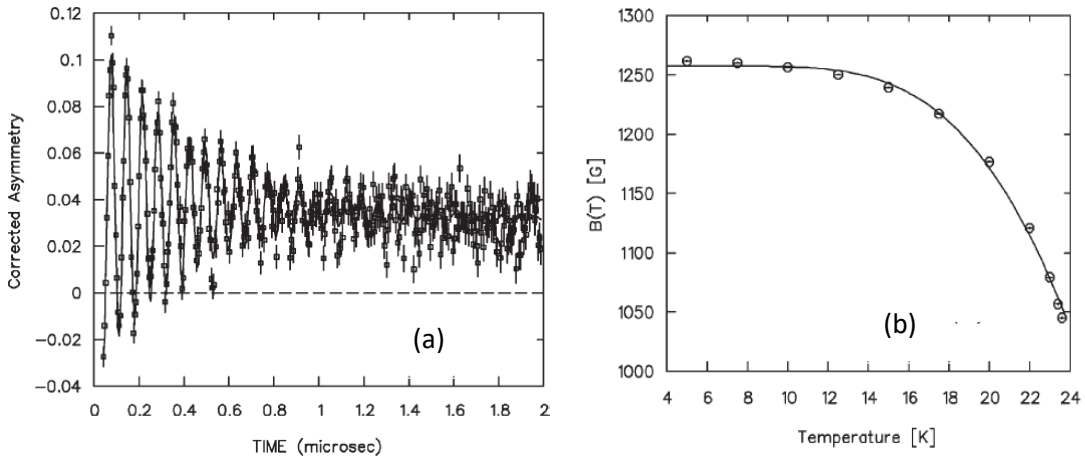

Figure 1.2. (a) Time spectrum of α- O_2 in zero applied magnetic field at T = 20 K measured by μSR (b) Temperature dependence of the magnetic field at the muon site.

Magnetization measurements of the solid oxygen have been performed up to 50 T [38]. All solid curves are linear except the low-field region in the α-phase and the non-linearity below 100 kOe (shown in Fig. 1.3 (a)) comes from the spin flop phenomenon expected in antiferromagnets. Fig. 1.3(b) shows the isothermal derivative magnetization

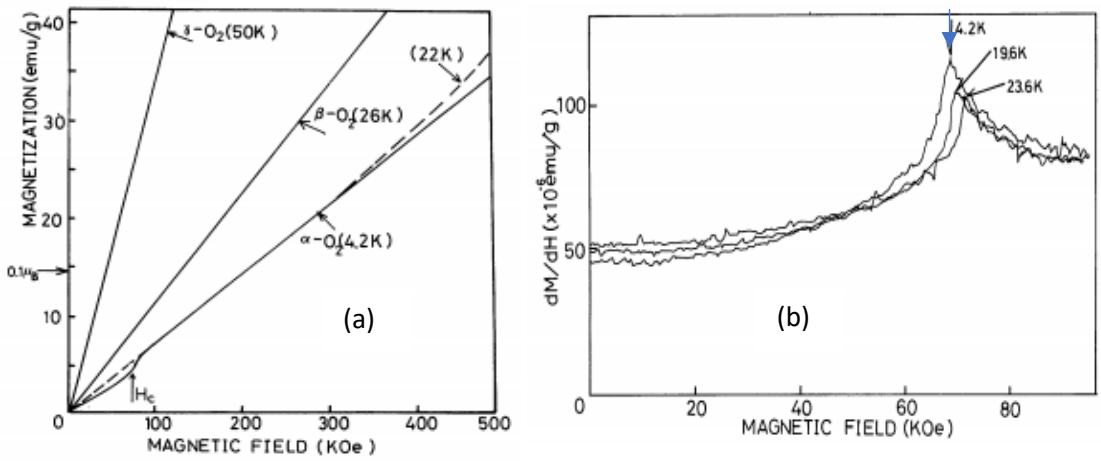

Figure 1.3. (a) Magnetization curves of oxygen in three phases (b) dM/dH curves of oxygen in the α-phase (arrows show H_c at each temperature) [38]

data, dM/dH, as a function of magnetic field at temperatures around T_N. Clear anomalies around 70 T (arrows in the Fig. 1.3 (b)) are observed which get shifted to higher fields with increasing temperatures. Current results on high-field magnetization in α-phase solid oxygen indicated that an abrupt increase in magnetization with large hysterisis was observed when pulsed magnetic field greater than 120 T were applied [39]. As shown in Fig. 1.4, the magnetization jumps at 125 T in the up sweep and 72 T in the down sweep are reproducible. This finding clearly shows that the field-induced phase transition takes place ultrahigh magnetic field greater than 120 T. The pronounced behavior suggests that the phase transition is first order. Because of the strong spin-lattice coupling, solid oxygen is regarded as a spin-controlled crystal [40]. Solid oxygen shows various transition from antiferromagnetism to superconductivity under a high pressure [5, 41,42].

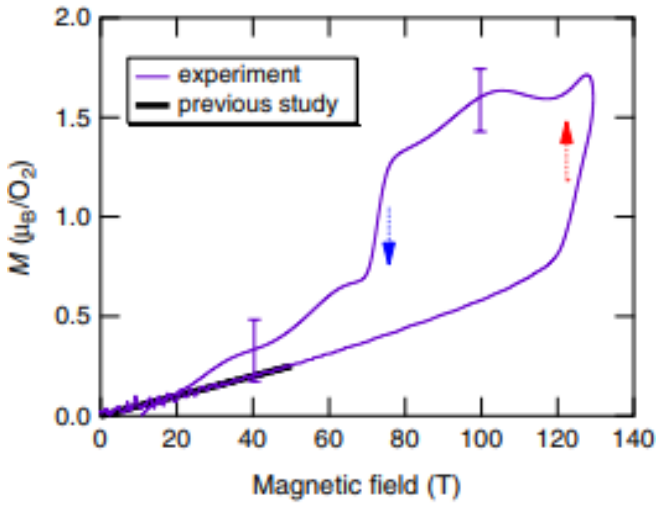

Figure 1.4. Magnetization curve of the α-phase solid oxygen under ultrahigh magnetic field. Distinct magnetization jumps are observed in the up (red arrow) and down (blue arrow) sweeps.

Since O_2 is a good oxidizer and can easily take an additional electron when it is brought into contact with alkali elements, there is another way of making crystalline O_2, in the form of ionic crystals [43]. Oxygen has two allotropes, O_2 and O_3 (ozone). Both forms can exist in the anionic state, giving the species superoxide (O_2^-), peroxide (O_2^{2-}) and ozonide (O_3^-) [44]. Those have stability of a bond. For instance, the bond length in the O_2 is 1.21 Angstrom and superoxide ion O_2^- 1.35 Angstrom at ambient pressure [45,46]. It can be understood since the bond order for superoxide O_2^- is lower than O_2. However, ionic compounds containing ozonide, superoxide and peroxide have been relatively little explored.

1.2.2. Superoxide as an Anionic State of Molecular Oxygen

Superoxide represents a class of rare compounds which are suitable for investigation of magnetic ordering phenomena associated with unpaired p-electrons. The superoxide anion O_2^- corresponds to "charged oxygen" [47]. The term "superoxide" prompted several scientists to presume that O_2^- possesses exceptionally high reactivity, particularly as a powerful oxidizing agent and an initiator of radical reactions [48]. Superoxide commonly has a dumbbell-type bonding state of two O atoms with only one unpaired electron on it. Unpaired electrons make free radicals highly reactive. Of interest here is the superoxide, which is stabilized by low valent, non-oxidizable and highly electropositive metallic cations to give ionic salts. Alkali metal cations meet these criteria.

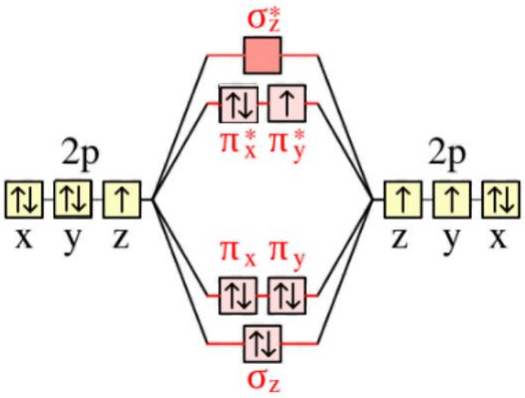

Figure 1.5. Molecular orbital diagram of superoxide.

The name "superoxide" was first proposed for the potassium salt of the radical anion O_2^- in 1934 [49,50]. It was selected because the stoichiometry for KO_2 differed from that for the products of combustion for most metals, e.g., NaOH (hydroxide), Na_2O (oxide), Na_2O_2 (peroxide), NaO_2H (hydroperoxide) and NaO_3 (ozonide). For many years, superoxide was considered to be an interesting chemical curiosity. Ionic salts of superoxide (yellow to orange solids), which generally were formed from the reaction of dioxygen with alkali-metal elements (A) were found to be paramagnetic with one unpaired electron per two oxygen atoms as shown in the molecular orbital diagram in Fig. 1.5.

The paramagnetic properties of the alkali-metal superoxides indicate the presence of an ion containing one unpaired electron (S= ½ system), so that they are correctly represented as ionic compounds of the type $A^+O_2^-$. Atoms have a tendency to achieve a completely filled

valence shell like the inert gases. Metals tend to lose electrons to achieve full valence shells ($A \rightarrow A^+ + e^-$) and nonmetals tend to gain electrons ($O_2 + e^- \rightarrow O_2^-$). The process of gaining or losing electrons crates ions and electrostatic forces bring the ions together to form compounds ($A^+ + O_2^- \rightarrow AO_2$). The attraction between the oppositely charged ions constitutes the ionic bond. These superoxides represent the realization of electron-doped oxygen molecules (O_2^-) arranged in a lattice. The alkali-metal atom A (Na, K, Rb, and Cs) acts as an electron donor. Each O_2^- anion has nine electrons in 2p molecular orbital levels with an electronic configuration of σ^2, π^4, π^{*3}. The alkali-metal atoms transfer their electrons to the oxygen molecules resulting in ionic crystals with dioxygen anions and result in alkali-metal superoxide (AO_2) as a product. The thermodynamic stability of the AO_2 increases with the increasing atomic number of metal due to the stabilization of anions by larger cation through lattice energies [51].

AO_2 are highly reactive compounds. It releases oxygen under heating and on contact with water and air, so it is important to handle these materials in a controlled atmosphere. This material also can be highly flammable if directly exposed to air, so care must be taken at all times. They appear transparent orange or yellow in color [47]. Despite the delicate and sophisticated processes that are required for handling and synthesis due to the sensitivity to air, AO_2 are interesting materials to study in terms of their magnetic properties. The unpaired electron located in the π^* molecular orbital of the superoxide anion is responsible for the magnetic moment in this class of materials.

1.3. Structural Phase Transition induced Magnetism in Alkali-metal superoxides (AO_2)

AO_2 belong to the the system which has mechanism of the intimate interplay between the spin, orbital and lattice degrees of freedom [52,53,54]. Two bonding axis of two oxygen atom of superoxide form oxygen dumbbell as displayed in Fig. 1.6. It has been proposed that electronic and magnetic structures are significantly affected by the relative orientation of O_2^- dumbbell within the crystal structure [55]. Since the magnetic interactions depend sensitively on the reorientation of the O_2^- dumbbell axis, these interactions are strongly affected by the structural phase transitions. In addition to this, those changes in the structure and magnetic properties depend on the alkali-metal ion.

The partially occupied π^* molecular states play the most important role in determining the magnetic properties of alkali-metal superoxides. The degeneracy of the π^* level is expected

to be lifted by lowering the crystal symmetry with decreasing the temperature as shown in Fig. 1.6, as occured due to the Crystal Field such as Jahn-Teller effect [16]. One suggested that the orbital degeneracy of the O_2^- anions in AO_2 is generally lifted by a Jahn-Teller type phase transition where the orientations of the O_2^- dumbbell axis changes. Relativistic spin-orbit coupling (SOC) is also effective in determining the magnetic interaction. Another aspect which can drive the magnetic ordering is the superexchange interaction of the Kugel-Khomskii (KK) within the framework of Goodenough-Kanamori rules [56,57]. The experimentally observed magnetic order thus arises from rather subtle interplay between spin-orbital physics and orbital-lattice coupling.

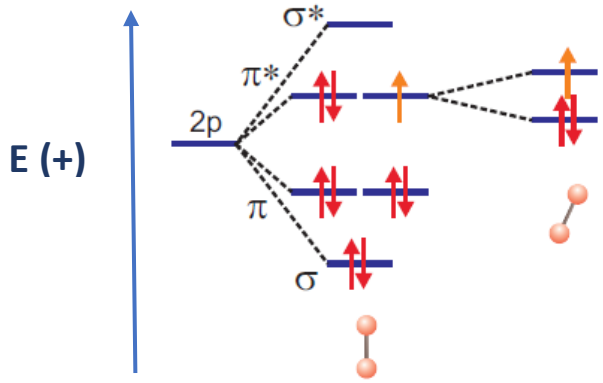

Figure 1.6. Schematic representations of Jahn-Teller effect in AO_2.

1.3.1. Structural Phase Transition in AO_2

In AO_2 system, the unit cell volume depends on the size of the cation. The ionic radius increases with atomic number: $r_{Cs} > r_{Rb} > r_K > r_{Na.}$ The crystal structures of AO_2 are all derived from rocksalt and the orientation of the oxygen dumbbells determines the structure. In case of KO_2, RbO_2 and CsO_2, at room temperature, thermal activation results in precession of the dumbbells around the *c*-axis. Hence, the dumbbell orientation along *c*-axis as shown in Fig. 1.7 is an average structure. Similarly, the structure of NaO_2 at room temperature is attributed to spherical disorder of the superoxide orientations. The low-temperature structures of single crystals of AO_2 have been studied, although details are lacking [8,9,10,11]. All AO_2 show a sequence of crystallographic phase transitions below room temperature. The re-orientation of the dumbbells in AO_2 induces lattice distortion/symmetry change. The driving force for dumbbell reorientation from the cubic (A = Na) or tetragonal phase (A = K, Rb, Cs) is a lowering in energy provided by breaking the degeneracy of the $\pi*$ orbitals of the superoxide anion as ilustrated in Fig. 1.6.

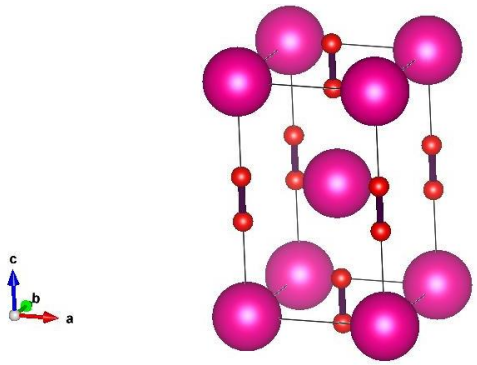

Figure 1.7. Room temperature structure of RbO_2. Rb and O atoms are shown by the violet and the red spheres, respectively.

Above 395 K, KO_2 was found to possess a disordered cubic structure. At room temperature [58], KO_2 crystallizes in the tetragonal structure of CaC_2 type, in which the O_2^- molecular bond axes are parallel to the *c*-axis. KO_2 retains this structure down to 196 K and exhibits the paramagnetic behavior [9].

Table 1.1 High-Symmetry/Temperature and Low-Symmetry/Temperature Structural Parameters of KO_2 [59]

Structural Details	**High-Symmetry/Temp.**	**Low-Symmetry/Temp.**
Space group	$I4/mmm$	$C2/c$
a (Å)	4.030	8.1769
b (Å)	4.030	7.6320
c (Å)	6.697	4.1396
α (∘)	90	90
β (∘)	90	90
γ (∘)	90	62
K	0.0, 0.0, 0.5	0.0, 0.25, 0.8175
O	0.0, 0.0, 0.0975	0.6857, 0.4748, 0.1889

Upon cooling, O_2^- molecular bond axis seem to tilt uniformly by ~20^o to have a lower crystal symmetry to be monoclinic. The magnetic phase is still paramagnetic down to 7 K. Below 7 K, the AFM ordering emerges in the triclinic crystal structure with the uniform tilting O_2^-

molecular bond axes by ~30° [15]. The transition in KO_2 is accompanied by a large distortion of the lattice and a reorientation of the O_2^- molecules, according to paramagnetic resonance.

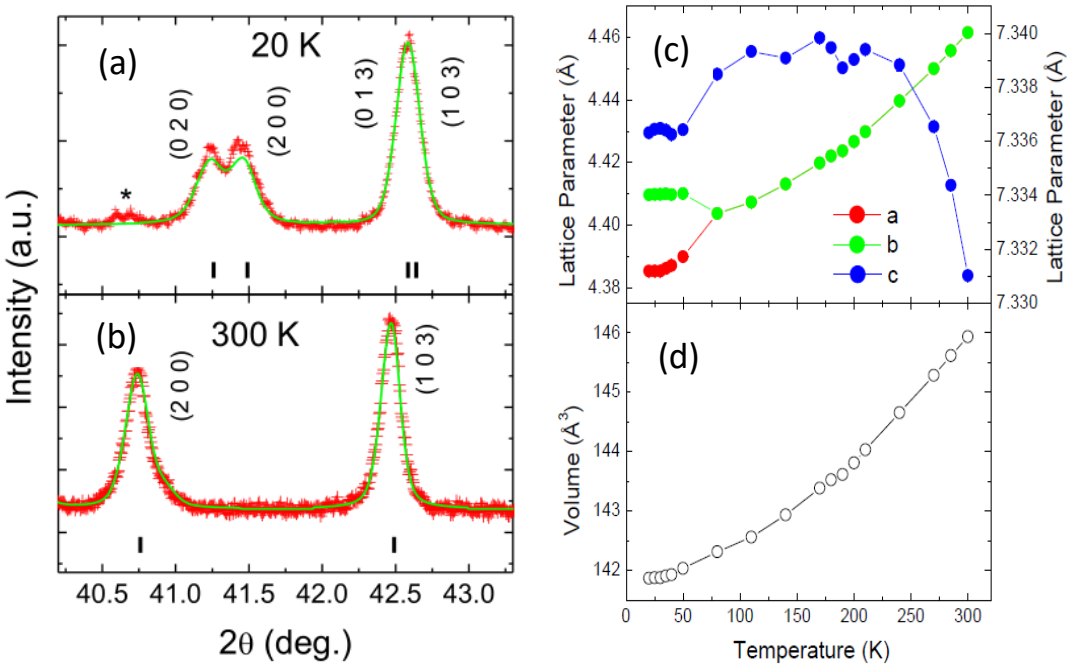

Figure 1.8. Structural phase transition from (b) tetragonal to (a) orthorhombic in polycrystalline CsO_2 observed at 300 K and 20 K using x-ray diffraction (c) The temperature dependence of lattice constant. The transition from tetragonal to orthorhombic structure was occurred at 70 K (d) The evolution of volume with temperature [10].

Hesse et al. also reported the structural phase transition in single crystal CsO_2 and RbO_2 [9]. Those two systems also undergo a series of crystallographic phase transition at low temperatures. Similar to KO_2, the room temperature of CsO_2 and RbO_2 has tetragonal structure (space group *I4/mmm*). In this structure, the superoxide dumbbells are on average pointing in the *c* direction, leading to a longer *c*-axis. The crystal structure of CsO_2 at low temperature is simpler than KO_2. From single crystal x-ray diffraction, it was observed that tetragonal CsO_2 transforms to an orthorhombic phase at 190 K >T>9.6 K. The structure stays orthorhombic into the magnetically ordered phase below 9 K. Another result in powder x-ray diffraction showed the structural phase transition from tetragonal to orthorhombic structure in which the dumbbells are slightly tilted away from the *c*-axis exists at the temperature of ~70 K [10]. Distinct from KO_2, CsO_2 has rather small rotation angles, θ~5° [10]. As shown in Table 1.2 and Fig. 1.8, the estimation of structural phase transition temperature in CsO_2 are unable to reach agreement.

An isostructural compound, RbO_2, has the same tetragonal symmetry with CaC_2-type. The crystal structure of RbO_2 at room temperature is tetragonal as well as the case of CsO_2 and displays some structural transitions with lowering temperatures. It has been proposed that RbO_2 goes into the lower symmetry than that of CsO_2 like the monoclinic one, while the orthorhombic structure was predicted to remain seated in CsO_2 at the ground state [8, 9]. Yet, reflections were observed to be smeared out at low temperatures [8]. This smearing behavior could be due to the sample quality and leaves ambiguity in the determination of the lattice symmetry of RbO_2 at low temperatures. The measurement by using a good quality sample and with a high reliable experimental condition is highly desirable. Besides, the temperature ranges where the transition occur have not been investigated in detail.

Table 1.2. Distinct structural phases of CsO_2

Phase	**Temp. (K)**	**Lattice parameter (pm)**	**Space group/symmetry**	**Structure remarks**
I-CsO_2	378<T	a=662(1) (473 K)	*Fm-3m*	NaCl-type; X-P
II-CsO_2	190<T<378	a=447.7 c= 735.0 (293 K)	Pseudo tetragonal *I4/mmm*	X-SC; X-P
III-CsO_2	190>T>9.6	a=445.7(10) b= 437.0(20) c=733.6(5) (100 K)	Orthorhombic	X-SC
IV-CsO_2	T<9.6	a=446.0(10) b=437.5(50) c= 733.6(5) γ=90.71° (8 K)	Orthorhombic	X-SC
X-P, X-SC: X-ray powder, single crystal diffraction data				

NaO_2 is structurally different from other alkali-metal superoxides. NaO_2, at room temperature is similar to that of sodium chloride. The superoxide ion, O_2^-, is located at the anion position with rotational disorder. The disordered pyrite structure of NaO_2 is attributed to spherical order of the superoxide orientations [60]. NaO_2 transforms to an ordered pyrite (cubic) structure below 223 K (space group *Pa-3*) from disordered pyrite (cubic) at room temperature (*Fm-3m*), in which the superoxide orientations are ordered along [111] directions of the cubic unit cell and further transforms to the orthorhombic marcasite structure below 196 K (space group *Pnnm*) as shown in Fig. 1.9 [9]. Below 43 K, there is a possibility that the structure changes further, but details have not been reported [9].

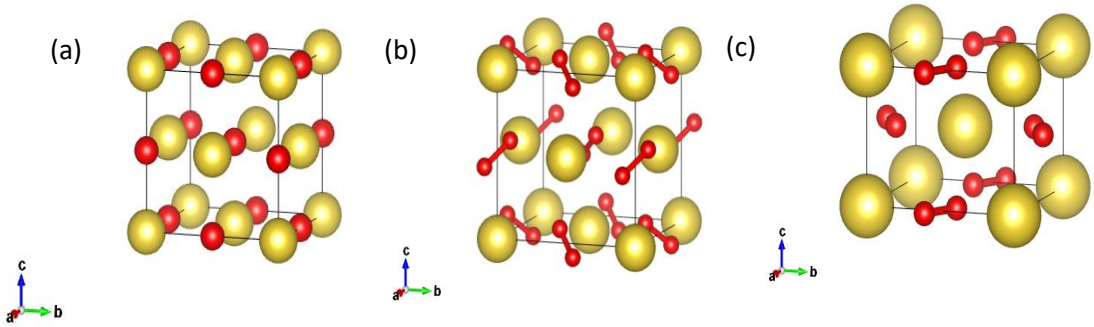

Figure 1.9. Crystal structure of NaO_2 at various temperatures. Na atoms are in yellow and O atoms in red. (a) disordered pyrite, (b) pyrite and (c) marcasite structure.

1.3.2. Magnetic Order and Magnetic Interaction in AO_2

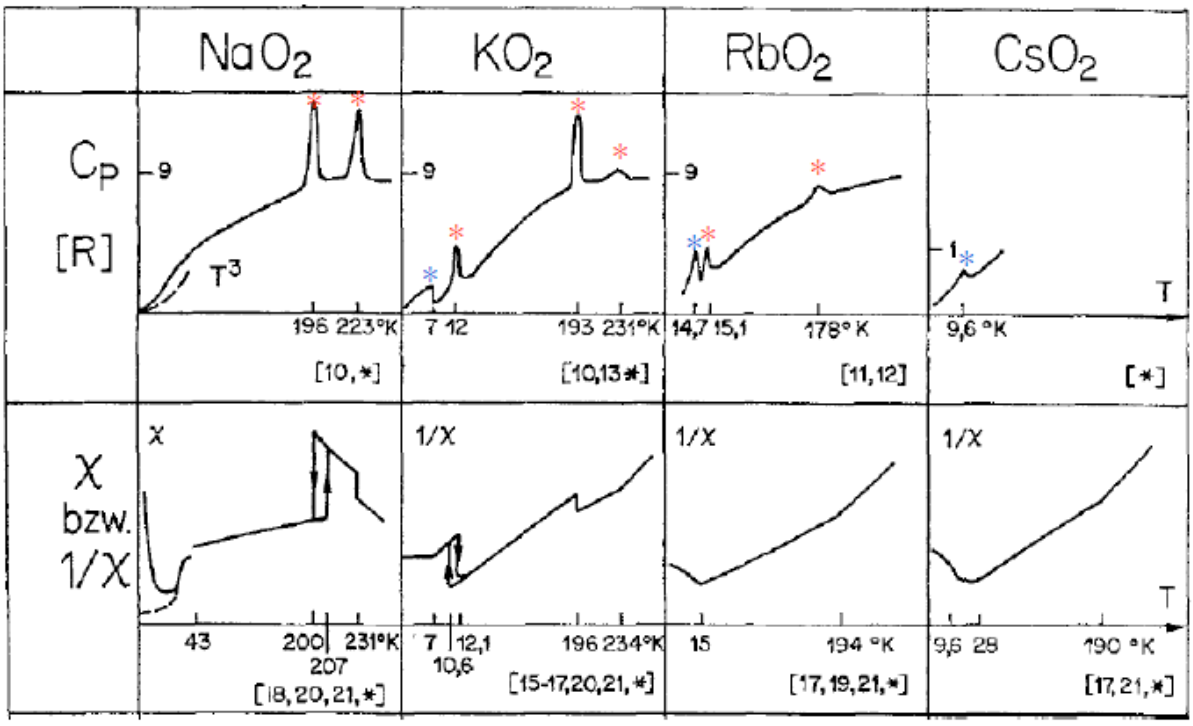

Figure 1.10. (red star) structural phase transition and (blue star) antiferromagnetic phase transition in single crystal AO_2 [12].

Transition metal (TM) compounds and various rare-earth based compounds have been the workhouse of the strongly correlated community over the past five to six decades, with very interesting properties being found as a consequence of closely coupled spin, orbital and lattice degrees of freedom. Recent studies have investigated the implications of closely coupled spin, orbital and lattice degrees of freedom for the class of magnetic materials where magnetism comes from partially filled p-electrons as in AO_2. In case of AO_2, the magnetic interaction was suggested to be strongly depend on the anion orientation. The low temperature structures of AO_2 are strongly correlated with their magnetic properties.

It was suggested that, for single crystal KO_2, the symmetry lowering would occur via coherent tilting of the O_2^- molecular axes called magnetogyration [61]. This O_2^- dumbbell can be reoriented by an external magnetic field, or in case of KO_2 by cooling towards the magnetic ordering transition. The magnetogyric phase transition of KO_2 appears at $T \approx 1.5\ T_N$, where $T_N = 7$ K. It involves a reorientation of the dumbbells such that their half-filled π^* orbitals can overlap the p_z orbitals of K^+ [60], stabilizing 3D antiferromagnetic (AFM) order. Nandy et al [62] proposed that the 3D AFM order is thought to be determined by ordering of half-filled π^*_x and π^*_y orbitals.

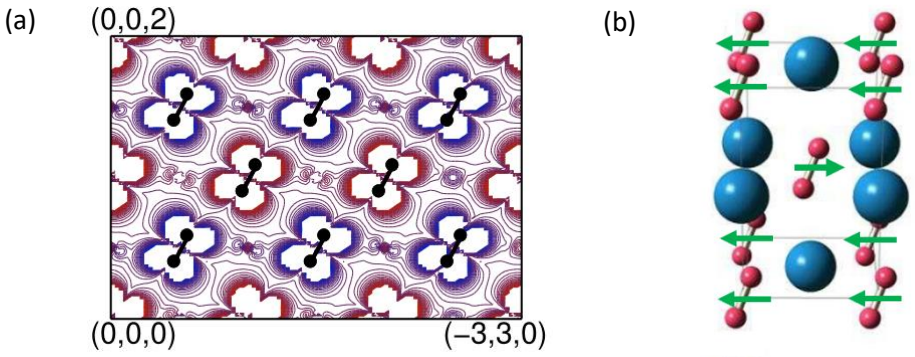

Figure 1.11. (a) The local PDOS for the AFM phase of KO_2 in the triclinic structure. Blue and red colors in the spin densities represent opposite spins plotted on the (110) plane (b) Magnetic spin structure of KO_2 measured by elastic neutron scattering.

According to neutron experiment in KO_2, the observation of AFM was observed at 7 K in which there are ferromagnetic sheets of moments parallel to the (00*l*) planes with adjacent sheets aligned antiparallel [6]. The relative intensities of the reflections suggest that the moments must be oriented in a direction closely parallel to the (00*l*) plane (see Fig. 1.11 (b)). This magnetic structure can be interpreted on the basis of direct magnetic exchange between

neighboring molecule-ions. From calculation work displayed in Fig. 1.11 (a), Kim et al found that with the tilting of O_2^- dumbbell in the AFM structures, the band-gap opening and the ferrro-orbital (FO) ordering occur simultaneously. Kim et al suggested the formation of FO ordering driven by the crystal field from the cations and the Coulomb interaction [63]. Orbital ordering is typically only indirectly observed. Indeed, its principal hallmark is the presence of the co-operative Jahn-Teller distortion itself. The concurrent AFM spin and FO orderings with the band-gap opening clearly demonstrate the strong coupling among spin-orbital-lattice degrees of freedom in KO_2.

In CsO_2, by using combination of experiment and density functional theory (DFT), Riyadi et al [10] suggested that orbital ordering below 70 K drives the formation of a one-dimensional (1D) S=1/2 antiferromagnetic spin chain. Pairs of superoxide π^*_x and π^*_y orbitals are connected via the $5p_z$ orbital of Cs, forming a 1D zig-zag chain of magnetic correlations as shown in Fig. 1.12 (a) and (b).

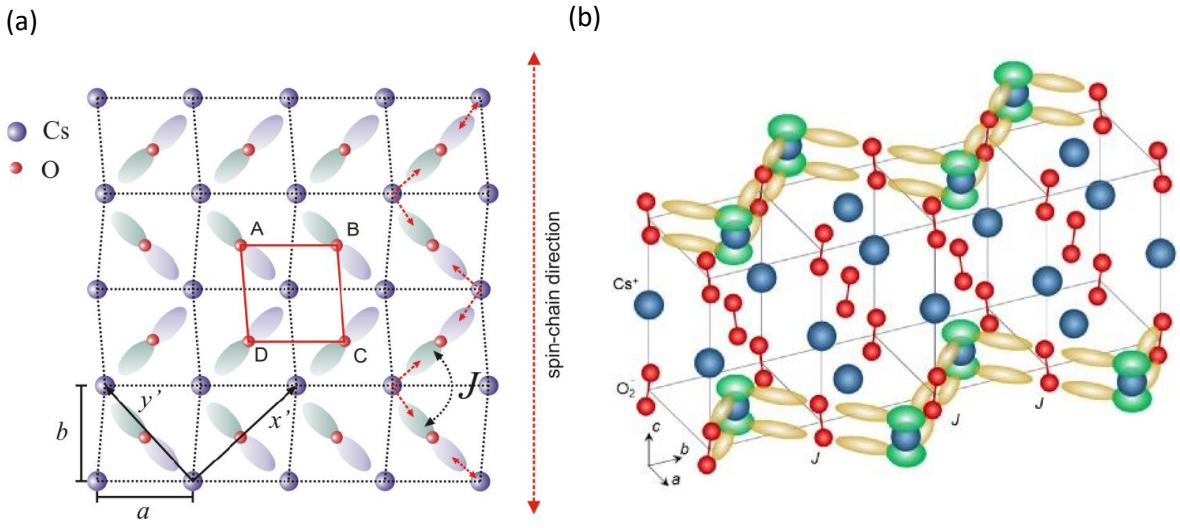

Figure 1.12. (a) ab-plane view of the optimized structure of CsO_2 below 70 K showing anion tilting and ordering of the half-occupied π^*_x and π^*_y orbitals. (b) The magnetic exchange pathway in CsO_2. The superexchange interactions J between $\pi^*_{x,y}$ orbitals (yellow) are bridged by Cs p_z orbitals (green).

The magnetization for CsO_2 as a function of magnetic field up to 60 T at 1.3 K showed the remarkable up-turn curvature around a saturation field (see Fig. 1.13) [64], suggesting the low-dimensional system. The saturated magnetization is also estimated to be $\sim 1\mu_B$ which corresponds to the spin-1/2. The comparison with the theoretical calculation using 1D

Heisenberg numerical calculation including the Bethe ansatz [65] showed some inconsistency because the calculated magnetization did not reproduce the experiments as a whole especially at high field regime.

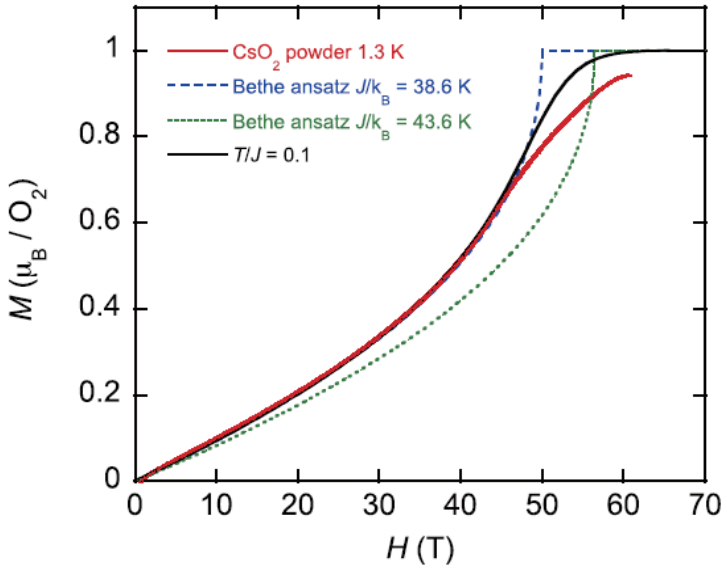

Figure 1.13. High-field magnetization in CsO_2 indicated the formation of low-dimensional nature of this system. A fit with the Bethe-ansatz curve gives the saturation magnetization of H_S = 50 T and J_{1D}/k_B =38.6 K. From this analysis, low-field magnetization can be reproduced by the exact calculation, but in the high-field region, especially around H_S, the high-field magnetization seems to be inconsistent with the calculation. On the other hand, the value J_{1D}/k_B = 42.8 K estimated from the Bonner–Fisher fit the calculated magnetization did not reproduce the experiments completely. The magnetization curve at k_BT/J_{1D} = 0.1 with J_{1D}/k_B = 38.6 K was calculated by using the finite temperature DMRG. The calculation showed a better agreement around the saturation field, but could not reproduce the experiments entirely [64].

This inconsistency may be caused by the interchain coupling and/or XXZ anisotropy. Weak interchain coupling induces three-dimensional 3D AFM LRO at the ground state of almost all actual quasi-1D spin chain systems. In this case, we have potential coupling like Coulomb interaction which introduces scattering of particles on different stacks [66]. In certain conditions, potential coupling may give rise to long range order at finite temperature as observed in some systems [67-71], while an ideal 1D spin chain system does not show long-range ordering above T=0 due to strong quantum spin fluctuation. The one-dimensional chains

cannot display a stable long-range AFM order for $T > 0$. If one considers only the strongest AFM interactions within the chain, according to the Mermin–Wagner theorem [72], there would be no long range magnetic order at finite T. However, as soon as the fluctuations slow down and system become static, the spins are locked into a 3D-order by weak interchain interactions.

It has recently been suggested from a NMR study that the Tomonaga-Luttinger Liquid (TLL) [73,74] state is observed in CsO_2 system [18]. The concept of TLL, which was introduced by Haldane [75] in the early 1980s, encompasses a large class of 1D quantum liquids. The striking feature of the TLL is a power-law singularity [76], zero excitation gap in the charge and/or spin sector, low-energy excitations, spin-charge separation (decoupled movements of charge and spin) in the continuum limit and also a smearing of the Fermi surface [77]. TLL theory provides a powerful, universal description of gapless interacting fermions in one dimension (1D), equivalent to the description that Landau Fermi liquid theory provides in three dimensions [78]. The concept of the TLL is not limited to 1D metals; it also applies to 1D AFM. In a TLL in an antiferromagnet, the gapless point k_0 of the linear dispersion moves with the magnetic field [79] and is related to the magnetization as observed in $Ni(C_9H_{24}N_4)(NO_2)ClO_4$, alias NTENP system [76]. TLL model is exactly solvable within the Bethe Ansatz method, which provides exact results for the energy spectrum and some thermodynamic quantities [80] with interaction-dependent powers determined by Luttinger parameter K (K<1 describes repulsive interaction and K>1 describes attractive interaction) [81], giving the K = 0.25 for NMR measurement in CsO_2 system [18]. Recently, it has been reported, below structural phase transition temperature (~70 K), where antiferromagnetic spin chains are formed as a result of p-orbital ordering, TLL behavior of spin dynamics was observed in CsO_2.

As shown in Fig. 1.14, ^{133}Cs T_1^{-1} (T) data sets measured in three different magnetic fields exhibit the power-law behaviour which is the characteristic of TLL [82]. This behavior is outweighted below ~15 K by the growth of 3D critical fluctuations preceding the antiferromagnetic ordering. TLL model suggested in the CsO_2 supposed to appear a field-induced magnetic order which would be related to the TLL state (see the inset in Fig. 1.14). Complementary analysis from the EPR line shape, linewidth and the signal intensity within the TLL framework allows for a determination of the K= 0.48 in CsO_2 [17]. Since EPR and NMR probe the low energy part of $\chi_{\perp}^{"}(q,\omega)$ in a slightly different way (time window), the features

in the excitation spectrum arising from the effects of interchain couplings may echo differently in EPR and NMR data.

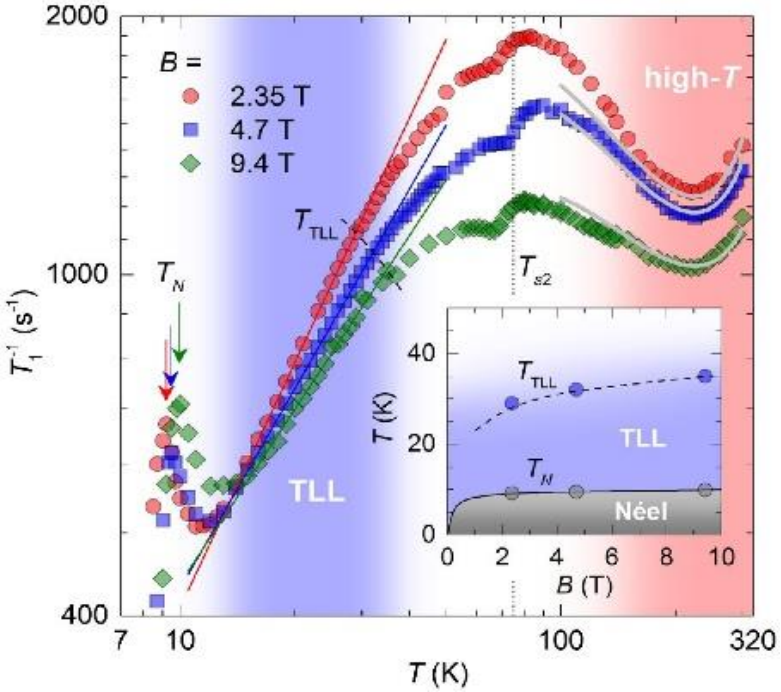

Figure 1.14. Magnetic phase diagram of CsO_2 studied by NMR. Suppression of spin dynamics and TLL behavior were suggested from the NMR result.

Kim et al [59] indicated that underlying physics of CsO_2 and RbO_2 is different from KO_2. The CF due to the O_2 molecular axis rotation in CsO_2 and RbO_2 is not strong enough to induce the FO ordering. In CsO_2 and RbO_2, the rotation angle of O_2 dumbbell is inherently too small to generate the FO ordering. Instead, in CsO_2 and RbO_2 the antiferro orbital ordering (AFO) ordering occurs through the interplay between various interaction effects including the KK-type superexchange, the SOC and cation distortion. From other references, it was reported that staggered AFO along both basal plane axes was calculated to be most favored in RbO_2 [54], whereas in CsO_2 the orbital ordering is of anti ferro along the *b*-axis and ferro character along the *a*-axis [10].

The magnetic ordering temperature of another alkali-metal superoxide, NaO_2, is still under debate. M. Bösch et al reported that NaO_2 has some similarities to a one-dimensional spin-Peierls system [16]. One suggested there is a change over from a weak three dimensional ferromagnetic to a strong one dimensional antiferromagnetic coupling between O_2^- spins [7]. The transition to the low-temperature marcasite phase of NaO_2 below 196 K lifts the degeneracy and might exhibit a spin chain along the *c*-axis due to strong AFM direct exchange

between anions and orbital ordering has not been confirmed [83]. Hesse et al suggested the formation of short range order at the temperature of 43 K<*T*<196 K [9].

Another molecular oxygen based system which also shows peculiar magnetism is alkali sesquioxides (A_4O_6). Sesquioxide is an oxide containing three atoms of oxygen with two atoms (or radicals) of another element. Alkali sesquioxides stand out as unique representatives of p-electron molecular solids. This compound exhibits a mixed valence type of behavior that is caused by differently charged dioxygen molecules, implying that the chemical formula may be written as $A_4(O_2^-)_2(O_2^{2-})$ with diamagnetic peroxide (O_2^{2-}) and paramagnetic superoxide (O_2^-) anions [47]. The presence of both peroxide and superoxide anions was verified by neutron scattering [84]. Interestingly, the alkali sesquioxides Rb_4O_6 and Cs_4O_6 exhibit frustrated magnetic ordering implying by the pronounced difference between ZFC and FC measurement as shown in Fig. 1.15. Such irreversibility between ZFC and FC is typical for magnetically frustrated system, for example, this effects is well-known to occur in spin glasses.

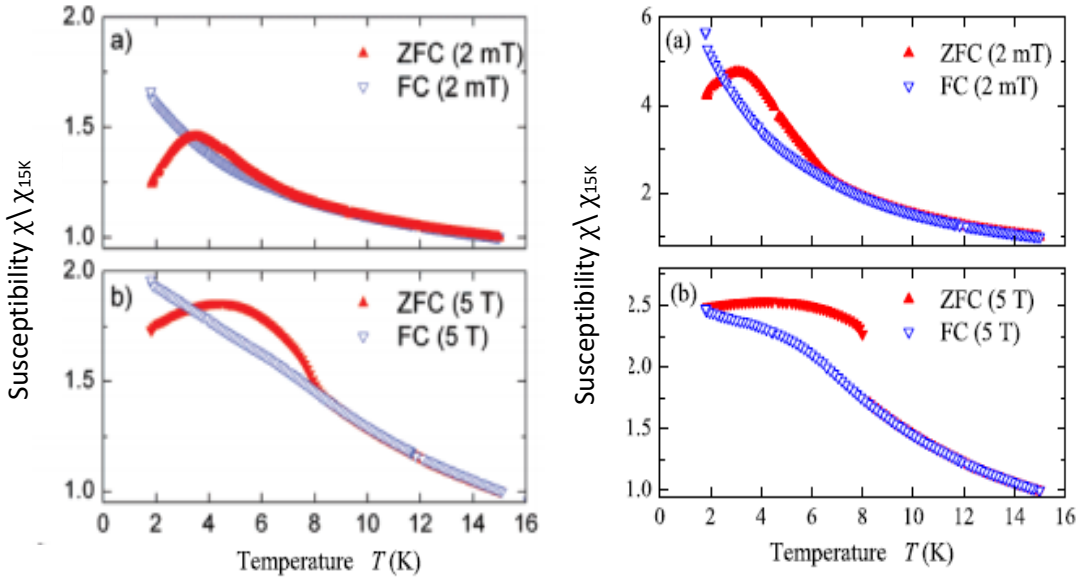

Figure 1.15: Magnetization data for Rb_4O_6 (left) and Cs_4O_6 (right). The low-temperature behavior of the magnetic susceptibility is shown in panels a and b for induction fields of 2 mT and 5 T, respectively [85].

1.4. Muon Spin Relaxation (μSR)

1.4.1. Properties of the Muon

Muon were first studied in cosmic rays, now produced in large accelarators. Muon spin relaxation (μ^+SR), an experimental technique used as the probe of the magnetic field inside matter at a microscopic level, is suitable for the study of condensed matter physics. Unlike neutron which experience scattering process, muon decays and stops at the certain position inside the sample. μ^+SR gives a local information of magnetism at particular point. Positive muon sits well away from nuclei in regions of large electron density. The muon carries a half spin and a large gyromagnetic ratio which therefore acts as a very sensitive probe to study the local magnetic field. Some basic properties of the μ^+ particle is summarized in Table 2.1.

Table 1.3. Basic properties of the positive muon (μ^+) [86,87]

Mass	m_μ	206.763835(11) m_e or 0.1126096 m_p
Charge		+e
Spin	S_μ	½
Lifetime	τ_μ	2.19714 (13) μs
Magnetic moment	μ_μ	8.8905981 (13) μ_N or 3.1833452 (20) μ_P
Gyromagnetic ratio	$\gamma_\mu/2\pi$	135.53879 (1) MHz T^{-1}

When positive muons, μ^+ , are deposited in a chemical sample at least three possible events can occur [88] :

(i) μ^+ sits in the sample and decays (characteristic lifetime = 2.2 μs)

(ii) μ^+ combines with an electron to form a muonium atom, Mu, a radioactive light isotope of hydrogen.

(iii) Mu reacts with the substrate to form a muonium-substituted radical, or resides in a diamagnetic environment.

1.4.2. Basic Principle of μSR

High energy proton beams (protons of 600 to 800 MeV kinetic energy produced using synchrotrons or cyclotrons) are bombarded into a target (light element target) usually graphite with the thickness ~10 mm as illustrated in Fig. 1.16.

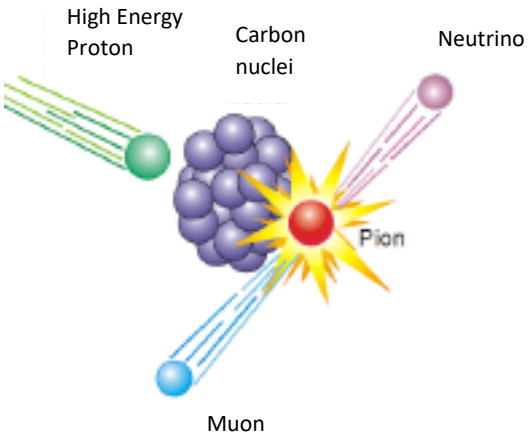

Figure 1.16. Illustration of the muon production process.

That high energy protons (P) interact with protons (p) or neutrons (n) of the nuclei to produce pions (π^+) via:

$$P + p \rightarrow \pi^+ + p + n \qquad (1.1)$$

$$P + n \rightarrow \pi^+ + n + n \qquad (1.2)$$

Pions decay in 26 ns, then the pions decay into muons (and neutrino muon):

$$\pi^+ \rightarrow \mu^+ + \nu_\mu \qquad (1.3)$$

This decay has to fulfill the conservation of linier momentum (the μ^+ is emitted with momentum equal and opposite to that of the ν_μ) and the conservation of angular momentum (μ^+ and ν_μ have equal and opposite spin). The pion decay is two body decay (see Fig. 1.17). To conserve momentum, the muon and the neutrino must have equal and opposite momentum. The pion has zero spin so the muon spin must be opposite to the neutrino spin. One useful property of the neutrino is that its spin is aligned antiparallel with its momentum (it has negative helicity), and this implies that the muon spin is similarly aligned.

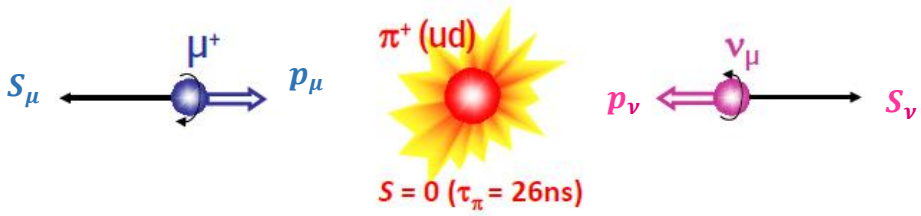

Figure 1.17. Illustration of pion decay. Due to the linear momentum conservation, the muon spin is polarized antiparallel to its momentum.

The muon is then steered by variety of electromagnets to the spectrometer and implanted into the sample. The implanted muon stops at positions which is typically in order 100-300 μm depth from the surface of the target sample. The muons are stopped in the specimen of interest and decay after a time t with probability proportional to e^{-t/τ_μ}. The muon decay is three body process (see Fig. 1.18):

$$\mu^+ \rightarrow e^+ + \nu_e + \bar{\nu}_\mu \qquad (1.4)$$

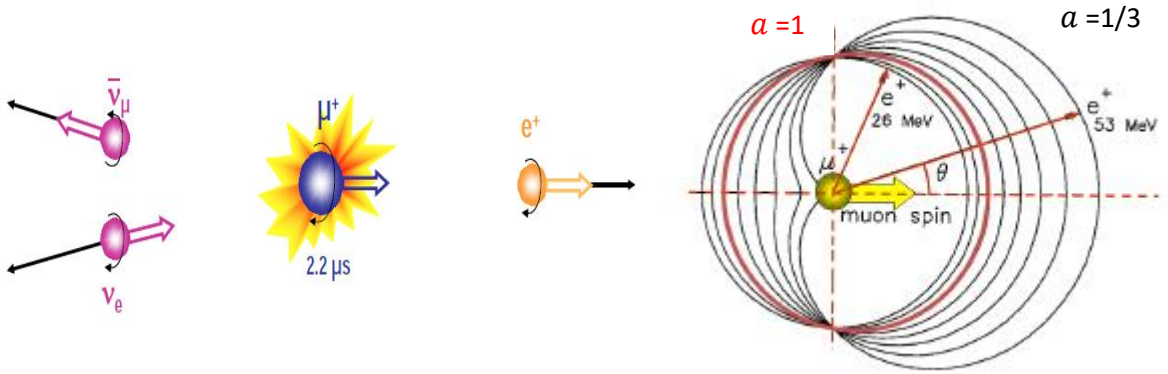

Figure 1.18. (left) Decay of the muon into a positron and pair of neutrinos. (right) The angular distribution of the emitted positrons [89].

This phenomenon (which also lies behind the negative helicity of the neutrino) leads to a prosperity for the emitted positron to emerge predominantly along the direction of the muon spin direction when it decayed. The muon spin is 100% polarized after its production. The self-spin-polarization can allow us to carry out experiments even in the zero-field condition which is ideal to study magnetic properties. The probability distribution of positron emission at angle θ relative to the muon spin S_μ is :

$$W(\theta) \propto [1 + a\cos(\theta)] \qquad (1.5)$$

The asymmetry parameter a =1 for the maximum positron energy and the average over all energy a is equal to 1/3, which is the ideal experimental asymmetry value when no positron electron discrimination is performed. The experimentally observed value of a is typically 0.23 which is smaller than the theoretical/ideal value of 1/3. This is due to a finite solid angle of the positron detectors and energy dependent efficiencies of detection systems.

Emitted positrons are detected and accumulated as a time histogram. The histogram is described by equation 1.6. and illustrated in Fig. 1.20 (a).

$$N_{det}^{e^+} = N_0 e^{-\frac{t}{\tau_\mu}} [1 + aP(t)cos\phi_{det}] + \mathrm{b} \qquad (1.6)$$

The exponential component describes the decay of the muon with the lifetime of τ_μ, b represents a time-independent background and a is the asymmetry of the muon spin polarization at t=0. The P(t) expresses the time dependence of the muon spin polarization and ϕ_{det} is the phase factor that accounts for the angle between the initial muon polarization and the positron detectors.

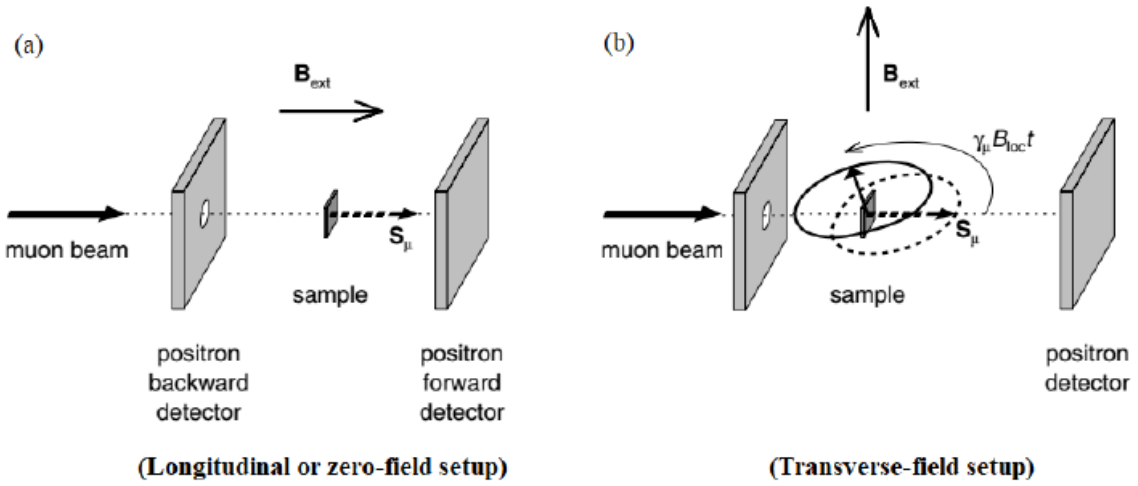

Figure 1.19: Three types of μSR experimental setup (a) zero-field (ZF-μSR) or longitudinal field (LF- μSR). ZF measurement is possible for μSR experiment due to the self-spin-polarization of muon. In LF-μSR, a magnetic field is applied in parallel to the muon spin S_μ (b) transverse field (TF-μSR), a magnetic field is applied perpendicular to S_μ.

Three experimental configurations are usually used in experiments illustrated in Fig. 1.19. As illustrated in Fig. 1.19, the positron detectors are placed parallel and antiparallel to the muon beam (S_μ), which are usually referred as backward (the downstream side) and forward (the upstream side), respectively. Both forward and backward detectors record millions of decay events which are used to create histograms of the asymmetry of the muon–spin-polarization versus time based on numbers of positrons counted by the forward (N_F) and backward (N_B) counters. The time dependent histogram can be represented as:

$$aP(t) = A(t) = \frac{N_F(t) - \alpha N_B(t)}{N_F(t) - \alpha N_B(t)} \qquad (1.7)$$

Within equation 1.7, $A(t)$ is thus defined as the μSR time spectrum. Here α is a parameter to geometrically compensate of numbers of counted muons by forward and backward counters. The α value can be calculated from a TF- μSR measurement in the same geometry. After the correction by using the measured α, the time spectrum should oscillate symmetrically around the zero average polarization as shown in Fig. 1.20 (b).

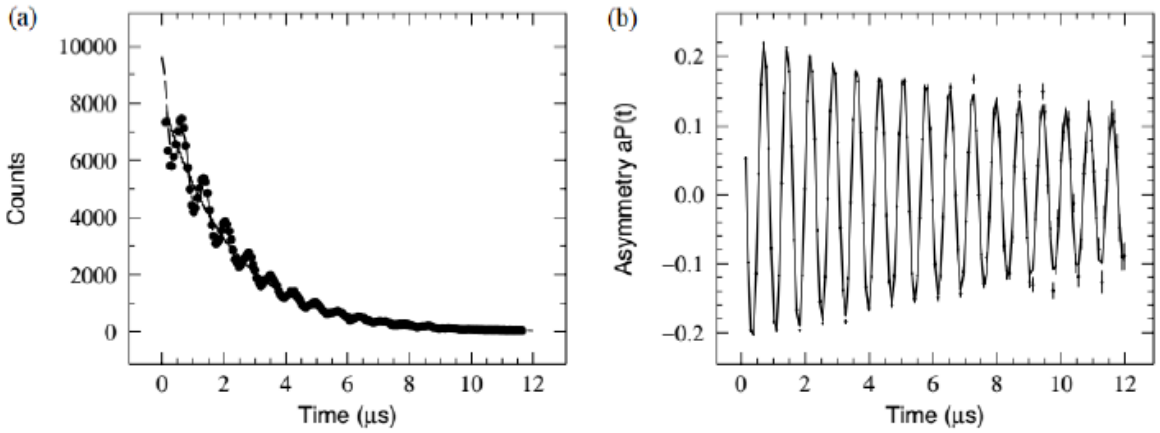

Figure 1.20. (a) Time histogram of accumulated positrons counted by forward and backward counter. The broken line indicates the best fit result by using Eq. 1.6. (b) The time dependence of asymmetry measured in a TF condition as decribed in Eq. 1.7.

μSR experiments can distinguish magnetic ordering under ZF condition. Within a target sample, muons stop at interstitial sites or near to electronegative atoms. When they experience magnetic fields perpendicular to their spins, they show the Larmor precession motion around magnetic fields. If magnetic fields at all muon stopping positions are homogeneous, therefore,

coherent oscillations in the μSR time spectra are observed. Magnetic field parallel to the initial muon-spin direction do not give rise to oscillations and cause depolarizations only if the fields are fluctuating in time. Equation 1.8 is an example of the function of μSR time spectra which consists of oscillation and depolarization parameter.

$$A_z(t) = a_L G_z(t) + a_T G_x(t)\ \cos(\gamma_\mu |B_1| t) \qquad (1.8)$$

where B_1 is local field, a_L is asymmetry from depolarization component, and a_T is asymmetry from precession component (a_L+a_T=a_{ZF}). For a homogeneous magnetic sample a_L/a_{ZF}=$1/3$, while if only part of the sample is magnetic $a_L/a_{ZF} > 1/3$ [90]. In this case, the muon spin precession at the center of 1/3 with the amplitude of 2/3 is observed in the μSR time spectra. Accordingly, we can define the magnetic volume fraction from asymmetry parameter as follow:

$$f_{mag} = \frac{3}{2} \times (1 - \frac{a_L}{a_{ZF}}) \qquad (1.9)$$

Ideally for a homogeneous sample, f_{mag} is equal to 1. Its value is less than 1 in case of that only a part of sample is magnetic. The coherent oscillation observed in the μSR time-spectrum indicates the appearance of the LRO in a target sample. In case of LRO state, the correlation length of the spin alignment should be extend over several unit cells which is at least 20-30 Å, while the correlation length in short-range magnetic ordering (SRO) is on the order of 5 Å resulting in no spontaneous muon-spin precession [91].

The magnitude of local field, which represents the size of ordered magnetic moment of a target sample, can be determined from the frequency parameter based on Larmor equation $\omega_i = 2\pi\gamma_\mu H_{int(i)}$. Also, the Fast Fourier Transform (FFT) remains useful as an approximate visual illustration of the internal magnetic field distribution and for comparing the measured μSR signal with the best fit theory function from the time domain.

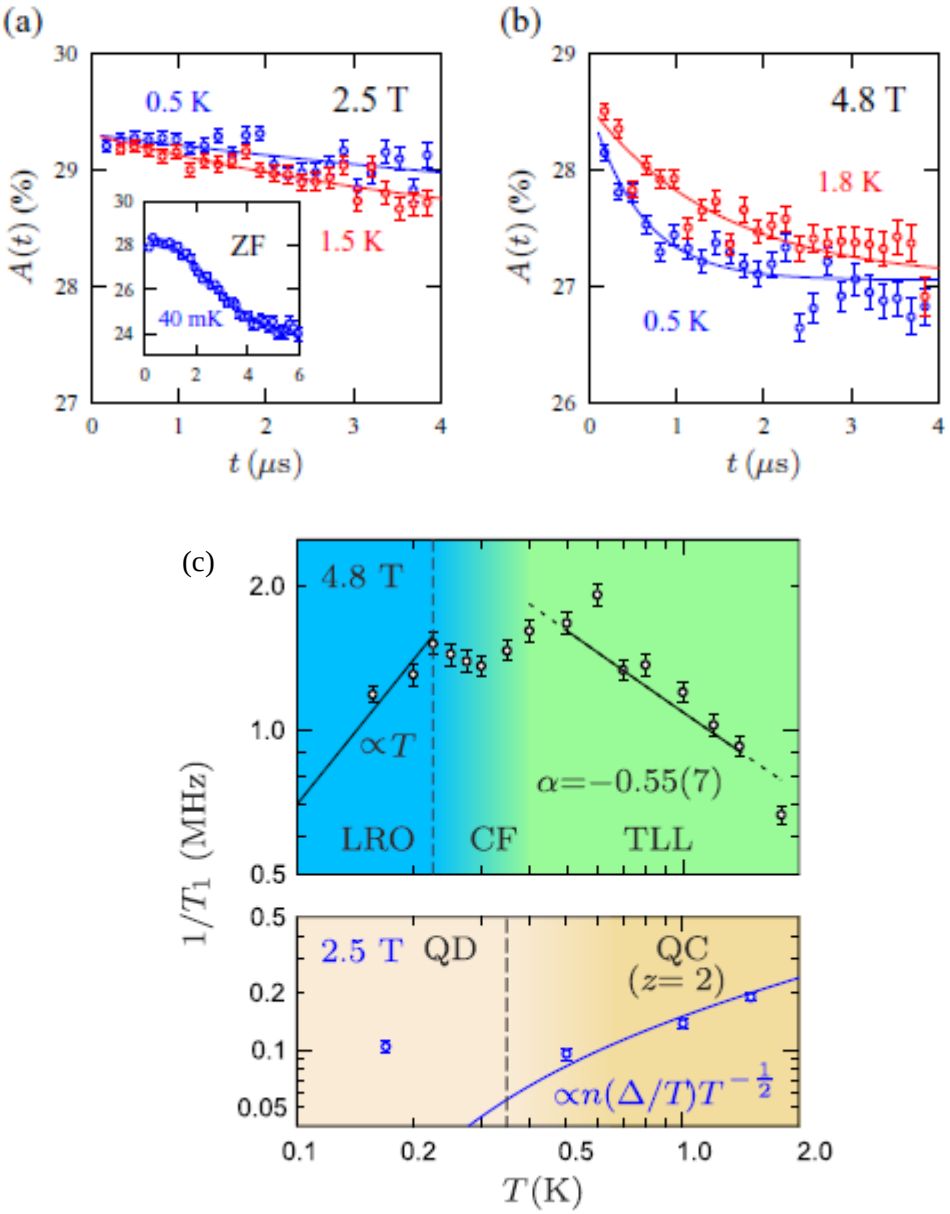

Figure 1.21. Experimental muon decay asymmetry in (a) Data in a longitudinal field $\mu_0 H$ = 2.5 T (outside TLL phase) on the powder sample. Inset: Data measured in zero applied field on a mosaic of single crystals showing Gaussian relaxation due to nuclear moments. (b) Results in applied longitudinal field $\mu_0 H$ = 4.8 T (in the TLL phase). (c) Relaxation rate $1/T_1$ at μH = 4.8 T (top) and $\mu_0 H$ = 2.5 T (bottom). Top: The peak around T = 225 mK indicates long range ordering. Above the ordering transition, $1/T_1$ is first dominated by critical fluctuations before entering a regime of universal scaling for 0.4 K $\leq T \leq$ 2 K. Bottom: The dashed line indicates the approximate value of the gap for g = 1.94 at $\mu_0 H$ = 2.5 T [92].

μSR is also useful to investigate dynamics from a microscopic viewpoint. A more direct μSR measurement to distinguish dynamic/static relaxation is a LF decoupling measurement, in which an external magnetic field is applied parallel to the initial muon spin direction. Recently, J. S. Möller et al reported that μSR can probe the TLL behavior of spin dynamics which is the first observation of quantum-critical spin dynamics using μSR in "high" (>1 T) applied fields [92]. As shown in Fig. 1.21 (c), the temperature scan at constant field 4.8 T reveals a sharp rise of the relaxation rate with a peak around 225 mK, followed by nonmonotonic behavior in an intermediate region between around 225 and 400 mK. Above 400 mK, $1/T_1$ exhibits power law behavior. Following the power law approximation, a fitting range extending from 0.4 to 1.8 mK is justified within the TLL framework. The application of μSR technique can be also performed in order to study the spin-gapped system as already observed in several systems [93,94].

The μSR technique has the unique time window (10^{-6} to 10^{-11} s) for studies of magnetic fluctuations in materials, and is complementary to other experimental techniques, such as the neutron scattering, NMR and magnetic susceptibility measurement. It particularly suitable to study the magnetic materials which have very weak magnetic fields (down to ~ 10^{-5} T), small magnetic moments and random magnetism such as spin glass and short range ordering. μSR is also able to determine the magnetic moments with some computational efforts.

1.4.3. Types of Muon Facilities

Muon sources can be divided into two classes: continuous sources, where the muons arrive in a quasi-continuous stream; and pulsed sources. In a continuous source, a single muon is in the sample at any given time. Muons arrive intermittently and implant in the sample. Veto detectors positioned behind the sample can be used to flag up muons which have flown past the sample and not implanted. The clock starts when a muon enters the detection apparatus, and stops when a decay positron is incident on one of the detectors. However, if a second muon arrives before a positron is detected, it is impossible to know which of the two subsequent decay positrons came from which muon, and both events must be discarded. The requirement that only one muon be present at any given time restricts both the event rate and the low-frequency resolution of a continuous source. Since a muon may arrive and interrupt the experiment, increasing the rate of muon production eventually reduces the event rate of the experiment, because many events must be discarded. Similarly, increasing the time window over which each event is recorded in an attempt to increase the low-frequency resolution also

increases the probability that a new muon will arrive and interrupt an event; thus, event rate and low-frequency resolution are in competition with one-another. In practical, ideally, the adjusment of the number of muon stop can be set to be ~ 35,000 (based on the experience during the experiment at DOLLY, PSI). A further consequence of a continuous source is high background; muons which neither embed in the sample nor set off the veto detector can result in spurious counts, especially at long times. In fact, this sets a practical limit of around 10 μs on experimental counting. PSI and TRIUMF are the facilities to produce the continuous muon beam.

A pulsed muon source delivers muons in large bunches rather than individually. All the muons implant in the sample approximately simultaneously, starting the experimental clock, and positron emission is timed with respect to the arrival of the pulse. The disadvantage of a pulsed source is that a resolution limit is imposed on precession frequencies by the width of the pulse. In spite of this restriction, it may still be possible to detect a transition to long-range magnetic order where frequencies are too high to resolve. Significant reductions in initial asymmetry below the transition are often observed because a reduced value of $A(t)$ corresponding approximately to the average value of the invisible oscillations is seen. Conversely, asymmetry at long times can increase due to the effect of the 1/3-tail. It is also often possible to observe discontinuous variations in relaxation rates with temperature. The limit on the rate of data acquisition at pulsed sources is imposed by the finite detector dead time (often around 10 ns). This is the time after detection of a positron during which further positrons will not be acknowledged. Consequently, rather than using just two detectors as in an idealised μSR experiment, large numbers of individual detectors are used. The ISIS at RAL and MLF at J-PARC host pulsed muon sources available for μSR expeiment.

1.5. Electronic Structure in Alkali-metal superoxide

The determination of electronic structure strongly depends on the on-site Coulomb repulsion energy U and the kinetic energy related to orbital overlap t. The limiting case where U is much larger than t ($U>>t$) results in a Mott insulator. In the insulating state, the highly correlated electrons minimise their electrostatic repulsion. The other limit with high electron density and a small interaction strength U/t will result in a metallic state where kinetic energy is dominant with a tendency to delocalize electrons. In the limit where on-site Coulomb repulsion U and the kinetic energy are comparable, a metal-insulator takes place.

Antiferromagnetic order is found experimentally at low temperatures AO_2 and it was suggested by recent density functional theory (DFT) and model studies that the insulating character of AO_2 at low temperatures can be explained by the interplay of correlation effects (spin and orbital order) and crystal distortions [52,54,95]. There have been a considerable number of reports on AO_2 in the last 4 years, both on theoretical and experimental studies. AO_2 is one of the candidates of strongly correlated molecular solid. Some reports from the band structure calculations presented the observation of a half-metallic in this system [52,54,63]. In calculations that use generalized gradient approximation (GGA) of Perdew, Burke, and Ernzerhof [96] for exchange-correlation functionals, alkali-metal superoxides are found to exhibit a half-metallic ground state due to the partially filled π-antibonding level. GGA is one of exchange correlation functions which suitable for most magnetic systems [97]. Current result of some AO_2 systems show the important contribution of on-site Coulomb correlation *U* and even the spin orbit (SO) coupling in order to reproduce fully insulating state indicated by band gap opening in AO_2 [52,53,63].

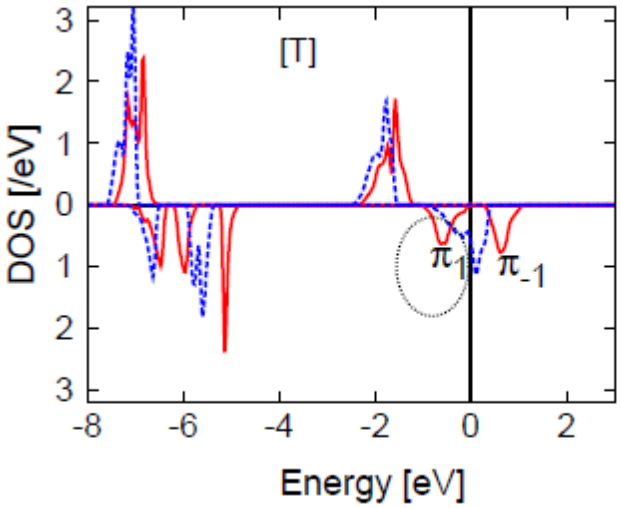

Figure 1.22. The PDOS of oxygen 2p states of KO_2 with the high symmetry un-rotated structure. The dotted (blue) and solid (red) lines represent the DOS in the GGA+*U* and GGA+*U*+SO, respectively (*U*=6.53 eV).

It was reported that Coulomb correlation effect has the important role for determining the electronic structure in AO_2. M. Kim *et al* [63] showed that the insulating nature of the high symmetry phase of KO_2 at high temperature arises from the combined effect of the spin-orbit coupling and the strong Coulomb correlation of O 2p-electrons. As shown in Fig. 1.22, the state near E_F do not split in GGA+*U* with *U*=6.53 eV. They become split only when the SO is included in the GGA+*U*. On the other hand, for the low symmetry, phase of KO_2 at low

temperature with the tilted O_2^- molecular axes, the band gap and the orbital ordering are driven by the combined effects of the crystal-field and the strong Coulomb correlation. The crystal field effect will be activated due to tilting of O_2^- molecular axes toward K^+.

In RbO_2, Kovacik and Ederer [53] demonstrated the importance of an onsite Coulomb interaction *U*, which led to the formation of an orbitally polarized insulating state. They suggested that RbO_2 at room temperature is in fact a Mott insulator, where the strong Coulomb repulsion prevents the electron hopping between adjacent sites. Calculating the electronic structure as a function of *U*, they found that the insulator state arises at U=2 eV. There is also orbital polarization found in RbO_2 driven by strong on-site interactions. On the other hand, in CsO_2, a value of U= 4 eV was chosen for the oxygen 2p-orbitals in the GGA+U method [98].

1.6. Motivation and Purpose of the Study

The dimension of the system and the spin value play a crucial role for the nature of ground states. The reduced dimension and the interplay between spin, orbital, lattice and charge degrees of freedom are fascinating issues in condensed matter physics. Magnetic materials realizing these phenomena are quite often found in transition metal oxides such as cuprates and vanadates. Recently, it has been suggested that alkali-metal superoxide is also a candidate of systems which has the interplay between spin, orbital, and lattice degrees of freedom. The low-dimensional magnetic interaction is also expected to be presented in the class of this system. One attractive feature of those alkali-metal superoxides is that the magnetic properties are well affected by changes in the lattice symmetry. Such changes in the lattice symmetry has been proposed to be caused by changes in the orientation of the O_2^- dumbbell. In addition to this, those changes in the structure and magnetic properties depend on the alkali-metal ion. Detail investigations to achieve the deeper insight for structural and magnetic properties of AO_2 are the main objective of this study.

RbO_2 and CsO_2 are isostructural structure at room temperature. Since the low-temperature structure of both system is not yet well-determined at this moment (refer to page 14), the detail temperature dependence of synchrotron XRD measurement is very important in order to check the structural changes with temperature for both systems. The study of lattice structure is important in this system since electronic and magnetic structure significantly affected by the relative orientation of O_2^- dumbbell within the crystal lattice.

In this doctoral thesis, we mainly used the muon spin relaxation (μSR) to investigate magnetic properties of alkali-metal superoxides especially in the ground state. μSR can give more detail investigation on magnetic properties including the estimation of internal field and the magnetic volume fraction. The magnetic properties are suggested to be different by the changing of the cation in AO_2. Another issue is that TLL model suggested in the CsO_2 supposed to appear a field-induced magnetic order which would be related to the TLL state [18]. Therefore, the detailed investigation on the magnetic properties near or in the zero-field (ZF) condition is strongly required to describe the magnetically ordered state appeared in the CsO_2 and other alkali-metal superoxide. Other experiments directly related to the magnetism in AO_2 were always conducted under finite magnetic fields. We have measured the polycrystalline CsO_2, RbO_2 and NaO_2 sample by using μSR under ZF and LF condition. Detail μSR results are written in Chapter 3, 4 and 5.

Chapter 2
Experimental Detail

2.1. Sample Handling and Preparation

The alkalimetal superoxide systems that we successfully synthesized were CsO_2, RbO_2 and NaO_2. Polycrystalline samples were prepared by using solution method (oxidation of the metal dissolved in liquid ammonia). The samples are synthesized at Prof. Takashi Kambe Laboratory in Okayama University. Starting materials to synthesize the samples are alkali metals: Cs metal (Aldrich Co. Ltd, 99.95% purity)/ Rb metal (Nilaco Corp., 99.98% purity)/ Na metal (Aldrich Co. Ltd, 99.9%). Beside that, ammonia (Sumitomo Seika Co. Ltd, 99.9%) is used as a solvent and also oxygen gas (Air Water, Inc., 99.9%) which is needed for the formation of AO_2.

Ampoules containing alkali metals were brought and then cut into an argon-filled glove box (Fig. 2.1 (a)). Pieces of alkali metal were transferred using a spatula into the reaction cell. The valve on the reaction cell/hyper glass cylinder (producted by Taiatsu Techno Corporation) can be closed tightly, allowing it to be transferred out of the glove box (Fig. 2.1 (b)). The oxygen and water content inside the glove box was maintained to be less than 0.1 ppm that was then dynamically pumped down to 10^{-2} Pa.

(a)  (b) 

Figure 2.1. (a) Alkali metal on ampoule (b) Reaction cell used for the synthesis of AO_2

It is well known that alkali metals are dissolved in water-free liquid ammonia (NH_3). Ammonia is a colorless gas with an intense odor above its boiling point of -33^{o}C and melting point (solid) of below -77^{o}C.

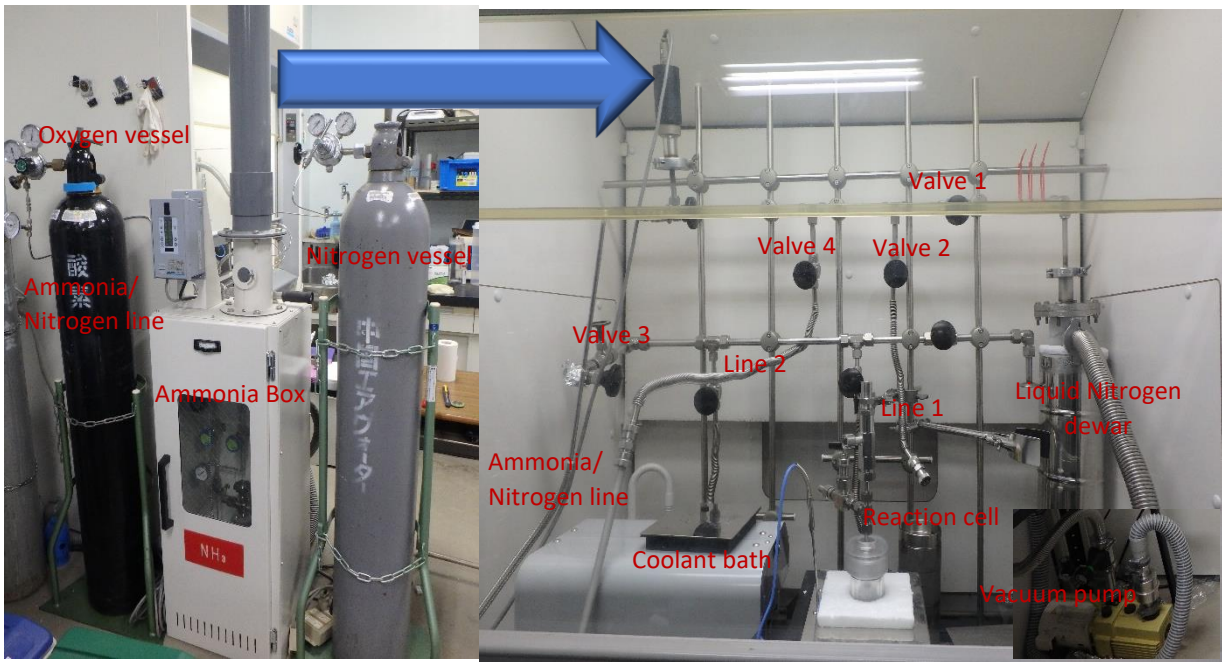

Figure 2.2. The complete set up for the synthesis process. The vacuum line was used for synthesizing alkalimetal superoxides.

In order to perform the synthesis of alkalimetal superoxide, a vacuum line was needed with the complete set up shown in Fig. 2.2. Connections between different parts of the vacuum line setup were controlled by a series of valves. The vacuum line was separated from the pump by a liquid nitrogen to avoid corrosion and breakdown of the pump. The reaction cell was connected to the line 1. In order to do the transfer, we need to adjust the valve by opening/closing it.

Table 2.1. The best synthesis condition to obtain AO_2 sample

Sample	NH_3 transfer	O_2 pressure (bar)	Stirrer speed (rpm)	Reaction Temp (^oC)	Reaction Time (hour)
RbO_2	3 times	1.4	200	-40	90
CsO_2	3 times	1.4	200	-40	60

Before starting the condensation of liquid NH_3 in the reaction cell, it was evacuated to remove the argon gas from the glove box. In case of the syntesis of RbO_2 and CsO_2, NH_3 was transferred 3 times by the time of 5 minutes for each. When alkali metals are dissolved in liquid NH_3, a dark blue solution as shown in Fig. 2.3 (a) appears due to the formation of solvated

electrons. The valve to the oxygen supply was then opened and oxygen was transffered into the reaction cell for oxidation of the alkali metal. Before passing into the reaction cell, the column was flushed 3 times with oxygen to make sure that it was dry enough. The initial pressure of oxygen supplied to the reaction cell was around 1000 mbar. After transferring the oxygen, the reaction cell is inserted into the cooling bath. The reaction was carried out at low temperature, which was achieved using a cooling bath, where ethanol (Okayama Yakuhin Kogyo, 99%) was used as the coolant as shown in Fig. 2.2. The temperature of cooling bath was set to be -40^{o}C with the stirring process. The reaction was varied in between 2 -7 days until the best condition was obtained. Table 2.1 displays the best condition to achieve the high-purity AO_2 sample. The solution was constantly stirred during reaction using a magnetic stirrer.

Reaction process:

$$A(s) \xrightarrow{NH_3} A(l) \qquad \text{..... (2.1)}$$

$$A(l) + O_2 \rightarrow AO_2(s) \qquad \text{..... (2.2)}$$

Exposure to oxygen led to a colorless solution, followed by a white color and finally a yellow precipitate which indicates formation of the alkalimetal superoxide. Once the yellow precipitate had formed, the liquid ammonia was removed from the solution by opening the valve to the vacuum line. After it was completely removed, the dry powder (see Fig. 2.3 (b)) in the reaction cell was carefully transferred to the glove box for storage.

(a) (b)

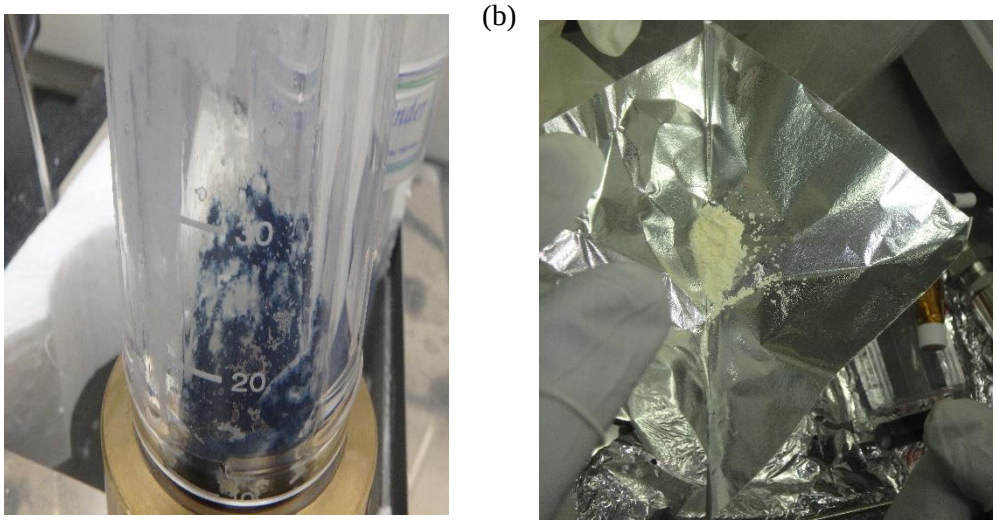

Figure 2.3. (a) Alkali metal is dissolved in liquid NH_3. (b) Product of synthesis process.

In case of the synthesis of NaO_2, reports in the literature have suggested that it is rather difficult to synthesize high purity NaO_2 [99]. The relative difficulty in synthesizing pure superoxides of the lighter alkali metals relative to the heavier one is thus due to the higher solubility of lighter alkali superoxides. In the beginning, we used the same method by using solution method (oxidation of the metal dissolved in liquid ammonia). But, it is still pretty much amount impurities were contained in the sample. In order to suppressed the formation of impurity, following the result of *S. Giriyapura* [100], a new solution route to the synthesis of NaO_2 has been found, using a solvent mixture of methylamine (CH_3NH_2) and ammonia (NH_3). The presence of ammonia in the mixture is required to dissolve Na metal, whereas methylamine suppresses the further side reaction of superoxide anions with the solvent.

Reaction process:

$$Na \xrightarrow{NH_3 + CH_3NH_2} Na(l) \qquad \text{..... (2.1)}$$

$$Na(l) + O_2 \rightarrow NaO_2(s) \qquad \text{..... (2.2)}$$

A new solution route could obtain a better quality of the NaO_2 sample indicated by the sample color as displayed in Fig. 2.4. The more yellow the sample, the better the quality.

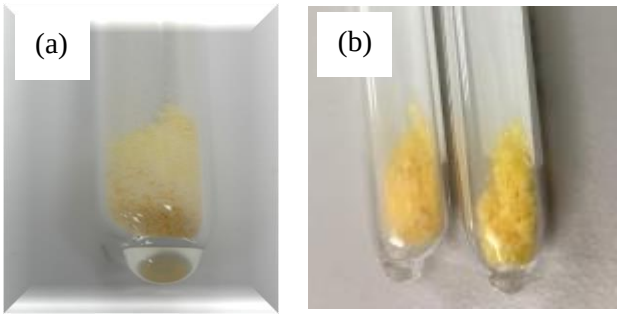

Figure 2.4: Sample dissolved using (a) ammonia (b) ammonia and methylamine

2.2. Phase analysis and structural characterization

X-ray powder diffraction (XRD) was used for analyzing the phase and obtaining detailed information of the crystallographic properties of the samples. The sample was prepared and inserted into the small glass capillary with diameter ϕ 0.3 mm as shown in Fig. 2.5 (a) and then mounted to the goniometer in Fig. 2.5 (b).

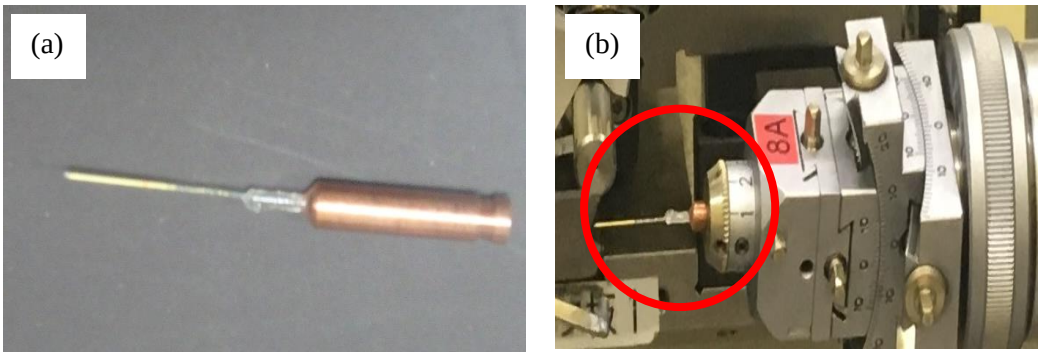

Figure 2.5. (a) AO_2 sample was inserted into the glass capillary (b) Sample was mounted to the goniometer.

2.2.1. Conventional x-ray powder diffraction

In a sealed x-ray tube, the x-ray beam is produced by the collision of high energy electrons with a metal target. The wavelength of x-ray is a characteristic of the used metal target. This thesis includes data measured using Molybdenum (Mo) and Cupper (Cu) targets. This corresponds to a wavelength, λ, of 0.7093 Å for Mo and 1.5406 Å for Cu, respectively. The laboratory XRD experiment is important to check the sample quality before performing synchrotron XRD experiment.

Figure 2.6. XRD machine Rigaku Max-007 HF in Okayama University.

2.2.2. Synchrotron x-ray powder diffraction

The synchrotron XRD was carried out in BL-8 at the Photon Factory in KEK. In this beamline, one can utilize the synchrotron radiation from a bending magnet in the 40 eV to 35 keV energy range. The beamline has three branch beamlines (8A, 8B, and 8C). Our synchrotron x-ray powder diffraction experiment was carried out in BL-8A using x-ray with 15 keV energy and wavelength, λ, 0.99917 Å. The sample standart CeO_2 was used in order to check the wavelength for this experiment. The cryostat can be cooled down to 20 K with the rate of 5 K/minute. We used short x-ray exposure time (t=15 s) in order to prevent sample damage. The synchrotron XRD data were analyzed using the GSAS (General Structure Analysis System) software [101].

There are some advantages of synchrotron XRD than conventional XRD. Synchrotron XRD tends to have high resolution making the clearer observation of fine peak splitting. Synchrotron XRD has a high energy (providing the high penetration and high scattering vector, Q) which results in more accurate atomic displacement parameter. Besides that, we can also check the wavelength and adjust the exposure time of x-ray into the sample.

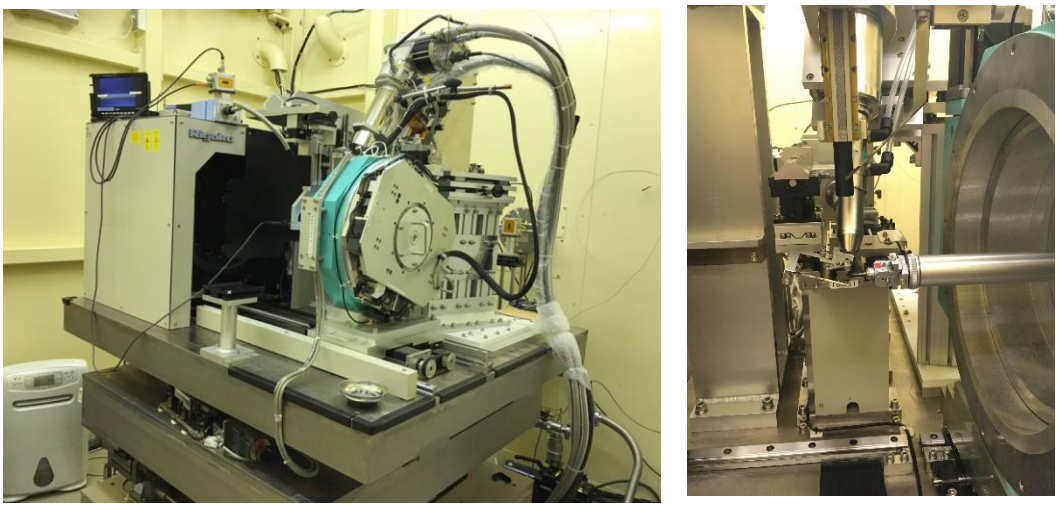

Figure 2.7. XRD machine at BL-8A in KEK, Japan.

2.3. Physical Properties

2.3.1. Magnetization Measurements

The magnetic properties of all alkalimetal superoxide samples in this thesis were measured using a Quantum Design MPMS 3 SQUID (Superconducting Quantum Interference Device) magnetometer. The machine can be operated under the temperature in between 2 and

300 K with a maximum magnetic field ± 7 T (Fig. 2.8 (a)). The system contains two main parts: a superconducting magnet for applying magnetic fields and a pick-up coil for detecting magnetic signals from the samples. The pick-up coil is connected to a SQUID, which gives extremely high sensitivity in detecting magnetic signals. During measurement, the sample is moved up and down, giving an alternating magnetic flux in the pickup coil. The alternating magnetic flux is output by the SQUID as an alternating voltage, which is then amplified and read as the magnetic moment of the sample as shown in Fig. 2.9. The SQUID can detect magnetic moment down to 10^{-7} emu.

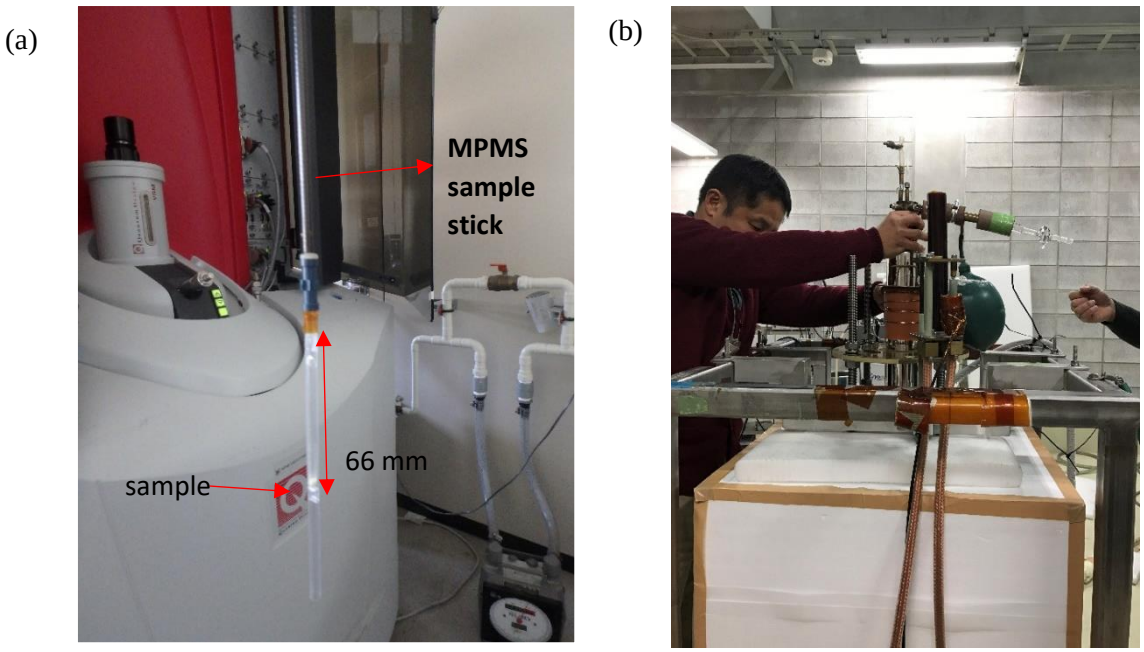

Figure 2.8. (a) Quantum Design MPMS magnetometer in Okayama University and sample set up for (b) High-field magnetization experiment in ISSP, Japan.

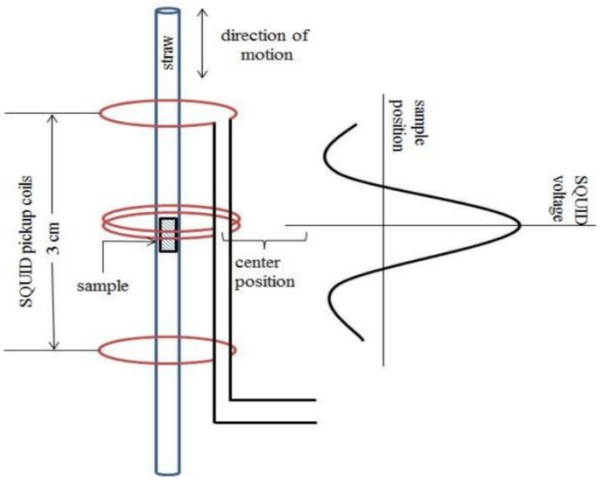

Figure 2.9. The configuration of SQUID magnetometer in a MPMS setup [102].

Alkali-metal superoxide samples measured in this thesis were in powder (polycrystalline) state. For the sample preparation, the powder sample with mass ~5-10 mg was placed into the ~5 cm ESR tube inside a Ar-filled glove box. The tube was then sealed using a small flame while pumping to evacuate Ar contents. The sealed ESR tube was inserted into a plastic straw and was fixed tightly inside the plastic straw to prevent the sample dropped. The straw was mounted on the end of the MPMS sample stick using thermal conductive tape (see Fig. 2.8. (a)). The temperature of MPMS machine must be set to be 300 K in the beginning. After mounting, the whole stick with sample was inserted slowly into the MPMS sample chamber followed by flushing the venting chamber 3 times. The sample was centered twice at 300 K and 2 K under applied field.

The magnetic susceptibility of the samples was measured as a function of the temperature in zero-field-cooled (ZFC) and field-cooled (FC) mode. For ZFC mode, the sample was cooled down to 2 K in zero applied field. A magnetic field was then applied and the sample was measured on warming from 2 K up to 300 K. In FC mode, the sample was cooled down to 2 K in the same applied field.

Beside doing magnetization measurement using MPMS, the high-field magnetization measurement was also carried out in Institute of Solid State Physics (ISSP), The University of Tokyo, Japan. The external field up to 60 T using pulsed magnet can be applied in order to observe the magnetic behavior under high-field (see Fig. 2.8 (b)).

2.3.2. Muon spin relaxation (μSR) measurements

μSR measurements were mostly perform at the DOLLY spectrometer, Paul Scherrer Institut (PSI) in Switzerland. Positive muon with momentum 28 MeV/c were directed to the spectrometer. In DOLLY spectrometer, the degree of polarozation of muon is >95% and the direction of spin is ~8-45^{o} with respect to beam axis (depending of the mode of the spin-rotator). The DOLLY spectrometer has four positron detectors: forward (F), backward (B), right (R), left (L) and two veto detectors that are placed in the forward and backward directions along the muon beam as shown in Fig 2.10. A backward veto detector (B_{veto}) consists of a hollow scintillator pyramid with a 7x7 mm hole facing the M counter. The function of B_{veto} is to collimate the muon beam to a 7x7 mm spot and to reject muons (and their decay positrons)

missing the aperture. On the other hand, a forward veto detector (F_{veto}) is to reject muons missed to hit the sample.

The Variox and Heliox-VT system used in the DOLLY instrument is a commercial based provided from Oxford instrument. The Variox cryostat can be operated in well defined temperature regime with the temperature range of 1.6-300 K. The cryomagnetic device "LM510" is used to control the Nitrogen and Helium levels. The output of this device is used to control the automatic refilling of the Nitrogen and Helium into the Variox. The sample temperature in the Variox cryostat is controlled by the Mercury temperature controller by adjusting the balance between the heater power and the pressure. In the Variox cryostat, a sample is indirectly cooled by the ^{4}He exchange gas. The amount of the exchange gas in the sample space should be controlled carefully in order to reach the temperature below 2 K. The Variox system was used in conducting measurements on the RbO_2 and NaO_2 sample.

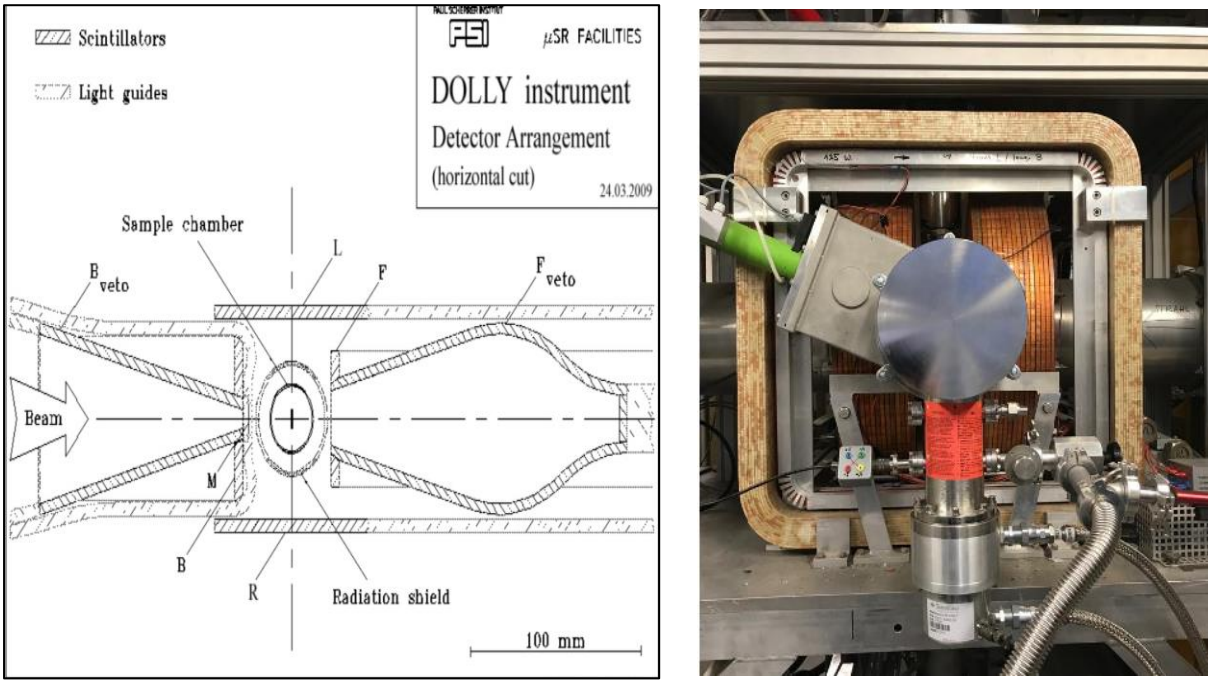

Figure 2.10. Horizontal cross section of the detector arrangement in the DOLLY instrument [103] and DOLLY spectrometer.

The ^{3}He insert is used to cool the sample temperature down to 0.3 K, named Heliox-VT system. Schematic view of the bottom part of the Variox cryostat with the ^{3}He insert in the position is shown in Fig. 2.11 (a). The insert is cooled by the Variox cryostat down to around

20 K using the ^{4}He exchange gas. Figure 2.11 (b) displays the detail parts of ^{3}He insert. After cooling the insert, the exchange gas inside the ^{3}He insert is then automatically condensed bya acharcoal, whereas the exchange gas in the Inner Vacuum Chamber (IVC) remains in it during the full operation. The ^{3}He gas contained in a small tank sitting on the top of the insert is then condensed at around 1.5 K by the 1 K pot. The 1 K pot consists of some thin metal plates and is cooled to below 2 K by the Variox cryostat through ^{4}He exchange gas. Once the ^{3}He pot has reached a stable temperature and the condensation has completed, the sorption pump will start to cool the ^{3}He pot and the sample to below 0.3 K. The Heliox-VT system was used in conducting measurements on the CsO_2 and NaO_2 sample.

(a)

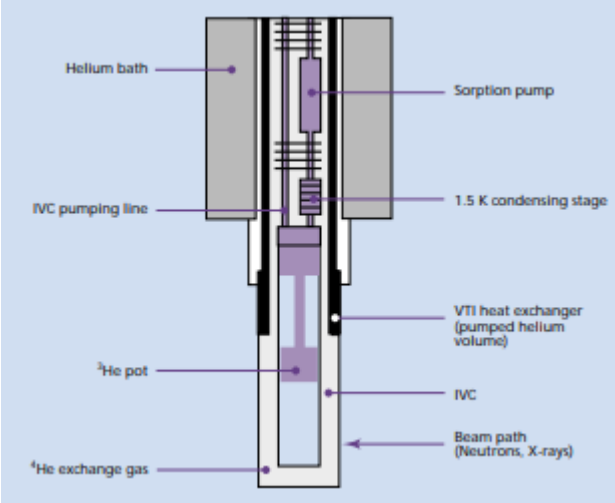

(b)

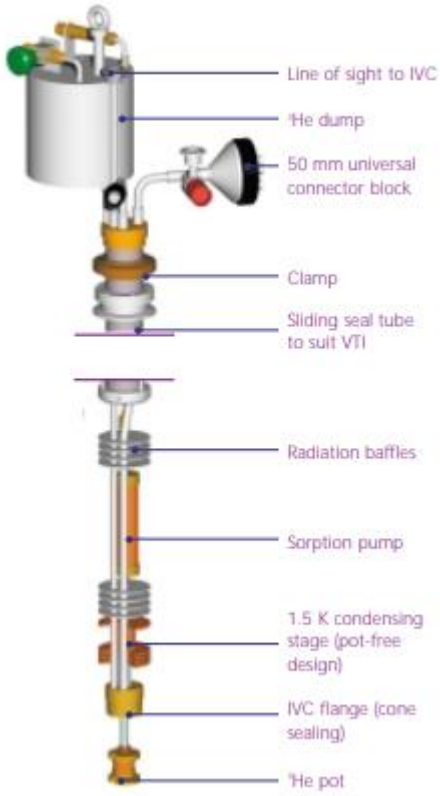

Figure 2.11. (a) The configuration of Variox cryostat with the ^{3}He insert in the position [103], (b) The detail parts of ^{3}He insert.

For μSR experiment, ~200 mg AO_2 sample was packed into the plastic bag (see Fig. 2.12 (a)). The sample was put on the center of the sample holder (see Fig. 2.12 (b)) and fixed by the aluminium or cupper tape as a pedestal.

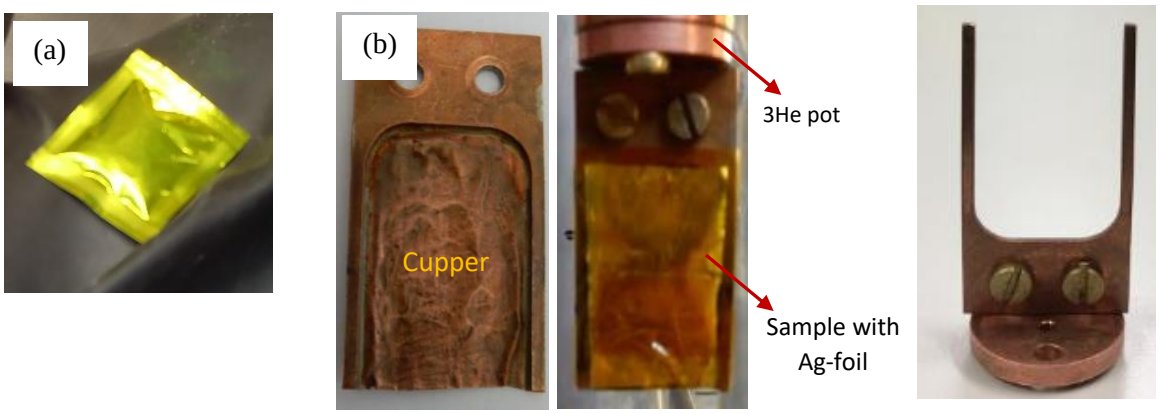

Figure 2.12. (a) Sample packing for μSR measurement (b) The sample holder with a thin Cu plate for the Heliox-VT cryostat (left) and also the sample holder for the Variox cryostat (right).

A sheet of Ag-foil (25 μm thickness) was put in front of the sample package to meet the density required to stop the incoming muons in the target sample (~150 mg/cm^2). ZF-μSR measurements were carried out for all samples from the lowest temperature 1.6 K (Variox) or 0.3 K (Heliox-VT), to above T_N. In addition, LF-μSR measurements were also performed. The geometrical factor, α, was estimated from a TF-μSR measurement under a field of 50 Gauss in the paramagnetic state of each sample. The μSR data were analyzed by using WiMDA (Windows Muon Data Analysis) software [104].

μSR measurements were also carried out at the HIFI spectrometer (ISIS) and ARGUS spectrometer (RIKEN-RAL). These two spectrometers are used in the pulsed muon beam in the UK. The muon instrument Argus (**A**dvanced **R**iken **G**eneral-purpose m**U**sr **S**pectrometer) can be used for a wide variety of studies in the areas of magnetism, superconductivity, charge transport, molecular as well as polymeric materials and semiconductors [105], while commisioning of the worldwide-unique HiFi instrument now enable μSR to probe spin dynamics in longitudinal field (LF) up to 5 T at 20 mK [106].

2.4. Calculation Work (The Estimation of Muon Stopping Position)

Knowing of the muon site(s) is often necessary for complete understandings of observed μSR signals, yet it is difficult to determine reliably. This is because, we implanted a charged particle inside the sample, which therefore gives effects on modifications of the local electronic environment. So far, there are four factors to be taken into account to determine muon site(s); dipole fields [107], electrostatic potentials [108], relaxation of atomic positions [109], and muon's zero-point vibrations [110]. Implanted muons usually stop at interstitial positions in the crystal lattice [108]. The bare μ+ is likely bonded to the most electronegative species such as oxygen or fluorine. In fluorides, this bonding often results in the formation of the $(F\mu F)^-$ ionic state, yielding the characteristic oscillation in the ZF- μSR time spectrum [111,112,113]. In oxides, it is believed that the μ+ sits about 1 Å away from the oxygen ion, as in the high T_c superconductors, for instance YBCO [114].

The electronic potential calculation with simplified parameters was used in this study. The electrostatic potential energy was calculated by employing the Density Functional Theory (DFT) method using the Vienna ab-initio simulation package (VASP) program [115]. DFT is a general-purpose computational method to derive electronic properties of the system based on the electron density. Although this trial has challenges, DFT calculations provide the better computational accuracy which offers possibilities of direct and quantitative comparisons with experiments [116,117]. The calculation was performed on a unit cell without the muon by using the supercomputing system of RIKEN named as HOKUSAI. The most minimum potential energy was then assumed as a muon stopping site [118]. It can be used for any physical systems which always toward the stability at the lowest energy.

Chapter 3

Result and Discussion on Cesium Superoxide (CsO_2)

3.1. Structural Phase Transition in CsO_2

At the room temperature synchrotron XRD result, we confirmed that CsO_2 adopts the structure of CaC_2: space group *I/4mmm*. Fig. 3.1 shows the fitted XRD pattern at the room temperature, with lattice parameters of $a=b=$ 4.469 Å and $c=$ 7.324 Å, in agreement with those reported for single crystal CsO_2 [12]. Very small amount of impurity that was found confirmed to be $CsOH.H_2O$ and its fraction was estimated to be less than 3% from the XRD analysis. This impurity phase should not influence the intrinsic magnetic property of CsO_2 because it has no unpaired electrons.

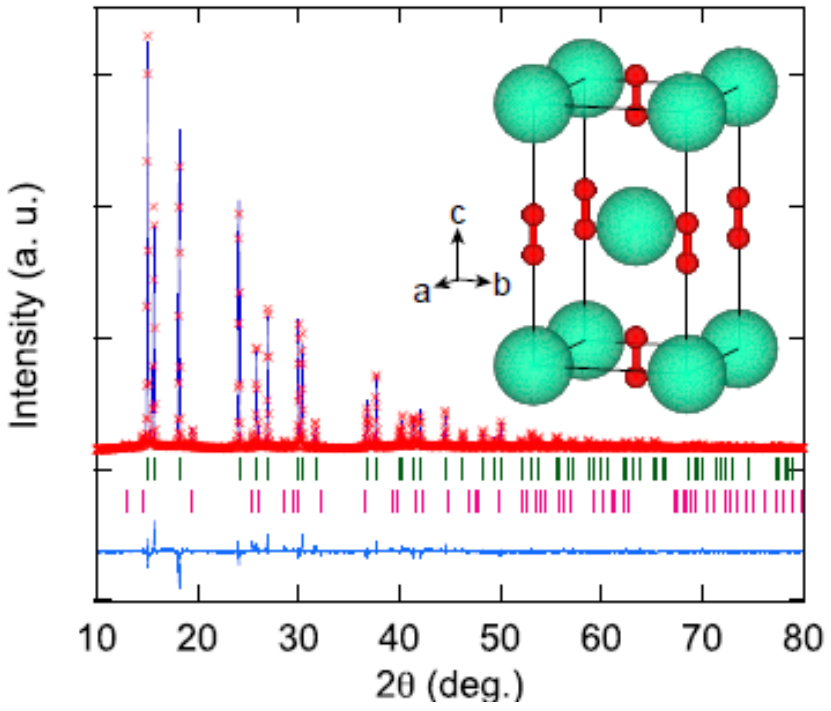

Figure 3.1. XRD pattern of CsO_2 measured at room temperature using synchrotron XRD. Bragg position of CsO_2 is indicated by small green line and bragg position of $CsOH.H_2O$ is indicated by small pink line [64].

Figure 3.2 shows the X–ray diffraction pattern of CsO_2 measured at the various temperatures from 20 K up to 300 K. The 200 peak at 2θ= 25.8° splits into 200+020 which indicates a structural distortion of the unit cell from tetragonal to orthorhombic structure at the temperature below about 150 K.

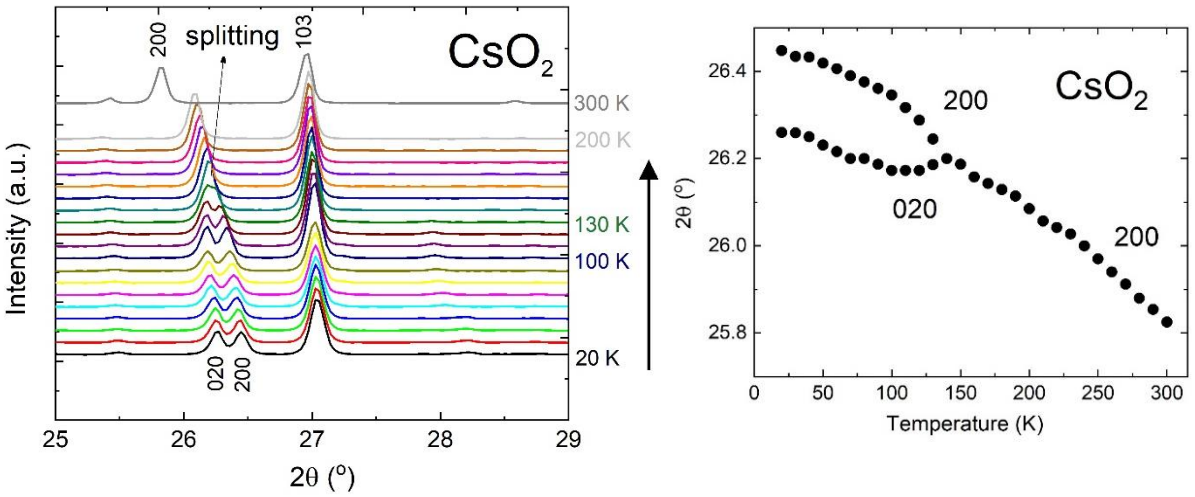

Figure 3.2. Peak broadening on cooling, followed by splitting at below about 150 K. The (200) peak experienced the splitting to be 020 and 200 indices below 150 K, suggesting a tetragonal-to orthorhombic structural change around 150 K.

The detail discussion of the XRD result in CsO_2 will be reported in separated doctoral thesis by our collaborator, Mizuki Miyajima from Okayama University. His current result proves that the orthorhombic structure (*Immm*) is obtained below 150 K and persisted in down to 20 K.

3.2. Magnetic Transition in CsO_2

The dominant feature in the magnetic susceptibility of our polycrystalline CsO_2 is the broadening peak at ~30 K. Considering the spin glass behavior observed in $RbO_{1.72}$ [119], Cs_4O_6 [47], and Rb_4O_6 [85] (see Chapter 1.3.2) which also gives a broad susceptibility maximum, we investigated this possibility in CsO_2. Yet, no significant irreversibility was observed between the field-cooled (FC) and zero field-cooled (ZFC) susceptibility at any temperature. Observation of a reversibility in the FC and ZFC curve is often apparent at the temperature where the random spins are frozen. Therefore, the possibility of spin glass can be

excluded in CsO_2. In another case, the irreversibility of FC and ZFC curve can be due to the movement of domain wall in ferromagnetic materials.

The broadening peak found in CsO_2 from the magnetic susceptibility versus temperature curve is thus likely indication of a devoloping short-range antiferromagnetic correlations below this temperature which is characteristic of low-dimensional magnetic system as also shown in other systems [120,121,122]. Superoxide is commonly regarded as a S=1/2 system because there is one unpaired electron in the π* level of the O_2^- molecule. The broad feature in the susceptibility curve is well fitted by the S=1/2 square lattice Heisenberg model recently formulated by Keith et al [123]. This model can distinguish both 1D and 2D low dimensional antiferromagnetic and ferromagnetic magnetic systems. The Hamiltonian of this system is written as:

$$\vec{H} = J\,[\vec{S}_i.\vec{S}_{i+x} + \alpha\,\vec{S}_i.\vec{S}_{i+x'}] \qquad (3.1)$$

The parameter α in the above questions denotes the ratio between two orthogonal exchange interactions, for instance: $J' = \alpha J$. For 2D antiferromagnetic ordering on a square lattice, J and J' are equal and α=1, whereas α=0 signifies an antiferromagnetic spin chain. The other alternative method of fitting the susceptibility using Feyerherm's S=1/2 Heisenberg antiferromagnetic chain model [124] :

$$\chi = \frac{Ng^2\mu_B^2}{4(2J)t}\ \frac{t^3+0.08516t^2+0.23351t}{t^3+0.73382t^2+0.13696t+0.53568} \qquad (3.2)$$

Feyerherm's polynomial approximation was obtained from Bonner and Fisher's formulation for linear chains of S=1/2 spins [125]. Bonner-Fisher described the linear chain system using the Heisenberg model. The typical 1D short-range ordering (SRO) magnetic correlation is evidenced by Bonner-Fisher type behavior in the magnetic susceptibility showing a broad peak around 30 K. As shown in Fig. 3.3, the broadening peak of CsO_2 can be fitted well by Bonner-Fisher model. The susceptibility then decreases with decreasing temperature until a suddden cusp appears at T_N~ 9 K.

Figure 3.3 shows the temperature dependence of the magnetic susceptibility, χ, and its inverse, χ^{-1}, of CsO_2 under a field-cooled (FC) H= 1 kOe condition showing anomaly at T_N= 9 K which corresponds to the antiferromagnetic ordering temperature. The χ^{-1} follows a Curie-Weiss behavior, χ (T)= $\frac{2C}{T-\Theta}$, showing the linearity as displayed in the inset in Fig. 3.3.

Here the Curie constant is C=$g^2\mu_B^2\sqrt{S(S+1)/3k_B}$ with S=1/2 and g factor=2 corresponding to O_2^- and μ_B is Bohr magneton. Fitting of the magnetic susceptibility yields for the effective magnetic moment, $\mu_{\text{eff}}=g\mu_B\sqrt{S(S+1)}$ = 1.83μ_B per O_2^- ion and a Curie-Weiss temperature, Θ, is estimated to be -41.2 K. The negative Curie-Weiss temperature suggests that the dominant exchange interactions are antiferromagnetic. The fact that μ_{eff} is slightly larger that the spin-only value of 1.73μ_B suggests the importance of orbital contributions to μ_{eff} [126].

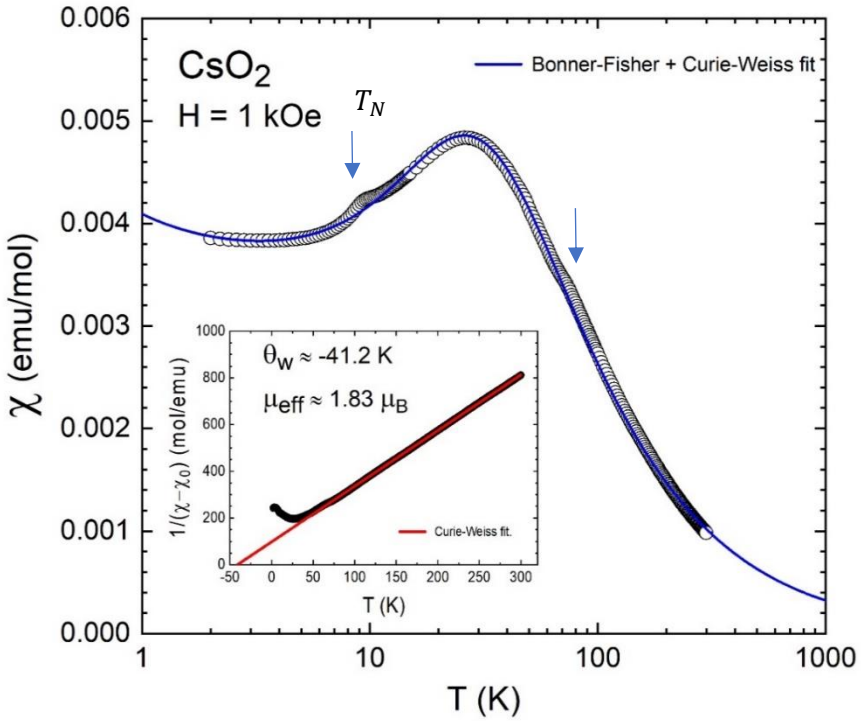

Figure 3.3. Magnetic susceptibility of polycrystalline CsO_2 as a function of temperature measured with a field-cooled (FC) mode at *H*= 1 kOe. The blue line is a fit to the Bonner Fisher+Curie-Weiss type behavior. The exchange parameter J/k_B is determined to be -42.8 K. (Inset) is the inverse susceptibility fitted by using Curie-Weiss type (red line). Based on previous reference, we predicted that anomaly at ~70 K is due to the formation of orbital ordering and at ~9 K is estimation of Neel ordering temperature [10].

3.3. μSR results in CsO_2

We have measured CsO_2 in the RIKEN-RAL muon facility in the UK and PSI in Switzerland. Due to the big internal field at the muon site, we could not observe muon spin

precession by using pulsed muon beam in the RIKEN-RAL muon facility. The pulsed muon beam can detect maximum value of internal field below about 500 Gauss. Only the decrease in the initial asymmetry which possibly means the magnetically ordered state appears causing the fast depolarization behavior faster than the time limitation of the pulsed muon facility was observed (see Fig. 3.4).

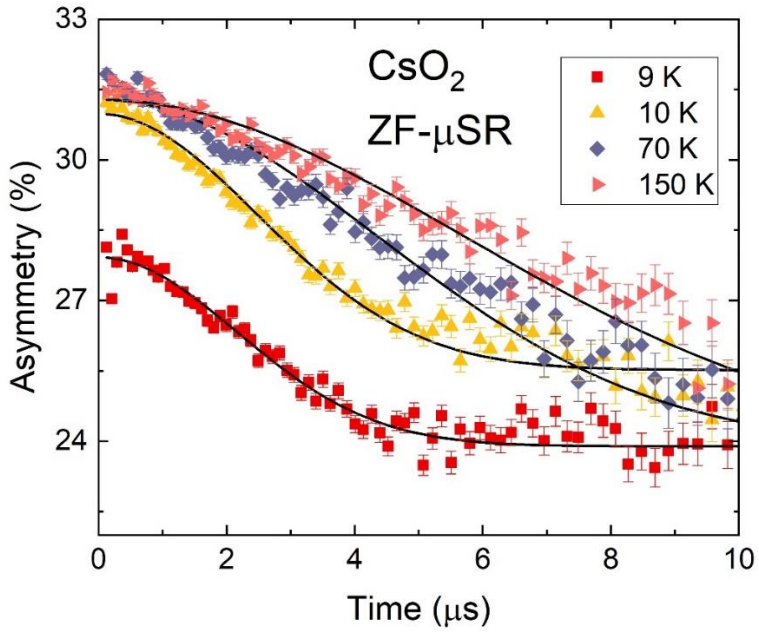

Figure 3.4. The μSR time spectra taken in the pulsed muon facility. The decreasing of initial asymmetry was observed at the temperature 9 K which possibly means the magnetically ordered state appears.

The time spectra in Fig. 3.4 can be fitted well by using the following fitting function:

$$A(t) = A\ exp(-\sigma t)^2 \qquad (3.3)$$

In order to study the detailed value of internal magnetic field which can not be detected by pulsed muon facility, we carried out μSR measurement by using continuous muon beam in PSI. Fig. 3.5 is ZF-μSR time spectra of CsO_2 measured at various temperatures. The long-time regime up to 5 μsec is indicated in Fig. 3.5 (a) to show the whole view of the time spectrum. The short-time region up to 1 μsec is displayed in Fig. 3.5 (b) in order to show fast changes in the time spectrum. The time spectrum at 10 K shows the slowly relaxing behavior. This indicates that the muon-spin is depolarizing due to the the static nuclear dipole field distributed at muon sites. As the temperature decreases, the time spectrum starts to change and the muon-spin precession behavior appears below about 9 K. With further decreasing temperature, the frequency of the muon-spin precession become larger indicating the growth of internal fields

at muon sites. The time spectrum saturates below about 2 K. The appearance of the muon-spin precession is an evidence to form LRO of unpaired electrons on O_2^- dumbbells as observed in KO_2 by the neutron scattering experiment [6]. The magnetic transition temperature, T_N, estimated from the current μSR study is to be below 10 K. Clearly, this LRO is not the magnetically induced one discussed in the NMR and other low-dimensional systems study but spontaneous one occurs in the ZF condition [17, 18, 127].

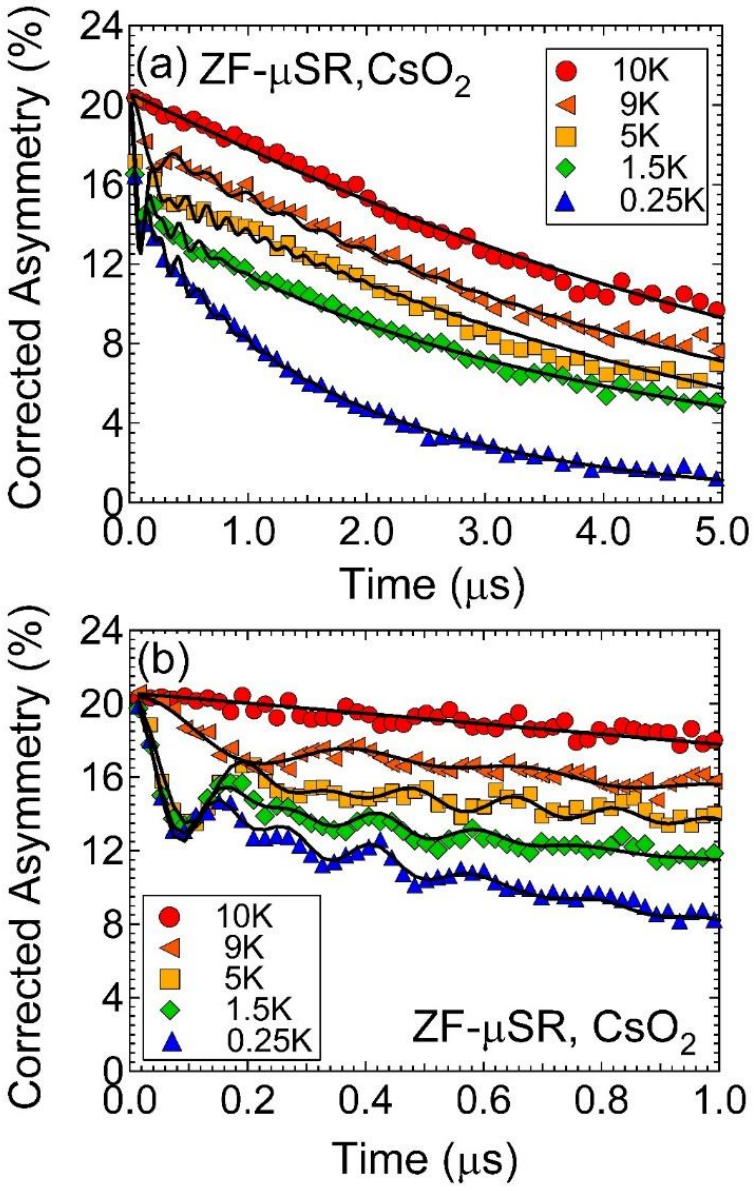

Figure 3.5. Zero field (ZF) μSR time spectrum of CsO_2 measured at various temperatures, showing (a) time spectra within the long-time region up to 5 μsec and (b) within the short-time region up to 1 μsec. The solid lines are the best-fit results by using Eq.(3.4).

In addition to this, the beating behavior on the time spectrum is confirmed. This means that there are multiple components of the muon-spin precession frequency which correspond to multiple muon-stopping sites in CsO_2. We could confirm the multiple internal fields from fast fourier transform (FFT) analysis as shown in Fig. 3.6. By using FFT, we found at least two

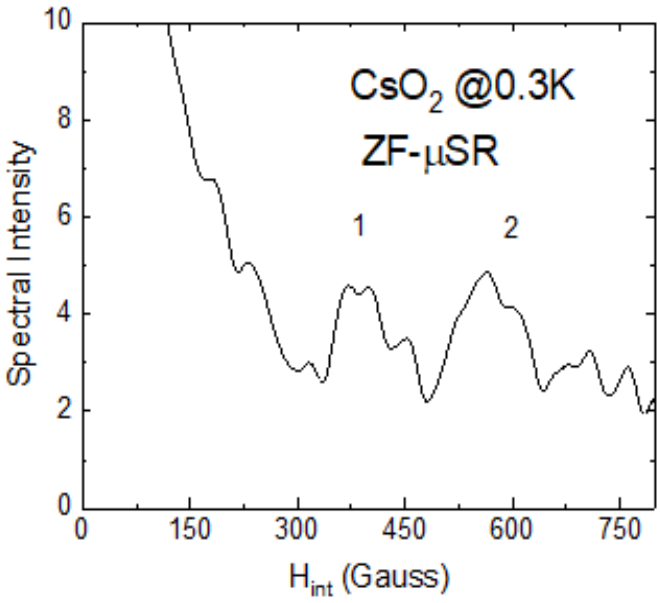

Figure 3.6. The FFT power spectra of oscillating terms at 0.3 K to visualize the distribution of internal field.

internal fields at the muon site in the μSR time spectra at the temperature 0.3 K. In order to deduce more detailed information from time spectra, the following function was used to analyze them.

$$A(t) = A_1 e^{-\lambda_1 t}\cos(\omega_1 t + \phi_1) + A_2 e^{-\lambda_2 t}\cos(\omega_2 t + \phi_1) + A_3 e^{-\lambda_3 t} \qquad (3.4)$$

In good agreement with the FFT result, we picked up the information from fitting result showing there are at least two muon-spin precession frequencies observed in the magnetically ordered state. The first and second components express the muon-spin precession behavior observed in the long-range magnetically ordered state below 10 K with precession frequencies, ω_i (i = 1, 2), and phases, ϕ_i (i = 1, 2). The A_i (i = 1, 2, 3) are the initial asymmetry parameters of each component at t=0, respectively. The λ_i (i = 1, 2) are damping rates of muon-spin precession components, respectively. Internal fields at muon sites are calculated from ω_i by using the equation, $\omega_i = 2\pi\gamma_\mu H_{int(i)}$, where γ_μ is the gyromagetic ratio of the muon spin (134.5 MHz/T) and $H_{int(i)}$ are internal fields at muon sites. The third component is to describe

the slowly relaxing behavior in the time region up to 6 μsec even after the muon-spin precession smeared out due to its damping behavior. Black solid lines in Fig. 3.5 are the best fit results subtracting small background components which were coming from muons surrounding the sample. Above 9 K, the μSR spectra is well fitted by a simple power-exponential relaxing function.

Figure 3.7 shows the components from the fitting result of time spectra by using Eq.(3.4). The temperature dependence of A_i is summarized in Fig. 3.7 (a). The total asymmetry, $A_{tot} = \sum_{i=1}^{3} A_i$ stay almost constant within the observed temperature region, indicating that all injected muons are in the diamagnetic state. No muonium state is confirmed. The A_1 increases gradually with lowering temperature and saturates below about 2 K with the value of 3-4%. Instead, A_2 is about 5% just below T_N and gradually decreases with decreasing temperature, and become to be about 2% at the measured base temperature of 0.3 K. The ratio among A_i reflects the volume fraction of each component. The temperature dependence of magnetic volume fraction is displayed in Fig. 3.8. The magnetic volume fraction starts increasing from temperature below about 10 K. Accordingly, the magnetic volume fraction of LRO is estimated as 40% (using the formulation written in Chapter 1.4.2). This means that only 2/5 of the total volume is forming LRO and others do not. Fig. 3.7 (b) indicates the temperature dependence of λ_i(i=1,2,3). The λ_1 tends to increase with decreasing temperature below T_N and shows a peak around 1 K. On the other hand, λ_2 shows a peak just below T_N and tends to decrease with decreasing temperature. The λ_3 stays almost constant with smaller value compared to other components.

Fig. 3.7 (c) displays the temperature dependence of $H_{\mathrm{int}(i)}$. Both components of $H_{\mathrm{int}(i)}$ appears just below about 10 K and gradually increases with decreasing temperatures. The $H_{\mathrm{int}(i)}$ tends to saturate below 2 K (temperature independent) and their saturated values are estimated to be about 540 and 390 G. The temperature dependence $H_{\mathrm{int}(i)}$ are simply fitted by using the Brillouin function in order to estimate the spin value of J [128]. The solid line in Fig. 3.7 (c) are the best-fit results in the case of J=1/2, 1 and 3/2. But, it is hard to judge the spin value within the experimental error due to the scattering of the data.

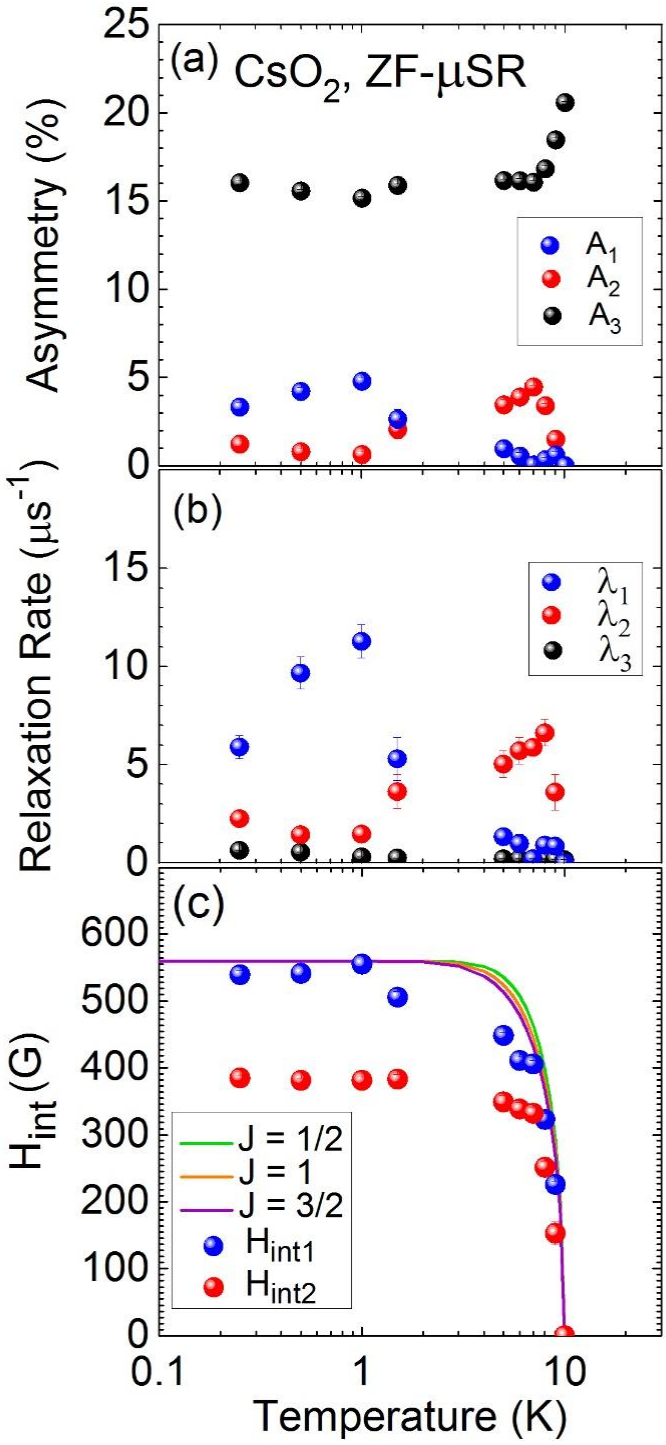

Figure 3.7. Temperature dependences of (a) initial asymmetries, A_i, (b) depolarization rates, λ_i, and (c) internal fields at the muon sites, $H_{\mathrm{int}(i)}$, of all components are achieved from the analysis of the time spectra of CsO_2 by using Eq. (3.4).

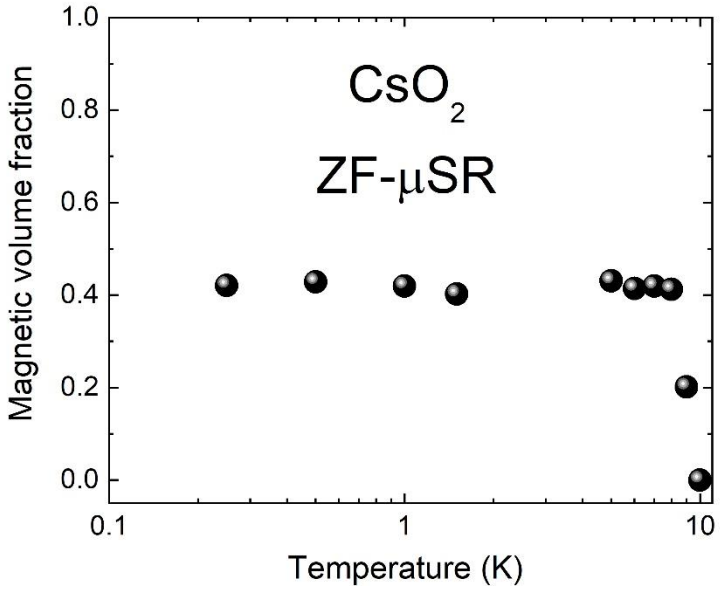

Figure 3.8. The magnetic volume fraction obtained from the analysis of ZF-μSR time spectra of CsO_2 by applying Eq. (3.4)

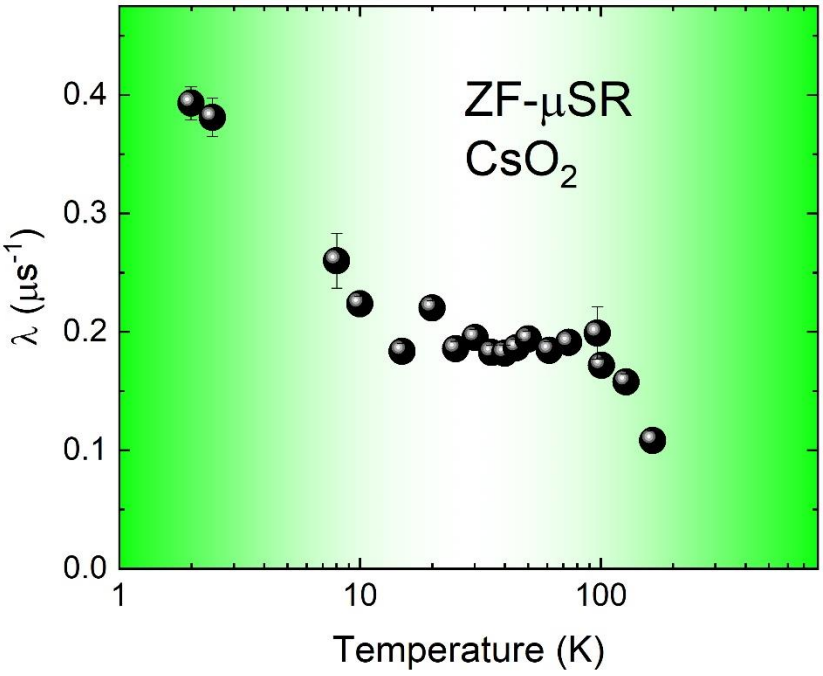

Figure 3.9. Temperature dependence of the muon spin depolarization rate in CsO_2 by μSR measured at RIKEN-RAL Muon Facility. The green background displays the area which is strongly affected by temperature.

In order to investigate the spin dynamics and a whole magnetic behavior, we extended the measurement of the depolarization rate in ZF beyond the magnetic transition temperature

using pulsed muon facility. Fig. 3.9 exhibits the temperature dependence of λ up to ~200 K. The λ is gradually increasing with decreasing temperature and saturates once below about 100 K. The NMR relaxation behavior also became less dependent of temperature below about 100 K [18]. In further decreasing temperature, λ starts to increase again below the transition temperature 10 K.

The spin dynamics was also checked by LF measurement. The LF- μSR spectra at 0.3 K is displayed in Fig. 3.10. There is still small depolarization remained in the time spectra under 1000 G indicating that a dynamic behavior is still exist. Generally, all electronic fluctuations must be suppressed by applying LF 1000 G.

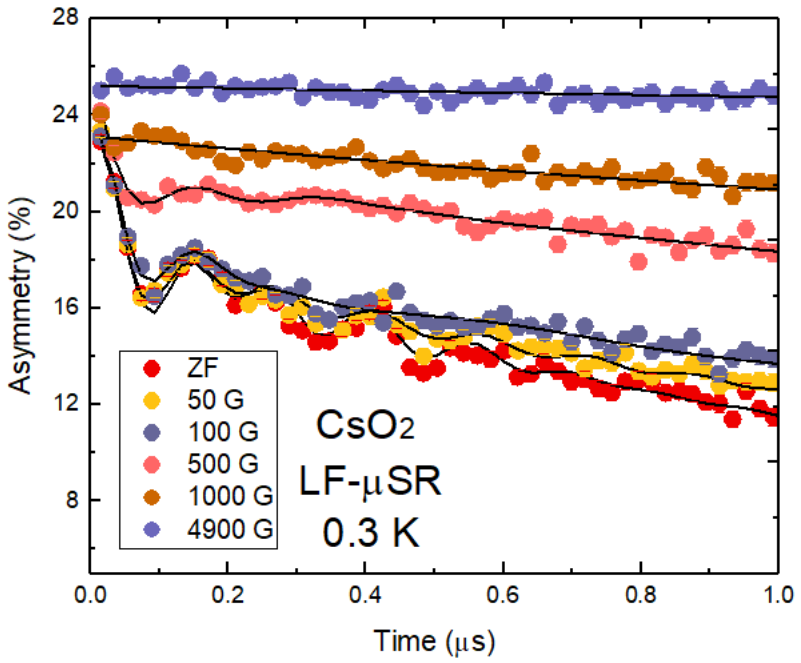

Figure 3.10. Longitudinal-field μSR time spectra of CsO_2 measured at several external fields at 0.3 K. Black solid line are the best-fitting results.

Following the earlier report from NMR, mentioning the existence of TLL in CsO_2 under field condition at the temperature in between 15-40 K [18], we also tried to track the TLL phenomena by μSR. The measured LF spectra, indicated in Fig. 3.11, were fitted to the simple power-exponential relaxing function as follow:

$$A(t) = Ae^{-\lambda t} \qquad (3.5)$$

It is dificult to observe the differences due to the very tiny change of the time spectrum in CsO_2 under high-field condition. There is no difference of the time spectrum by changing of the temperature under high field 2.35 T and 4.7 T. As indicated in Fig. 3.12, there is almost no changing of the relaxation rate by changing of temperature (λ~constant). We could not observe an indication of suppression of spin dynamics as well as TLL phenomena which has been proven by NMR.

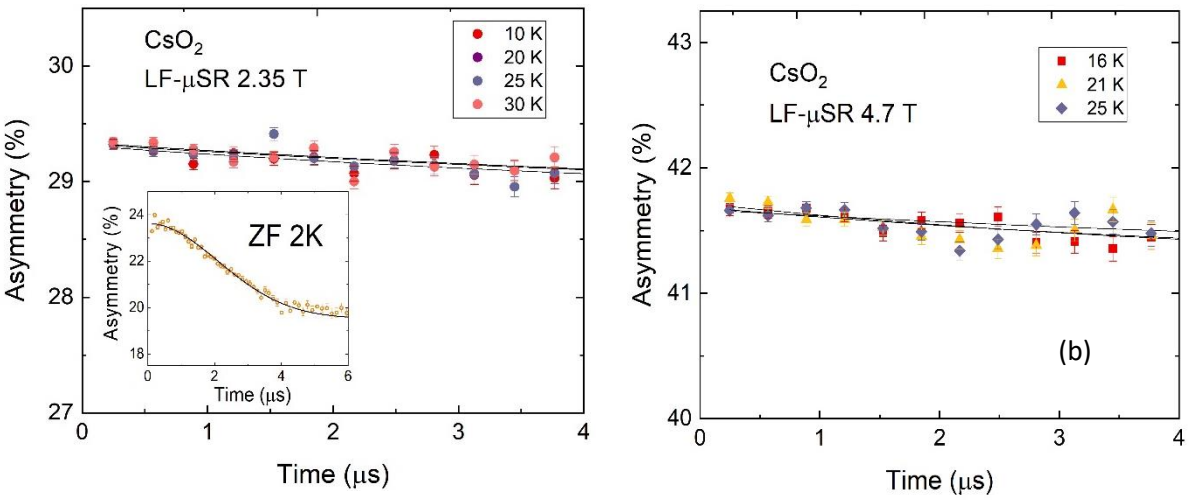

Figure 3.11. Experimental muon decay asymmetry A(t). Data in (a) LF $\mu_0 H$= 2.35 T. Inset: Data measured in zero applied field and (b) $\mu_0 H$= 4.7 T on the powder CsO_2 sample.

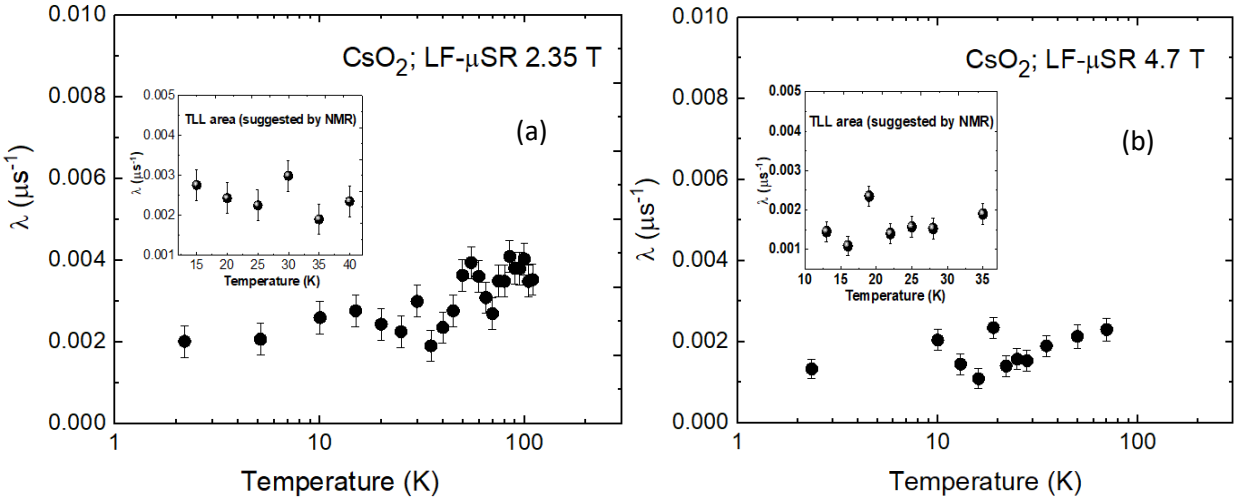

Figure 3.12. Relaxation rate λ at $\mu_0 H$= 2.35 T and $\mu_0 H$= 4.7 T

3.4. Discussion

The study of crystal structure in CsO_2 is important because it is strongly correlated with its magnetic properties. From our data, we found that the structural phase transition occur from tetragonal to orthorhombic at the temperature below about 150 K. The structural phase transition temperature has a small difference compared to single crystal CsO_2 in which occured at the temperature of 190>T>9.6 K. The structure persists in orthorhombic symmetry down to 20 K which will be reported in separated PhD Thesis by our collaborator. The low-temperature structure is also consistent with the previously reported orthorhombic structure in CsO_2 by Rosenfeld et al [8] and Riyadi et al [10].

CsO_2 is an example of quasi-one dimensional systems, such as $BaCo_2V_2O_8$ [127]. The one dimensional magnetic interaction is followed by the 3D magnetic ordering at low temperature. It is well established that long-range magnetic order is suppressed in magnetic systems whose interactions are low dimensional. The prototypical example is the S=1/2 Heisenberg antiferromagnetic chain (S=1/2 HAFC). In real S=1/2 HAFC compounds, weak interchain coupling induces long-range magnetic order although with a suppressed ordered moment and reduced Neel temperature compared to Curie-Weiss temperature. In general, long-range order does not exist in purely one-dimensional systems due to strong fluctuations of the order parameter. Due to this effect, the magnetic transition in quasi-one-dimensional systems occur at the temperatures lower than those given by mean-field calculations. As the temperature decreases, the system crosses over from 1D to 3D and long-range static magnetic order appears. This sudden change of dimensionality can be understood from the fact that one-dimensional chains cannot display a stable long-range antiferromagnetic order for $T > 0$ K. As long as the spins are dynamic, the 1D character is sustained. However, as soon as the fluctuations slow down and the system become static, the spins are locked into a 3D-order by (weak) inter-chain interactions.

A zero-field μSR experiment has detected three-dimensional (3D) magnetic ordering at T_N ~9 K in CsO_2. Following the result of high field magnetization measurement (Chapter 1.3.2), the contribution of interchain coupling and/or XXZ anisotropy were suggested due to the inconsistency around the saturation field [64]. This interchain coupling might drive the formation of 3D LRO at ~9 K in CsO_2. The interchain coupling *J'* should be relatively small compared to *J*. The estimation of interchain coupling value must be very important for the next study.

Based on ZF-μSR result, there is no field-induced magnetic ordering as suggested by NMR result in CsO_2. CsO_2 has spontaneous LRO without magnetically induced one. This is an indication that weak interchain coupling in CsO_2 can be generated spontaneously without the presence of external field.

Morover, LRO in CsO_2 can be regarded to form domain structures in a sea of non-LRO. This is because only 40% magnetic volume fraction is formed stating that 2/5 of the total volume is forming LRO and others do not. We believe that this is an intrinsic behavior of the sample because we have confirmed the sample quality from the beginning. One possibility is because one-dimensional magnetic ordering at higher temperature regime prevents the formation of fully three-dimensional AF ordering at the ground state. The reduced magnetic volume fraction was also reported in other systems. The magnetically ordered volume fraction decreases in the doped $RENiO_3$ (RE=rare-earth element) suggesting the formation of intrinsic phase separation. The phase separation between ordered AF and disordered state was suggested in this system [129]. For CsO_2, it seems that there is a mixture in between Neel ordering and quantum condensed state. The one-dimensional magnetic interaction could be remained seated even in the ground state. The coexistence of 1D and 3D behavior observed in well-known quasi 1D system, $KCuF_3$, measured by inelastic neutron scattering [26]. As an addition, the non-linear increases observed by high-field magnetization at 1.3 K (Fig. 1.13) suggests a strong quantum fluctuation in CsO_2. Based on the LF-μSR experiment, essentially static AF ordered state, that could coexist with moderate dynamic fluctuations, progressively develop below the magnetic ordering temperature since the small relaxation behavior still exists under LF 1000 G.

Absence of Tomonaga Luttinger Liquid

The absence of TLL phase is confirmed from our current μSR result under LF condition. We could not see any observation of field-induced TLL phase from μSR result. The first observation of TLL probed by μSR was observed in $(C_7H_{10}N)_2CuBr_4$ (DIMPY) [92]. We expect any nuclear contribution to the muon relaxation to be fully quenched at this field and therefore we are only probing the electronic spin dynamics of TLL behavior indicated by the linear behavior (power-law behavior). Following the μSR measurement in DIMPY, we could not see the similar tendency of the relaxation rate from LF measurement. Our μSR result showed the weak relaxation at the TLL temperature ($15 < T < 40$ K) under high external field, without any change in relaxation rate at the temperature range of expected TLL ($15 < T < 40$ K).

The possibility is that all spins have been depolarized under very high field 2.35 T and 4.7 T. Since there is no spin dynamics remained, it is hard to observe the presence of TLL phenomena (which measures the degree of quantum fluctuations inside the material). Another possibility is that could be due to the different time window in between NMR and μSR. NMR experiments usually focus on the very fast fluctuations. One suggestion is that the characteristic time in the spin fluctuations is longer than the characteristic time of observation for thermal muons but shorther than that for NMR. The fast fluctuations result in the weak relaxation from the muon time window. Furthermore, the study of TLL phenomena observed by μSR is not yet applicable in many systems. The further study is still needed.

The possibility of the existence of TLL can be determined by the temperature dependence of magnetic susceptibility measurement. As reported in reference [78], TLL also applies to 1D antiferromagnets. In CsO_2, a broad peak is observed in magnetization measured as a function of temperature. In another spin-1/2 Heisenberg chain system, $Cu(C_4H_4N_2)(NO_3)_2$, a broad peak at 6.89 K is also observed in temperature dependence of magnetic susceptibility [130] in which with an increasing field, the peak moves gradually to the lower temperature, signaling a crossover to a low-temperature TLL regime. The peak started to be shifted to the lower temperature by applying external field 6 T which is close to the broad peak temperature. Since 1 K corresponds to 1 T of energy electron spin, we at least need to apply the external field close to the value in where the broadening peak is observed. Following this way, in CsO_2, with an increasing field up to 7 T, no observation of peak shifting was observed. Furthermore, we need to measure up to ~30 T (the broad peak was observed at ~30 K) to check whether the peak shifting is observed or not in order to clarify the presence of TLL behavior in CsO_2. But, insufficient time prevented further measurement.

Muon Stopping Position in CsO_2

Fig. 3.13 displays the minimum potential positions in CsO_2 estimated from DFT calculations by describing of isosurface areas with the exact energy region from the potential minimum positions (yellow surface). The crystal structure used in this calculation followed the result from S. Riyadi et al [10]. Dark marks in those extracted figures indicate exact locations of the local minimum potential. Those local minimum positions are expected to be regarded as initial stopping sites for injected muons. Two different muon positions were revealed in the

current study around the oxygen dumbbell. Those different sites are caused by the titling of the oxygen dumbbell against to the *c*-axis. Assuming the same AF spin structure with that observed in KO_2 [6], we find two probable muon sites in the vicinity of the dumbbell oxygen, namely (0.7373; 0,2500;0.5859) and (0.6999;0.2567;0.5762). We found that muons stop near an oxygen atom. This is because an injected muon has a positive charge and preferentially stops close to anions, which have negative charges. The two muon stopping position confirms that calculation result has a good agreement with the experimental result which show two internal field at the muon site.

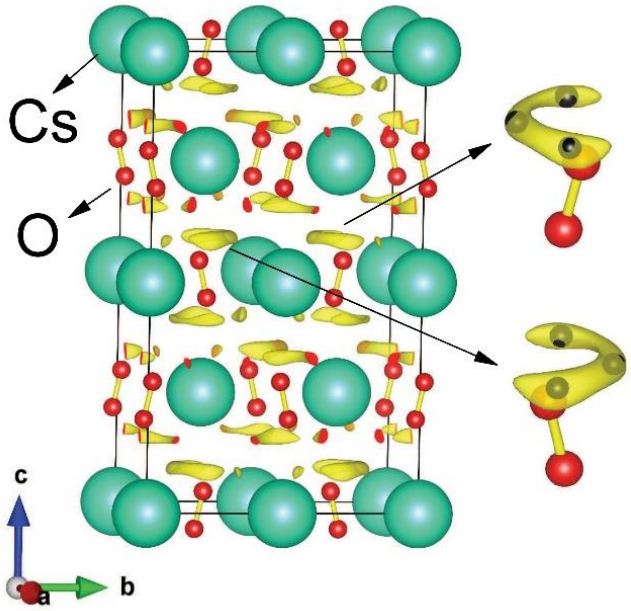

Figure 3.13. Minimum potential positions estimated from density functional theory (DFT) calculations. There are two possible muon positions around the O_2^- dumbbell. The difference of those positions are caused by the tilting of the O_2^- dumbbell against crystal axes. Isosurface areas which is about 200 meV higher region in the energy from the local minimum potential positions are displayed by yellow regions. Dark red marks in those isosurface regions are local minimum potential positions.

This work is a preliminary study of AO_2 probed by μSR. The value of internal field obtained from experimental μSR result can be a reference for further study of calculation work. When muon-spin precession is observed, precession frequencies give us information of internal fields originating from the surrounding magnetic moments at muon sites. The muon-site itself is a very important parameter to study the hyperfine interaction between muon and electrons

and to discuss ordered states of electronic spins in magnetic materials. These internal fields are estimated on the basis of the dipole-dipole interaction between muon spins and surrounding magnetic moments. Such combined studies involving experimental and computational techniques can allow us to discuss the spin structures and also estimation of magnetic moment. Especially in low-dimensional system, such as CsO_2, strong quantum fluctuations are suggested to attribute to the reduction of effective magnetic moment. In order to prove such a reduction of magnetic moment, more detail calculations of the muon site and the interaction between muon and surrounding moments are inevitable. The neutron diffraction can be also considered for determining the magnetic moment in the ground state.

Chapter 4

Result and Discussion on Rubidium Superoxide (RbO_2)

4.1. Structural Phase Transition in RbO_2

We measured synchrotron X-ray diffraction (XRD) at beamline (BL)-8A and 8B in KEK Photon Factory (PF) after confirming the sample quality from the result of laboratory XRD using Cu targets. The laboratory XRD data showed that the sample quality is good indicated by the observation of RbO_2 peak from X-ray profiles as shown in Fig. 4.1.

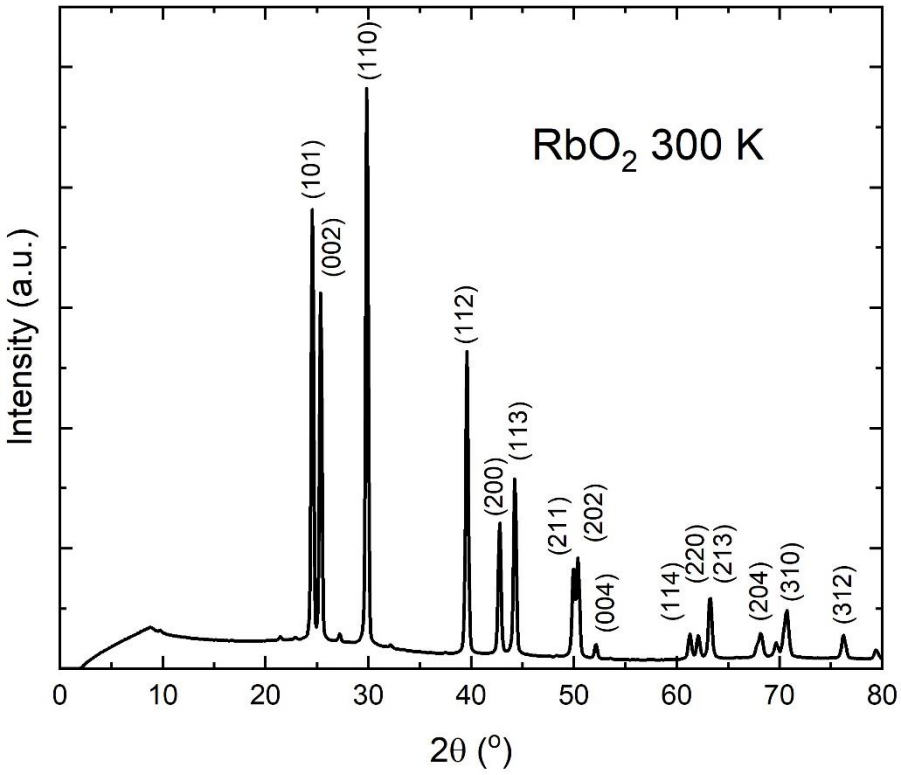

Figure 4.1. XRD pattern of RbO_2 measured at room temperature using laboratory XRD. All Bragg peaks represent the presence of RbO_2 phase referred from Reference [131]. This data was measured using Cu targets (λ CuKα_1=1.5406 Å).

We also measured low-temperature XRD using laboratory XRD machine with Mo targets (λ MoKα_1=0.7094 Å). But, there is no significant change of XRD pattern was observed if we compared high- and low-temperature XRD pattern. Since the Rb K-edge (13.396 keV) is

close to the wavelength of MoKα (17.480 keV) and thus there is a high possibility that samples containing Rb are highly absorbing towards a Mo source.

In order to check the detail low-temperature structure from XRD pattern, the synchrotron XRD measurement was performed. The measurement was done at the temperature 30 K< *T*< 300 K. From the room temperature synchrotron XRD result, we confirmed that RbO_2 adopts the tetragonal structure: space group *I/4mmm*. Fig. 4.2 shows the fitted XRD pattern at the room temperature, with lattice parameters of *a*=*b*= 4.21815 Å and *c*= 7.00144 Å, in agreement with those reported for single crystal RbO_2 [12].

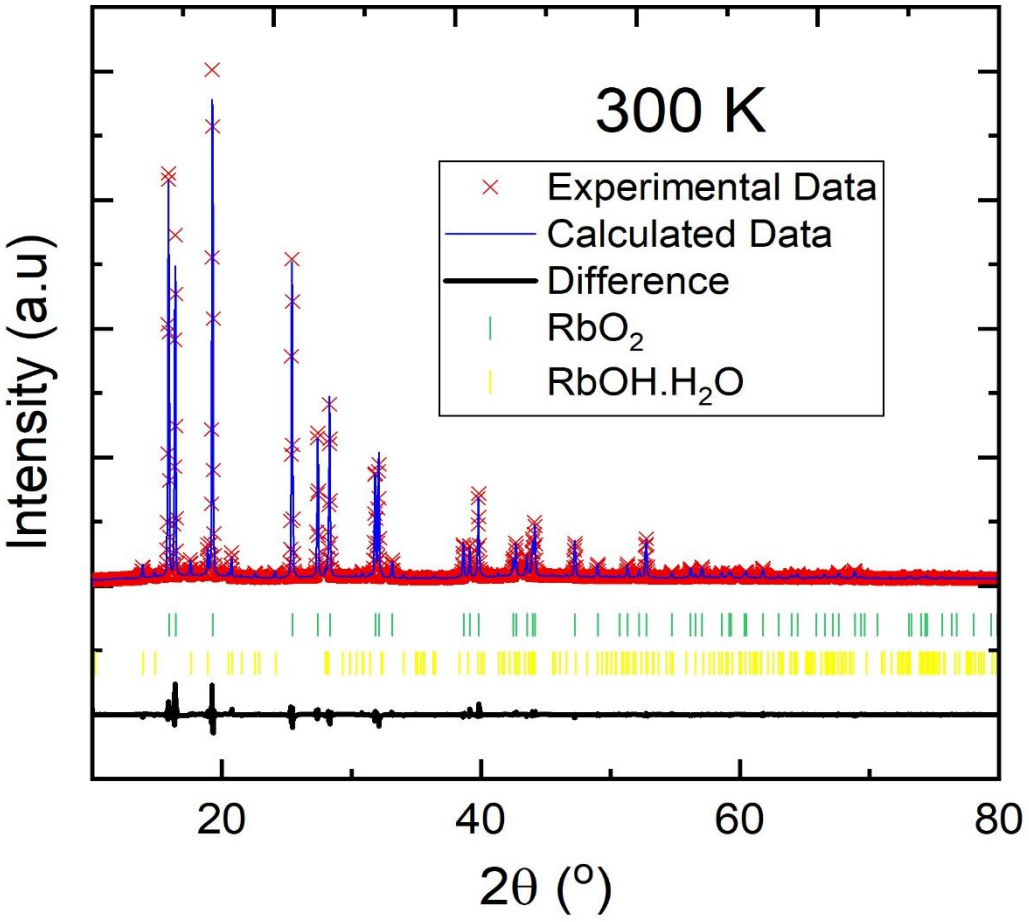

Figure 4.2. Room temperature XRD pattern of RbO_2 using λ, 0.99917Å. Observed data (red crosses), the calculated pattern (blue line), difference between observed and calculated pattern (black line), the candidate peak positions (green bar for RbO_2 and yellow bar for $RbOH.H_2O$).

An impurity phase, $RbOH.H_2O$ (5% by weight), was also present but does not contribute to the magnetic response of the sample. At room temperature, the dioxygen anion

are oriented along the *c*-axis of the unit cell with the position of each atom: Rb (0; 0; 0) and O (0; 0; 0.41332). The O-O distance is estimated to be about 1.22 Å. The O-O bond length determined from the X-ray powder diffraction data is considerably shorter than 1.35 Å expected for the superoxide anion. The final weighted, R_{wp}, for room temperature structure was converged to 4.36%, indicating a good fit to the experimental data.

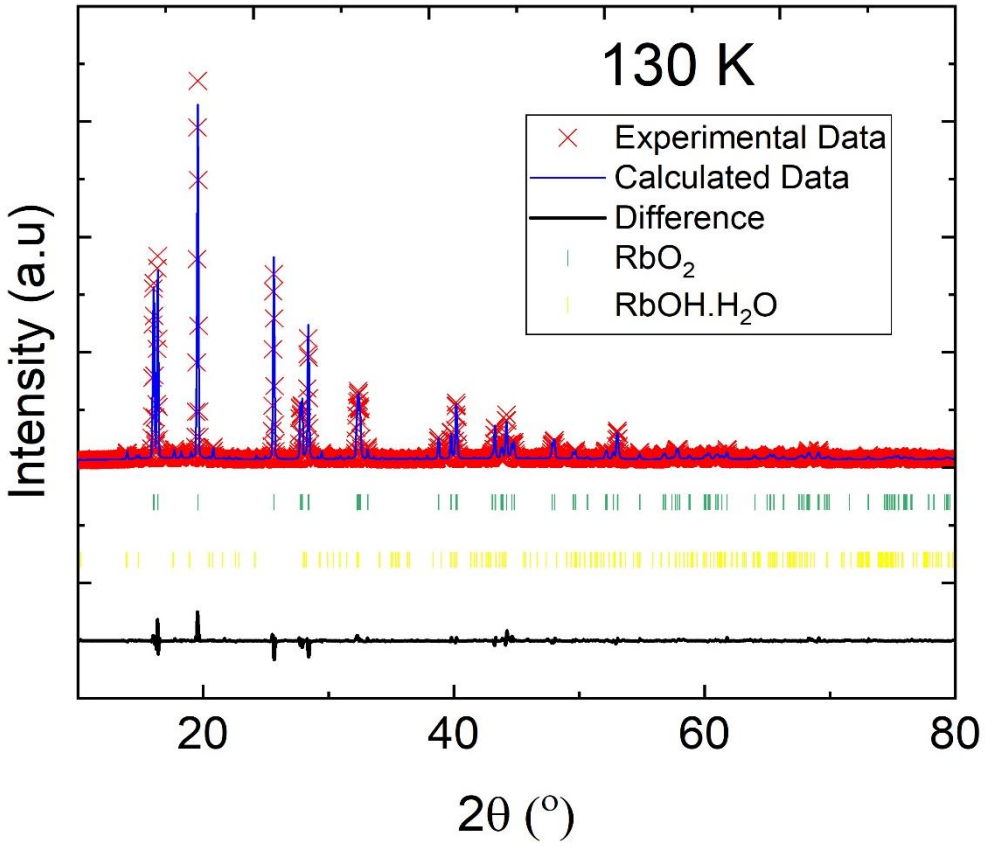

Figure 4.3. XRPD pattern of RbO_2 at the temperature of 130 K. The XRD pattern can be fitted well by using orthorhombic structure (space group: *Immm*). Observed data (red crosses), the calculated pattern (blue line), difference between observed and calculated pattern (black line), the candidate peak positions (green bar for RbO_2 and yellow bar for $RbOH.H_2O$).

Figure 4.3 shows the X-ray diffraction pattern of RbO_2 at 130 K. We confirmed that RbO_2 at temperature 130 K adopts the orthorhombic structure: space group *Immm*, with lattice parameters of *a*= 4.14322 Å, *b*= 4.16321 Å and *c*= 7.00720 Å. The position of each atom: Rb (0; 0; 0) and O (0; 0; 0.40372). The $RbOH.H_2O$ impurity (orthorhombic, space group: *Cmc21*) does not undergo a phase transition with the lattice parameter *a*= 4.09719 Å, *b*= 11.22561 Å and *c*= 6.03020 Å. The final weighted, R_{wp}, for room temperature structure was converged to

5%, indicating a good fit to the experimental data. O-O distance is estimated to be about 1.35 Å which is in good agreement with the bond length of superoxide.

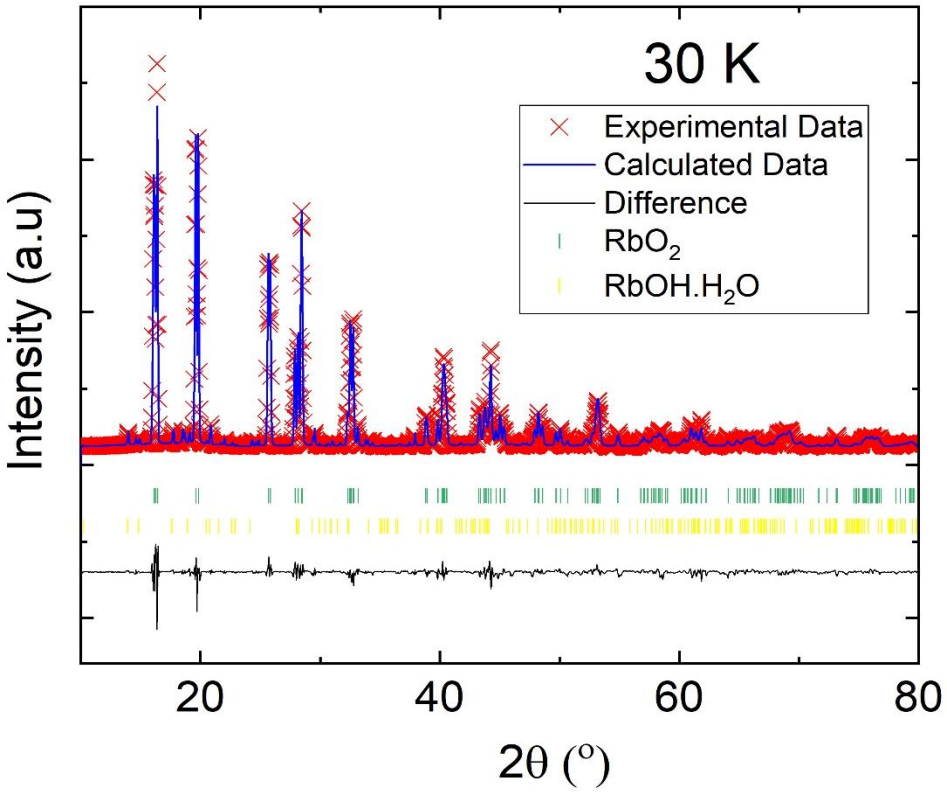

Figure 4.4. XRPD pattern of RbO_2 at the temperature of 30 K. The XRD pattern can be fitted well by using orthorhombic structure (space group: *I*112/*m*). Observed data (red crosses), the calculated pattern (blue line), difference between observed and calculated pattern (black line), the candidate peak positions (green bar for RbO_2 and yellow bar for $RbOH.H_2O$).

Figure 4.4 shows the X-ray diffraction pattern of RbO_2 at 30 K. Monoclinic structure (space group *I*112/*m*) significantly improves the fit with lattice parameters of a= 4.10634 Å, b= 4.14513 Å, c= 7.00413 Å and γ= 90.628°. The position of each atom: Rb (0; 0; 0) and O (0; 0; 0.40243). The angle of γ in the monoclinic structure also agree well with the reported structure in single crystals where γ~ 90.69 °. Even the R-factor is still beyond 5% for this analysis result (The R-factor for the data at 30 K is ~6.67%), the monoclinic structure *I*112/*m* can be a possible low-temperature structure in RbO_2.

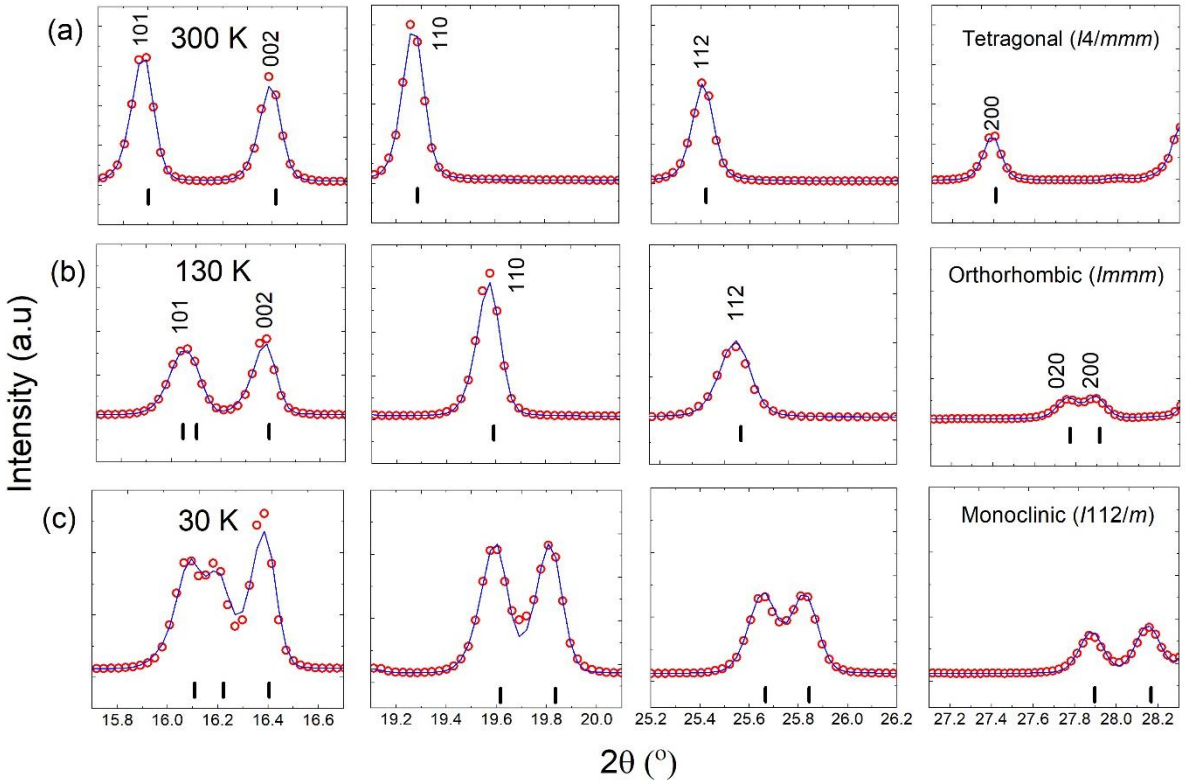

Figure 4.5. XRD patterns of RbO_2 measured at 300 K, 130 K, 70 K and 30 K around $2\theta = 15^o$ and 29^o. The blue line is the fitting result of the peaks and thin black bars show position of peaks. (a) The room temperature structure can be fitted well by tetragonal structure. (b) The 200 peak becomes broader indicating a split into 020 and 200 peaks indicating the change in the crystal structure from tetragonal to orthorhombic. This split is caused by the change in the crystal structure from tetragonal to orthorhombic. (c) Splits of 110 and 112 peaks indicate that the lattice symmetry of RbO_2 becomes lower than orthorhombic. The split of each peak remains at least down to 30 K.

The evolution of peak broadening as a function of temperature was studied in order to determine whether there is a well-defined phase transition below room temperature. Our preliminary synchrotron XRD study suggests that an obvious change appears below 170 K, indicated by the splitting of the peak of 200 to be 020 and 200 which are confirmed at the position of 28^o as shown in Fig. 4.5 (b). We define the transition temperature as Ts_1. A structural transition from tetragonal to orthorhombic appears below about 170 K down to 100 K which can be refined by using the space group *Immm* (see Fig. 4.3). The same crystal structural transition from tetragonal to orthorhombic around 150 K is reported to appear in CsO_2.

Based on the fitting result, below 100 K, the orthorhombic structure seems not suitable in RbO_2 since the refinement using orthorhombic *Immm* model did not converge smoothly. Moreover, another change in the lattice symetry was observed below about 100 K. This change is identified by splits of 110 and 112 peaks as indicated in Fig. 4.5 (c). We define this transition temperature as Ts_2. At this temperature, the lattice symmetry is predicted to be lower than othorhombic since some fundamental peaks experience splitting. The analysis results show that monoclinic structure possibly exists at temperature below about Ts_2 and remains down to 30 K.

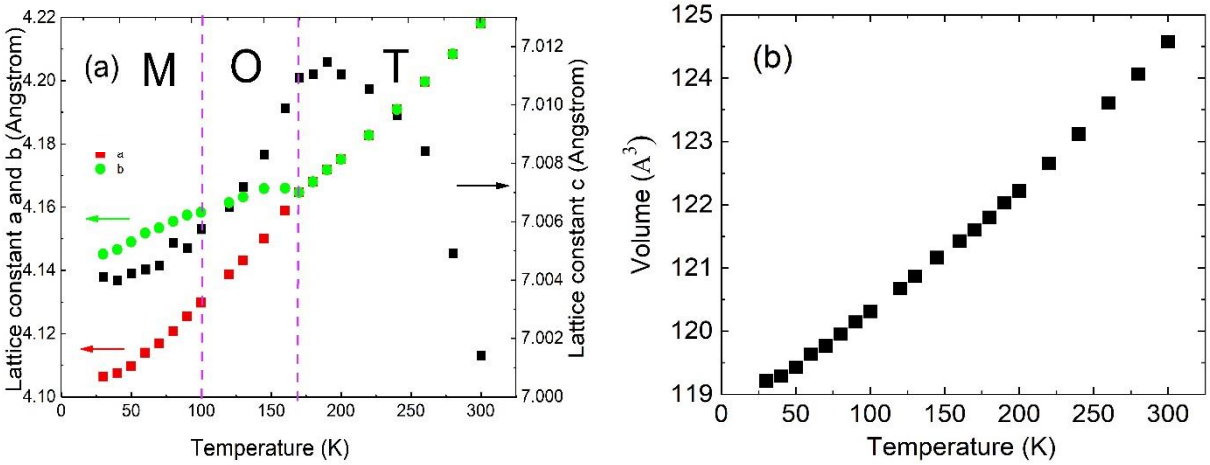

Figure 4.6. (a) The temperature dependence of lattice constant *a*, *b*, and *c* ; T= Tetragonal, O= Orthorhombic; M= Monoclinic (b) The evolution of unit cell with temperature.

The evolution of the lattice parameters with temperature is shown in Fig. 4.6 (a). Apart from the orthorhombic distortion temperature below about 170 K indicated by the lattice parameter $a \neq b$, the other noteworthy feature is an increase of the *c* lattice parameter below 300 K. The crystal *c*-axis length increases with decreasing temperature which would be due to the effect of decreasing thermal fluctuations on cooling resulting in the reduction of the dumbbell's libration. This drives the enhancement of the projected length of the dumbbell to the *c*-axis, which leads to the increasing of the *c*-axis. Below 200 K, the *c* lattice parameter shortens due to coherent positions of the dumbbells. Below 100 K, the *c* lattice parameter can be regarded as constant.

The volume of the unit cell decreases by decreasing the temperature as represented in Fig. 4.6 (b). At room temperature, the O-O distance should be relatively short. This could be due to the thermal activation results in precession/libration of the dumbbells around the *c*-axis at high temperature. At room temperature, O_2^- dumbbell axis should not be fixed at the *c*-axis

because of the libration of molecule. Since we can see the time-averaged structure by XRD, the tetragonal structure might hold the time averaged direction of the dumbbell parallel to the *c*-axis at the room temperature. If the O_2^- dumbbell axis is tilted from the *c*-axis, the projected length of the O-O distance to the *c*-axis is decreased. If we see the effective (time averaged) projected length of the dumbbell, it may be reduced.

Weak incommensurate peaks were appeared below Ts_1 in the orthorhombic phase, which had been reported in Ref [8]. The appearance of small peak was found for instance at $2\theta = 18.25^o$. Below Ts_1, these peaks are shifted with decreasing temperature and their positions are fixed at the temperature below about Ts_2 indicated by the black arrow in Fig 4.7. In our present structural refinement, we ignore these superlattice peaks because of their weak intensity.

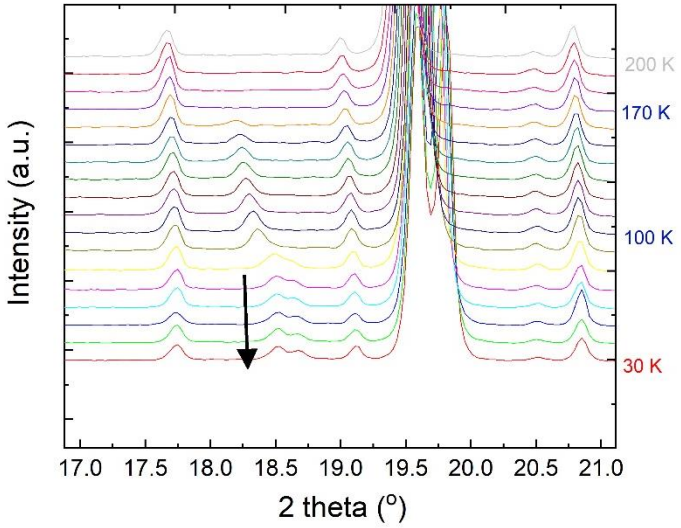

Figure 4.7. The feature of possible incommensurate peak in RbO_2

4.2. Magnetic Transition in RbO_2

Figure 4.8 displays the temperature dependence of the magnetic susceptibility times temperature, χT, measured in 1 kOe after the field-cooling procedure. The inset in Fig. 4.8 (a) is the temperature dependence of χ showing no appearance of a broad peak which was observed in CsO_2. This is a large difference from the case of CsO_2 in which the clear peak characterized by the low-dimensional magnetic interaction is observed around 30 K (see Fig. 3.3). The sharp peak around 15 K is the signature of the appearance of the magnetic transition. Thus, this peak temperature can be defined as T_N.

The insets in Fig. 4.8 (b) and (c) are temperature dependences of the 110 and 200 peak positions observed by XRD measurement on RbO_2. Those peak positions were estimated by the fitting using the Gaussian function. Crystal transition temperatures from tetragonal to orthorhombic and from orthorhombic to lower symmetry are indicated as Ts_1~170 K and Ts_2~100 K, respectively. There are two anomalies observed in the temperature dependence of χT as seen in Fig. 4.8 (b) and (c). One is around 100 K and the other is around 170 K. Those anomalies are coincident with Ts_1 and Ts_2.

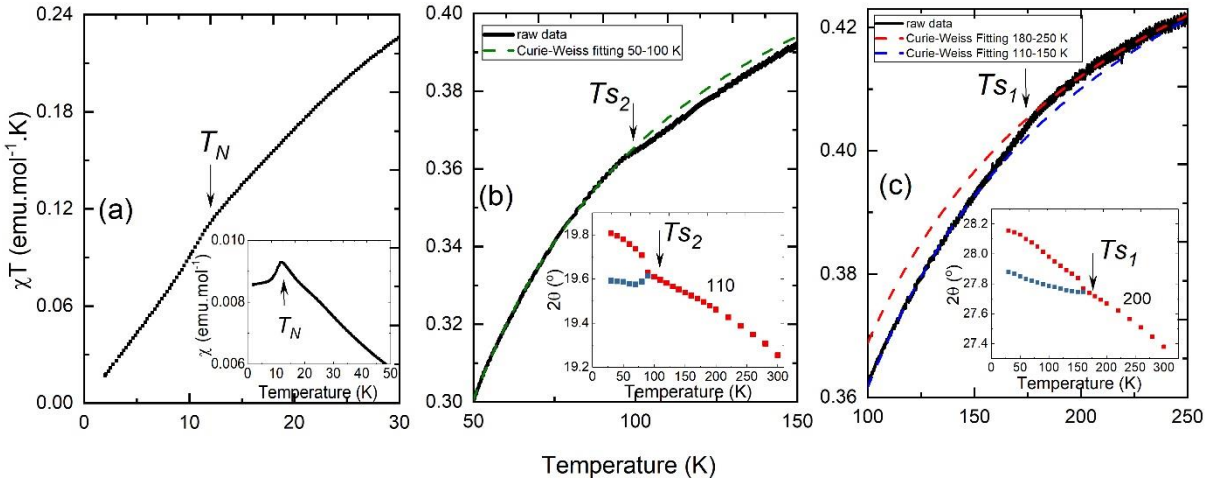

Figure 4.8. Temperature dependence of magnetic susceptibility times temperature (χT) measured in RbO_2 from (a) 2 K to 30 K, (b) 50 K to 150 K and (c) 100 K to 250 K. Black arrow in (a) indicates the Neel ordering temperature (T_N). Insets in (b) and (c) are temperature dependences of 2θ values of 110 and 200 peaks. Those peak positions were estimated by the fitting using the Gaussian function. Ts_2 in (b) and Ts_1 in (c) are temperatures at where 110 and 200 peaks split with lowering temperature. Anomalies in the magnetic susceptibility shown in (b) and (c) are almost coincident with Ts_1 and Ts_2 as indicated by black arrows.

Accordingly, we analyzed the temperature dependence of magnetic susceptibility by using the Curie-Weiss law within temperature ranges between 250 K and Ts_1, Ts_1 and Ts_2, and then between Ts_2 and 50 K which is enough above from T_N. Broken lines in Fig. 4.8 (b) and (c) are the best fit results. For each temperature region, we got detail values of Curie constant, C, to be as 0.467, 0.473 and 0.467 emu.K.mol^{-1}, respectively. Values of Curie-Weiss temperature, Θ, were also estimated to be as -26.49(27), -30.86(18) and -27.56(6) K, respectively. Negative values of Θ indicate that the magnetic interaction between O_2^-

dumbbells is AFM as well as the case of CsO_2. The estimated values of Curie constants are bigger than the expected value from g=2 and S=1/2 indicating the importance of orbital contributions.

As shown in Fig. 4.9, the high-field magnetization result for RbO_2 as a function of magnetic field up to 60 T at the temperature below T_N, 1.3 K and 4.2 K, showed the absence of upturn curvature as observed in another alkali-metal superoxide system, CsO_2 [64]. There is no significant difference of the magnetization pattern from these two temperatures measurement except for the magnetization value at 1.3 K is higher than that of 4.2 K. The magnetization value is estimated to be about 0.47 μ_B at 1.3 K under applying external field 60 T. This value is smaller than that observed in CsO_2 which has magnetization value 1 μ_B at 60 T (see Fig. 1.13).

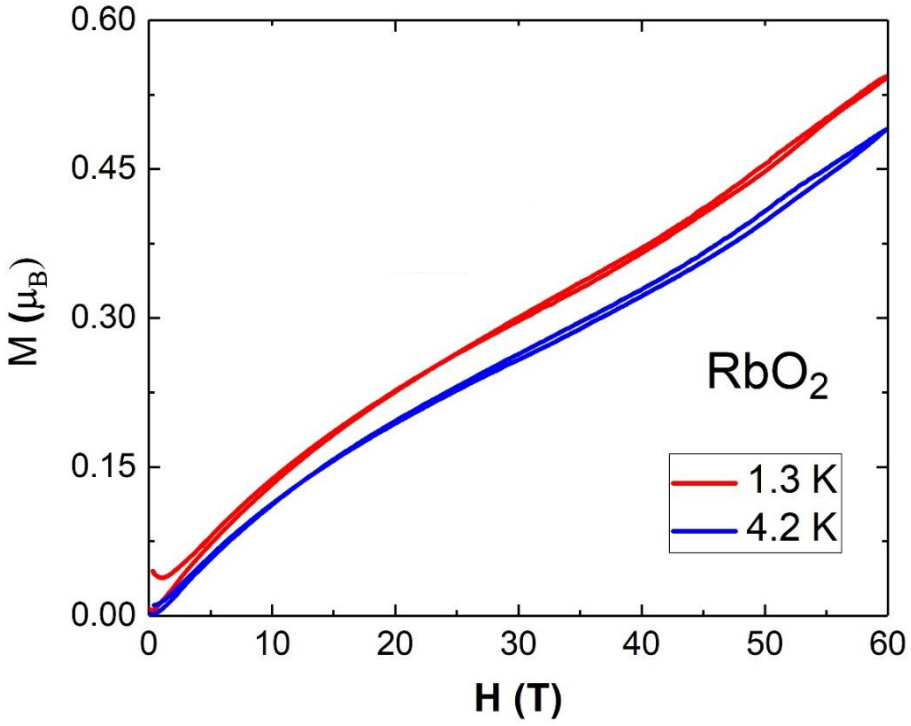

Figure 4.9. The magnetization curve measured on polycrystalline RbO_2 at 1.3 K and 4.2 K up to the magnetic field of 60 T.

4.3. μSR results in RbO_2

We have measured RbO_2 in the RIKEN-RAL muon facility in the UK and PSI in Switzerland. As the same case with CsO_2, using the pulsed muon facility at RIKEN-RAL, we could not observe clear muon-spin precession although the decrease in the initial asymmetry

around the suggested T_N ~ 15 K was observed. Such significant reductions in the initial asymmetry in the magnetically ordered satate are often observed because this behavior corresponds to the average of the invisible oscillation. This ordered state might accommodate the fast muon-spin precession as well as the case of CsO_2 which has to be confirmed by a continuous muon source.

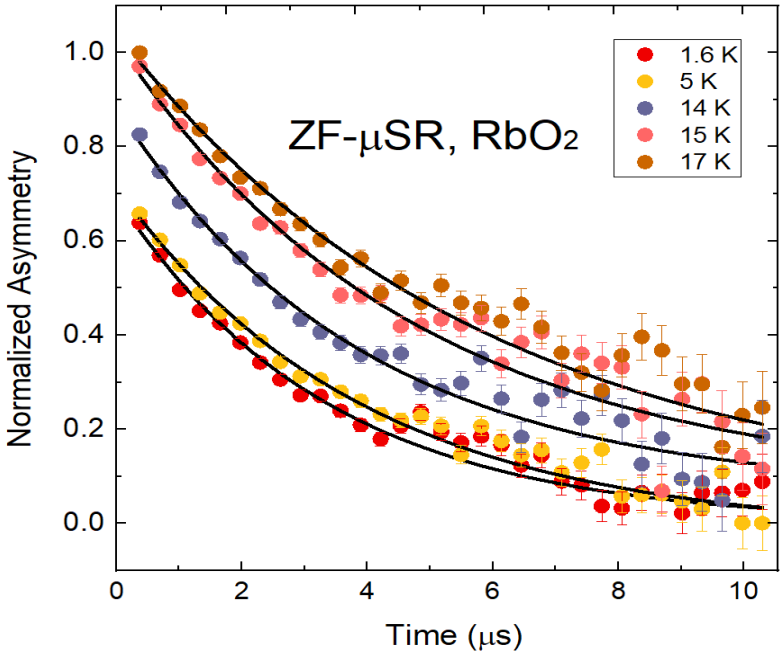

Figure 4.10. The μSR time spectra taken in the RIKEN-RAL muon facility.

The time spectra in Fig. 4.10 can be fitted well by using the following fitting function:

$$A(t) = A\ exp\ (-\lambda t) \qquad (4.1)$$

In order to study the detailed value of internal magnetic field, we carried out μSR measurement by using continuous muon beam in PSI. The sample used in this measurement was the best among all RbO_2 samples. The magnetic transition temperature is estimated from the current μSR study to be ~15 K as shown in Fig. 4.11 which is close to the estimation of magnetic ordering from the magnetic susceptibility measurement. μSR result displayed the existence of long-range magnetic ordering in the muon sites by the appearance of oscillation spectrum. In addition to this, the beating behavior on the time spectrum was confirmed. This means that there are multiple components of the muon-spin precession frequency caused by inequivalent muon stopping sites. A single smooth field distribution could not produce this beating. In order to deduce more detailed information from the time spectra, the following function is used for the ZF time spectra below T_N.

$$A(t) = A_1 e^{-\lambda_1 t}\cos(\omega_1 t + \phi_1) + A_2 e^{-\lambda_2 t}\cos(\omega_2 t + \phi_1) + A_3 e^{-\lambda_3 t} \qquad (4.2)$$

We estimated that there are at least two muon-spin precession frequencies observed in the magnetically ordered state corresponding to two inequivalent muon sites in RbO_2. The first and second components express the muon-spin precession behavior observed in the long-range magnetically ordered state below 15 K with precession frequencies, $\omega_1$and ω_2 . A_1 and A_2, and $\lambda_1$and λ_2 are initial asymmetries and relaxation rates of the first and second components, respectively. The third component is to describe the slowly relaxing behavior. Solid lines in Fig. 4.11 are the best fit results by Eq. 4.2. The total asymmetry, $A_{tot} = \sum_{i=1}^{3} A_i$ stayed almost constant within the observed temperature region. Fig. 4.12 (a) shows the temperature dependence of asymmetry. The signal increases substantially at lower temperatures as the magnetically ordered domains grow at the expense of the paramagnetic ones whose volume fraction is hidden in parameter A_3 which is non-oscillating component. The third term, in Eq. 4.2, accounts for the fact that on average, for a completely random distribution of the directions of the local field in polycrystalline compound, one-third of all muons experience an internal field along their initial spin direction. As a consequence, they will not precess, but will contribute to the $e^{-\lambda_3 t}$ term. The asymmetries show almost the temperature independent close to T_N. The magnetic volume fraction determined from the ratio of the amplitude of oscillation components to the total asymmetry is estimated to be ~100%. As indicated in Fig. 4.12 (c), magnetic volume fraction is about 100% which indicates that almost all magnetic spins undergo the magnetic ordering. Fig. 4.12 (b) indicates the temperature dependence of λ_i (i=1,2,3). The associated relaxation rates λ_1 and λ_2 show the fairly strong temperature dependence especially the data point close to T_N. Instead, the λ_3 stays almost constant with smaller value compared to other components.

Fig. 4.14 displays the temperature dependence of $H_{\mathrm{int}(i)}$. H_{int}(T) near T_N was clearly and precisely achieved. Both components of $H_{\mathrm{int}(i)}$ appears just below about 15 K and gradually increases with decreasing temperatures. The $H_{\mathrm{int}(i)}$ tends to saturate below 7 K (temperature independent) and their saturated values are estimated to be about 723 G and 340 G. Internal fields at muon sites are calculated from ω_1 by using the equation, $\omega_i = \gamma_\mu H_{\mathrm{int}(i)}$, where γ_μ is the gyromagnetic ratio of the muon spin (2π x 13.45 kHz/G) and $H_{\mathrm{int}(i)}$ are internal fields at muon sites. It is useful as an approximate visual illustration of the internal

magnetic field distribution and for comparing the measured μSR signal with the best fit theory function from the time domain. The obtained frequencies and the resulting field distribution map agrees well with fast Fourier transform of the μSR time spectra (Fig. 4.13).

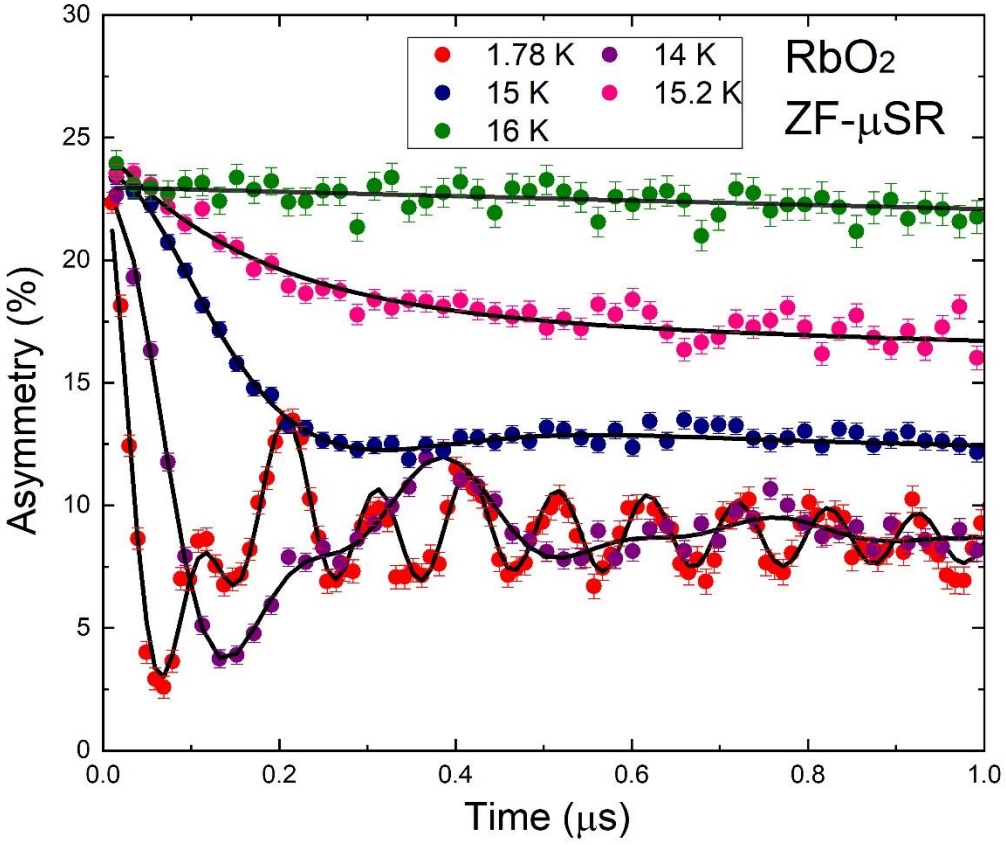

Figure 4.11. Zero-field μSR time spectra of RbO_2 measured at several temperatures. Clear muon-spin precession was observed below about 15 K. Solid line (black) are the best-fitting results obtained using Eq.(4.2). The precession frequency increases with decreasing temperature, showing the increase in the internal field at the muon sites.

In order to achieve the information of the dimensionality of the magnetic interaction, following Eq. 4.3 was applied to the temperature dependence of H_{int} [133,134]:

$$H_{int}(T) = H_0[1 - (\frac{T}{T_N})^{\alpha}]^{\beta} \qquad (4.3)$$

where β is the critical parameter to describe the dimensionality of the magnetic interaction and α is to express the spin excitation at low temperatures. The results obtained from H_{int1} and H_{int2}

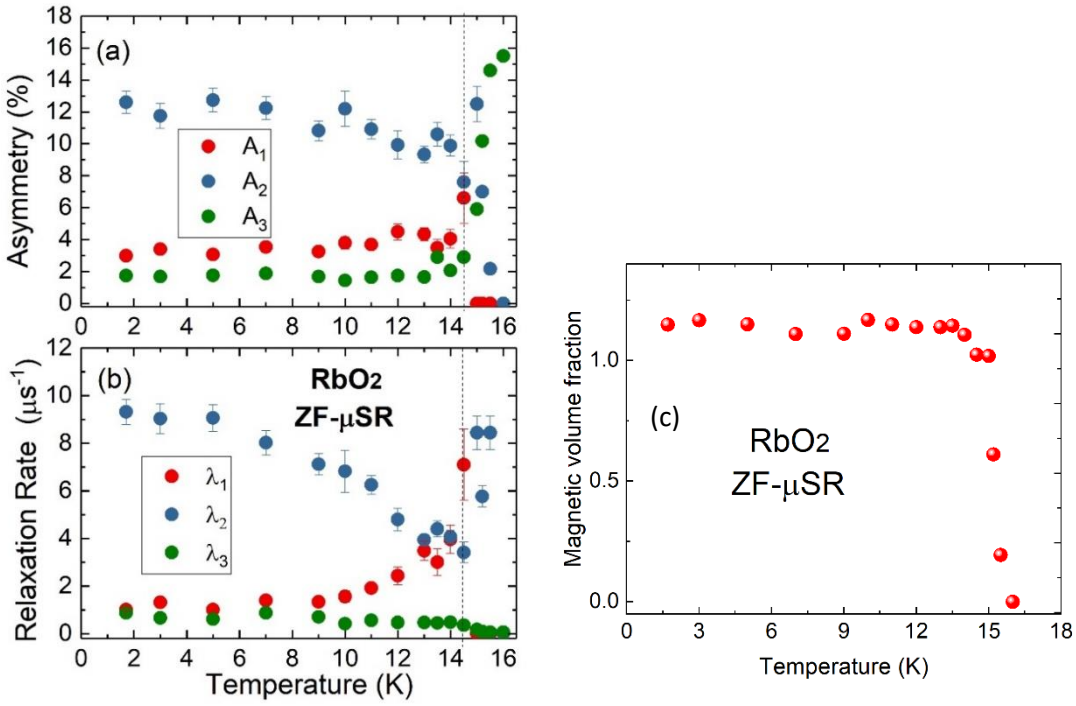

Figure 4.12. Temperature dependences of (a) initial asymmetries, A_i, (b) depolarization rates, λ_i (c) The magnetic volume fraction obtained from the analysis of ZF-μSR time spectra of RbO_2 by applying Eq. (4.2)

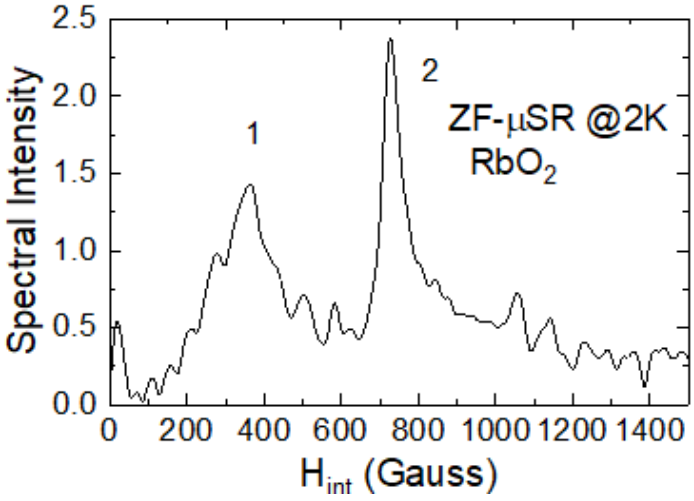

Figure 4.13. The fast fourier transformation power spectra of oscillating terms at 1.78 K to visualize the distribution of internal field.

are slightly different, so that we took averaged values. Those are T_N= 15.1(2) K, β= 0.36(6) and α= 2.88(43). Although it is not so clear to judge the dimensionality of the magnetic interaction from these results due to fairly big fitting errors, those results could support the appearance of the static long-range ordered state on the basis of the three-dimensional (3D) Heisenberg magnetic interaction [133,135]. This result exclude from RbO_2 a possibility of the existence of the low-dimensionality in the magnetic interaction which is expected in CsO_2.

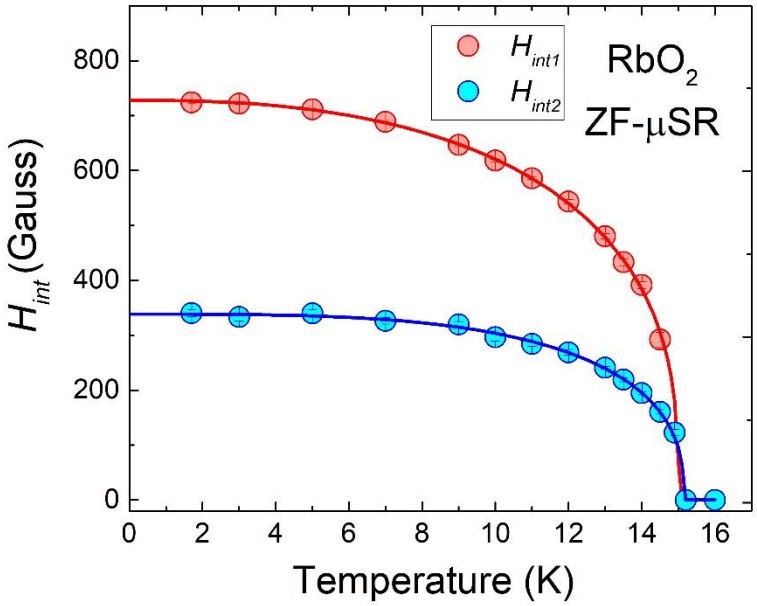

Figure 4.14. Temperature dependence of local internal field H_{int1} and H_{int2}. The solid line is T-dependence of the critical region from which T_N and β were extracted.

We extended the measurement of the depolarization rate in ZF beyond the magnetic transition temperature using pulsed muon facility. Fig. 4.15 exhibits the temperature dependence of λ up to ~200 K. With decreasing temperature, the spin dynamics is gradually suppressed and the fluctuation frequency gradually comes in the μSR time window. This is observed as the increase of λ down to 100 K and saturates once below about 100 K. In further decreasing temperature, λ starts to increase again below the transition temperature 15 K.

The effect of applied LF is to decouple the depolarization of the muon spin due to dynamic or fluctuating moments [136]. In order to investigate whether spins on O_2^- dumbbells are frozen or not, LF was applied at 1.78 K. As displayed in Fig. 4.16, there has been a complete recovery of the asymmetry at long times by applying 1000 G with no evidence for any

remaining dynamic fields. Measured time spectra are almost flat in the long-time region and shift upward parallel with increasing LF, indicating no dynamic fluctuating spins left in RbO_2 at this temperature. This results means that all spins on O_2^- dumbbells are frozen from the view of the characteristic time window of μSR which is from 10^6 to 10^{11} Hz.

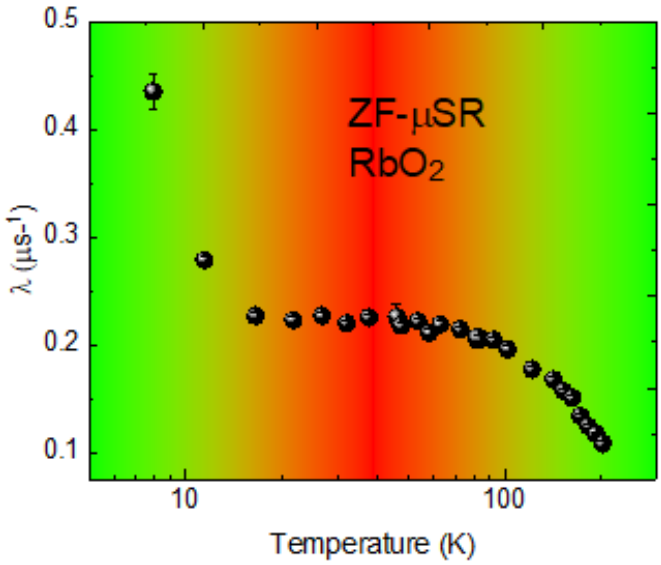

Figure 4.15. Temperature dependence of the muon spin depolarization rate in RbO_2 by μSR measured at RIKEN-RAL Muon Facility. The green background displays the area which is strongly affected by temperature.

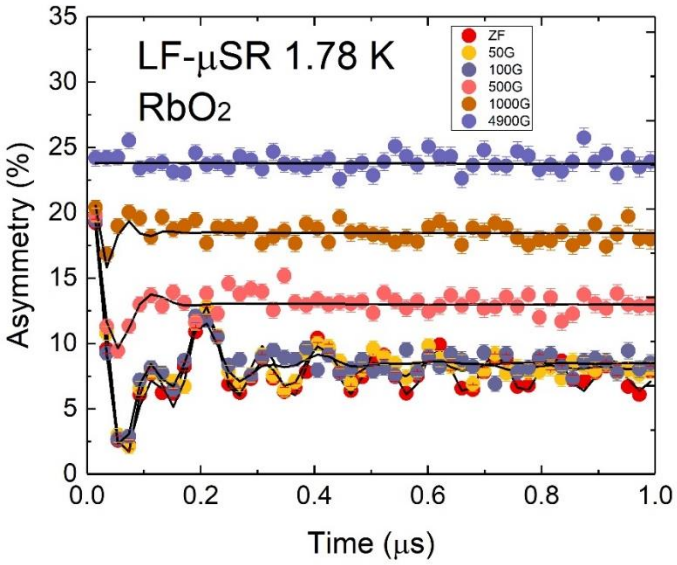

Figure 4.16. Longitudinal-field μSR time spectra of RbO_2 measured at several external fields at 1.78 K. Black solid line are the best-fitting results. The polarization is shifted to the higher values indicating the presence of static magnetism.

4.4. Discussion

First, we discuss the structural phase transition in RbO_2. The peak splitting observed from x-ray diffraction measurement indicated the tetragonal to orthorhombic transition at the temperature below about 170 K. The refinement using orthorhombic structure can be fitted well down to temperature 100 K. The refinement at low-temperature (below 100 K) cannot be fitted well by using orthorhombic (*Immm*) structure. Moreover, the monoclinic structure (*I*112/*m*) which has lower symmetry than orthorhombic can be a possible low-temperature structure of RbO_2.

The possible lower symmetry than orthorhombic was indicated by some splitting of fundamental peaks and the observation of possible incommensurate peak below 100 K which is an indication of further structural phase transition at this temperature. The lower symmetry could be driven by the Jahn-Teller or another symmetry distorted nanodomains involving short-range correlated shifts and tilts of the anions. This behaviour cannot be probed easily by x-ray powder diffraction.

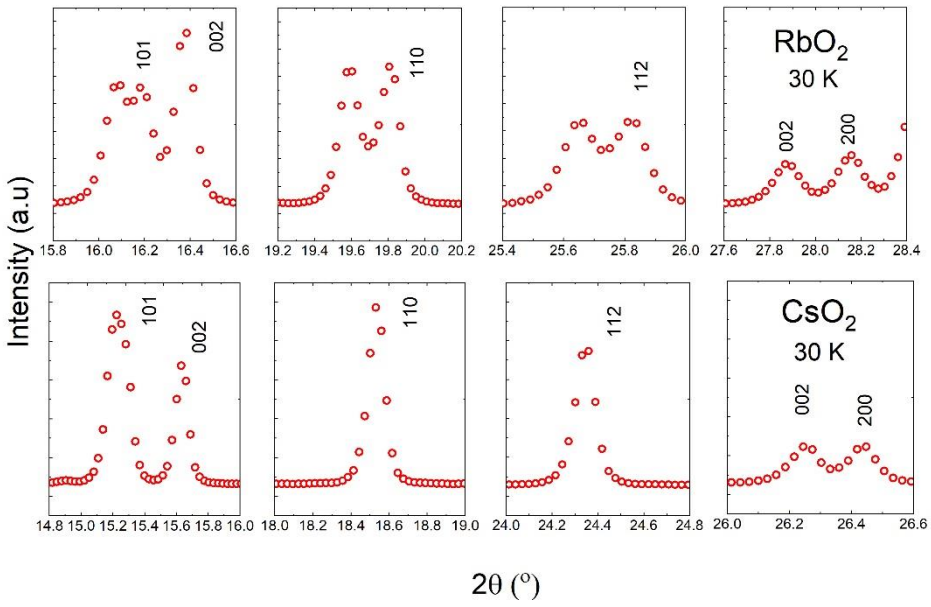

Figure 4.17: Peak splitting in the fundamental peak of RbO_2 compared to CsO_2 at 30 K. Since the same splits of the 101, 110 and 112 peaks are not observed in CsO_2, the lattice symmetry of RbO_2 is lower than that of CsO_2.

Our XRD data could explain that RbO_2 has lower lattice symmetry than CsO_2 since RbO_2 has more complicated XRD peak especially at low temperature. Large amount of peaks occurs in the powder pattern in low symmetry crystal system. As shown in Fig. 4.17, some

fundamental peaks in RbO_2 i.e: 101, 110 and 112 experience splitting which is not observed in CsO_2 at low temperature.

We here reported the first investigation of the microscopic magnetic nature of a polycrystalline RbO_2 sample using μSR. The observation of precession frequency in zero external field is a undisputable evidence for the spontaneous ordering of the electronic spins, placing the onset of long-range oredering at T_N ~15 K. The intriguing feature of the RbO_2 compound is that ZF-μSR resolves two discrete frequencies υ_1=6 MHz and υ_1=11 MHz at 1.78 K, corresponding to the static local fields at the muon site of 340 G and 723 G, respectively. In case of RbO_2, the system tends to adapt whole three-dimensional system since the magnetic volume fraction satisfied 100%. The full magnetic volume fraction indicates that the absence of quantum fluctuations is inevitable. The LF-μSR spectra reveals the expected behavior for static magnetism.

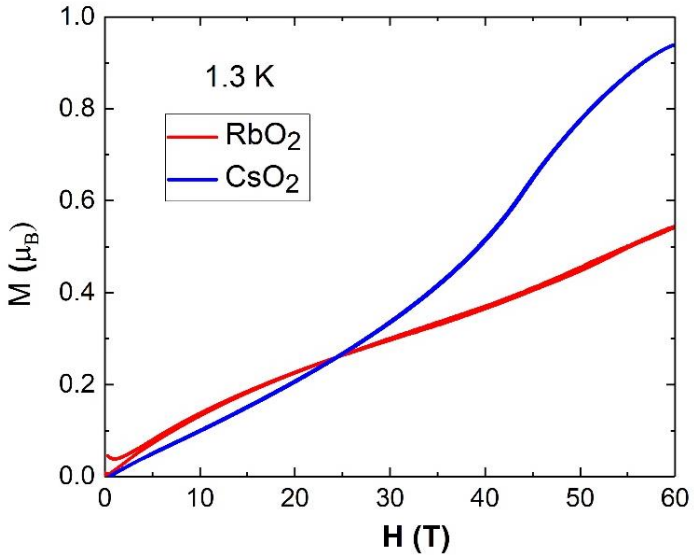

Figure 4.18. Magnetization curve measured on polycrystalline of RbO_2 at 1.3 K up to the magnetic filed of 60 T (red line). For the comparison, the result of high-field magnetization measurement in CsO_2 is presented (blue line) [64].

Our result of high-field magnetization in RbO_2 showed the absence of up-turn curvature (absence of low-dimensional magnetic interaction). The saturated magnetization can be achieved by applying field 60 T in CsO_2 (see Fig. 4.18), while in RbO_2 in order to reach the saturated magnetization, the higher applied field might be needed. If we extrapolate the value of magnetization in RbO_2, the saturated field could be approached by applying nearly two times larger external field (~120 T). This difference could be affected by the different magnetic

exchange interaction between these two systems. The spin-flop field, H_{SF}, can be expressed using the exchange field H_E and the anisotropy field H_A by using relation: $H_{SF} = \sqrt{2H_E H_A}$ [137]. Since the exchange field is strongly correlated to the saturated field, RbO_2 should have H_E higher than CsO_2. The exchange field, H_E, can be expressed as $H_E = \frac{zJS}{g\mu_B}$, where z is the number of nearest neighbor spins. CsO_2 has z=2 which correspond to a 1D spin chain. If we assume that the three-dimensional magnetic interaction exist in RbO_2, this system should have more than 2 nearest neighbor spins. Another possibility which can drive the difference of magnetization value in both systems is that the magnetic exchange interaction, *J*, in RbO_2 is bigger than that in CsO_2.

Even though RbO_2 and CsO_2 are isostructural compounds each other at room temperature, we found through the current study that there are some big differences in their low-temperature crystal structures, magnetic properties and the spin dynamics of the O_2^- dumbbell. Taking into account changes in the lattice symmetry as displayed in Fig. 4.17, it is strongly expected that those differences in magnetic properties are caused by differences in the lattice symmetry between RbO_2 and CsO_2, especially below T_{S2}. It is suggested that the lattice symmetry of RbO_2 below T_{S2} is to be lower compared to that of CsO_2. The current study revealed that differences in the magnetic properties between RbO_2 and CsO_2 are caused by changes in lattice symmetries. We also supposed that those changes in lattice symmetry were caused by changes in the orientation of the O_2^- dumbbell.

A possible mechanism which can be supposed to understand changes in the lattice symmetry is on the basis of differences in the ionic radius between Rb and Cs. The shorter ionic radius of Rb than that of Cs makes the interatomic distances in the ab plane shorter. This causes the rigid structure, resulting in that the deformation of the orthorhombic structure below 170 K smaller than that of CsO_2. In order to release the free energy from the lattice, RbO_2 changes the lattice symmetry again below T_{S2} although the final symmetry in the ground state is still unclear. In the case of KO_2, which is another isostructural compound, the crystal structure was predicted to change to be triclinic at temperature below T_N~ 7 K. This triclinic structure lifts up the degeneracy of π* orbital as well as the Jahn-Teller effect and generates the interlayer AFM coupling leading the formation of the 3D AFM ordering.

Another possible mechanism is the appearance of electronic orbital orderings in RbO_2. In the case of KO_2, Kim et al. verified from the electronic structure calculation that the emergence of the O 2p ferro-orbital (FO) ordering is essential to achieve the experimentally observed AF structure [6, 63]. By considering the tilting of O_2^- dumbbell in the AF structure,

the band gap opening and the FO ordering occur simultaneously. Following this scenario, AF interaction in RbO_2 could be explained suggesting a possible appearance of the orbital ordering. It was predicted that the emergence of in-plane antiferro-orbital ordering to be most favored in RbO_2 based on untilted dumbbells in the *c*-direction [54].

It was suggested that the O_2^- dumbbell in CsO_2 tilted about 5^o from the *c*-axis in the orthorhombic phase [10]. In this case, the alternative tilting on the basis of the space group *Immm* was proposed in order to explain the orthorhombic structure. However, it is impossible to uniquely determine the O_2^- tilting state of the dumbbell from this space group. What is allowed by this space group is that the average angle of the O_2^- dumbbell against the *c*-axis should be zero. This means that we cannot exclude a possibility that the O_2^- dumbbell does not tilt even in the orthorhombic phase and/or a possibility of the mixture of those states making the average of tiling angle to be zero. Accordingly, further investigations on the detail lattice symmetry of RbO_2 at low temperatures including the O_2^- dumbbell tilting behavior are highly required to reveal the whole view of the anionogenic magnetism of superoxides including the possible formation of orbital ordering in RbO_2.

The absence of one-dimensional magnetic interaction in RbO_2 is quite interesting compared to the result on CsO_2. Furthermore, the system $(Cs_{1-x}Rb_x)O_2$ can be envisaged, where the disappearance of one-dimensional magnetic interaction indicated by the observation of broadening peak in CsO_2 can be tuned by varying the ratios of cation as observed in the spin-1/2 kagome lattice antiferromagnetic $(Rb_{1-x}Cs_x)_2Cu_3SnF_{12}$. By tuning the Cs content, the magnetic properties is changed from disordered state ($x<0,53$) to be ordered state ($x>0,53$) [138].

Chapter 5

Result and Discussion on Sodium Superoxide (NaO_2)

5.1. Magnetic Transition in NaO_2

Figure 5.1 (a) shows the result of magnetic susceptibility measurement of NaO_2. A Curie-Weiss analysis is fitted in the temperature range 250 to 300 K. The inverse magnetic susceptibility χ^{-1} (T) data obtained in a field of 1 kOe gives a magnetic moment μ_{eff}= 1.83 μ_B (μ_B is Bohr magneton) and Curie-Weiss temperature Θ_{CW}= -41.2 K. The low temperature susceptibility tail below 20 K is contribution from the impurity. The impurities such as NaOH and $NaNO_3$ were still found in sample batch synthesized using ammonia as a solvent [139].

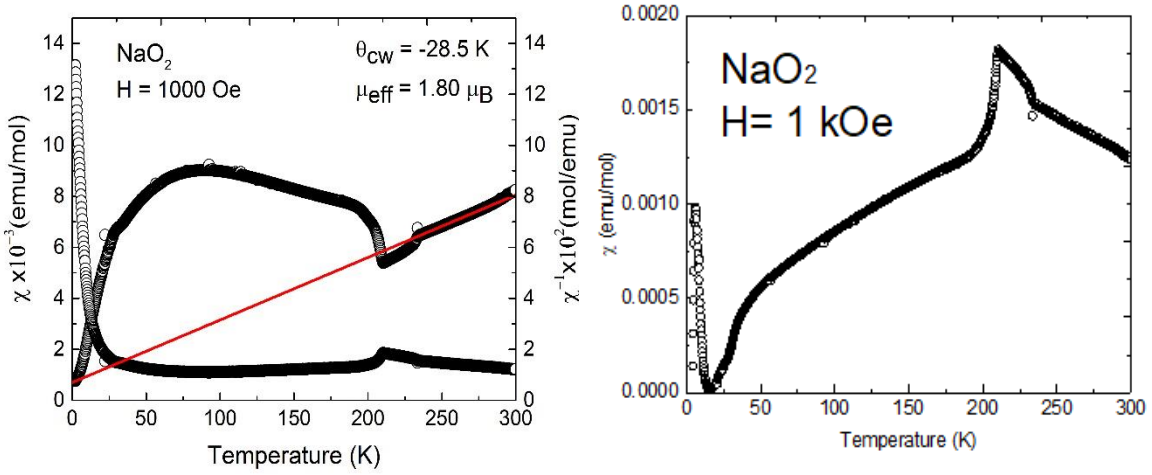

Figure 5.1. (a) Magnetic susceptibilty of NaO_2 synthesized using ammonia as a solvent (b) Magnetic susceptibility in NaO_2 with subtracting the impurity at low temperature (2-10 K). Such an abrupt change occurs at the temperature below about 40 K.

Figure 5.1 (b) shows the magnetic suceptibilty after subtracting the susceptibilty contributed by the impurity. The magnetic susceptibility in Figure 5.1 (b) is similar to that of other references [7, 12]. As explained in Chapter 2, we did the new synthesis method in order to suppress the impurity and obtain high purity of NaO_2 sample using liquid ammonia and

methylamine as the solvent. The result of magnetic susceptibility, as shown in Fig. 5.2, gave the similar result with the earlier reported magnetic susceptibility result in other references [7, 12] without any effort to subtract the contribution of impurity. The impurity remains but we can suppress it using the new synthesis method. The result of this magnetic susceptibility can be reproduced for other NaO_2 sample batches.

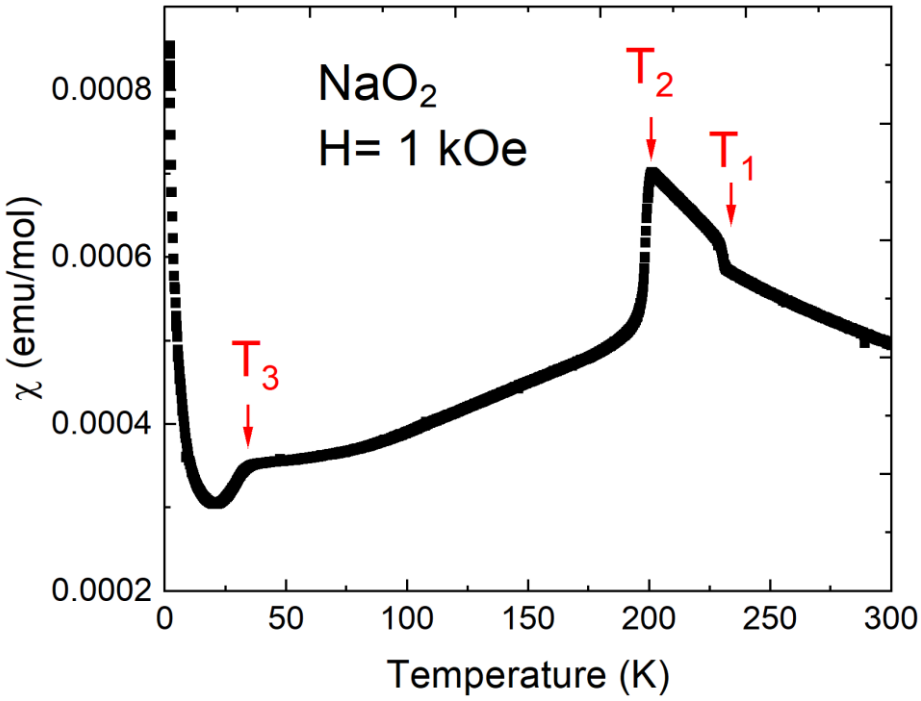

Figure 5.2. Magnetic susceptibilty of NaO_2 synthesized using methylamine and ammonia as the solvent.

The clear anomaly was observed at the temperature between 230 K and 200 K, defined as T_1 and T_2, respectively. These anomalies are consistent with the expected structural phase transition as discussed in Chapter 2. The magnetic susceptibility, χ, drops sharply at below 40 K, defined as T_3. The sudden change of susceptibility value toward zero is an indication of spin gap state as also observed in other spin gap systems, $NaTiSi_2O_6$ [140] and TiOCl [141]. Since M. Bösch et al reported that NaO_2 has some similarities to a one-dimensional spin gap system [16], the anomaly at the temperature below about 40 K might be corresponded to this phenomena.

5.2. μSR results in NaO_2

By using Heliox cryostat at DOLLY, PSI, we did not observe any signature of long-range magnetic order for NaO_2 down to 0.3 K as shown in Fig. 5.3.

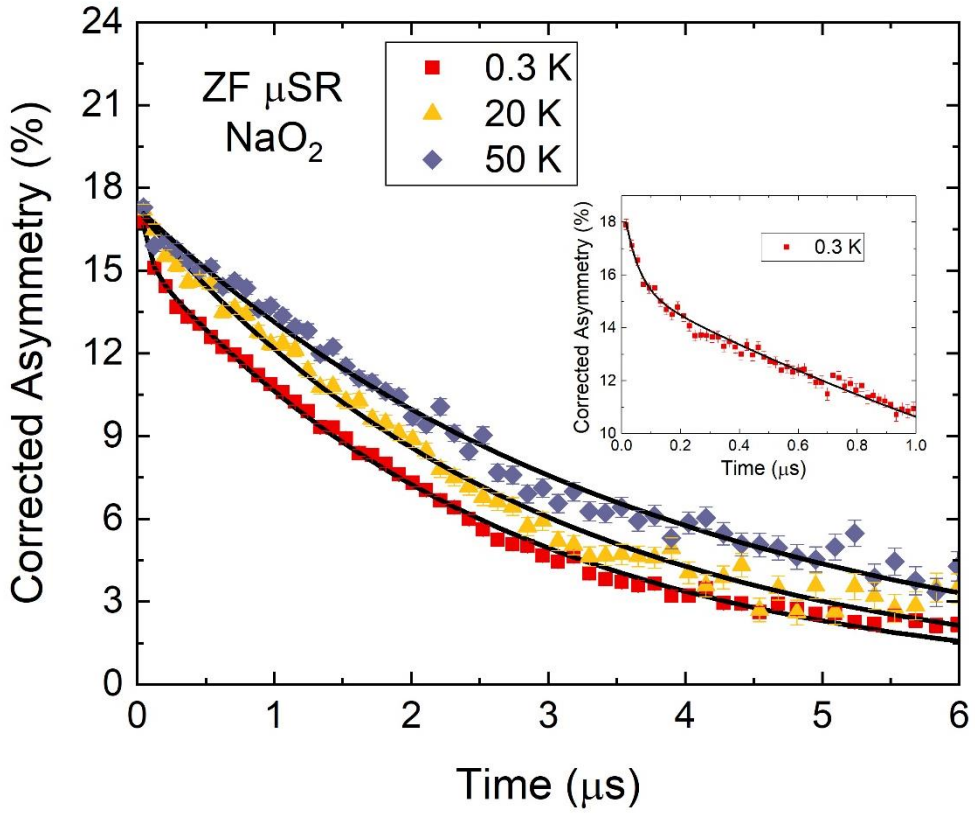

Figure 5.3. Time spectrum of NaO_2. No signature of muon spin precession is visible in NaO_2.

The absence of muon spin precession, which would be indicative of a spontaneous magnetic field, together with the observation that both high-and low-temperature spectra relax to the same value with negligible missing asymmetry, excludes the presence of long-range magnetic order. ZF muon spin polarization spectra at the temperature of 0.3 K shows a narrow dip in the initial time region as displayed in the inset in Fig. 5.3. It can be an evidence of the short-range magnetic order in the muon view. In the case of NaO_2, we can use a simple exponential function $\exp(-\lambda t)$ to describe the depolarization due to fluctuating electronic spin. There are many possibilities of the absence of muon spin precession. One of the possibilities is the formation of spin gap as also observed in other spin-gap materials [94, 142].

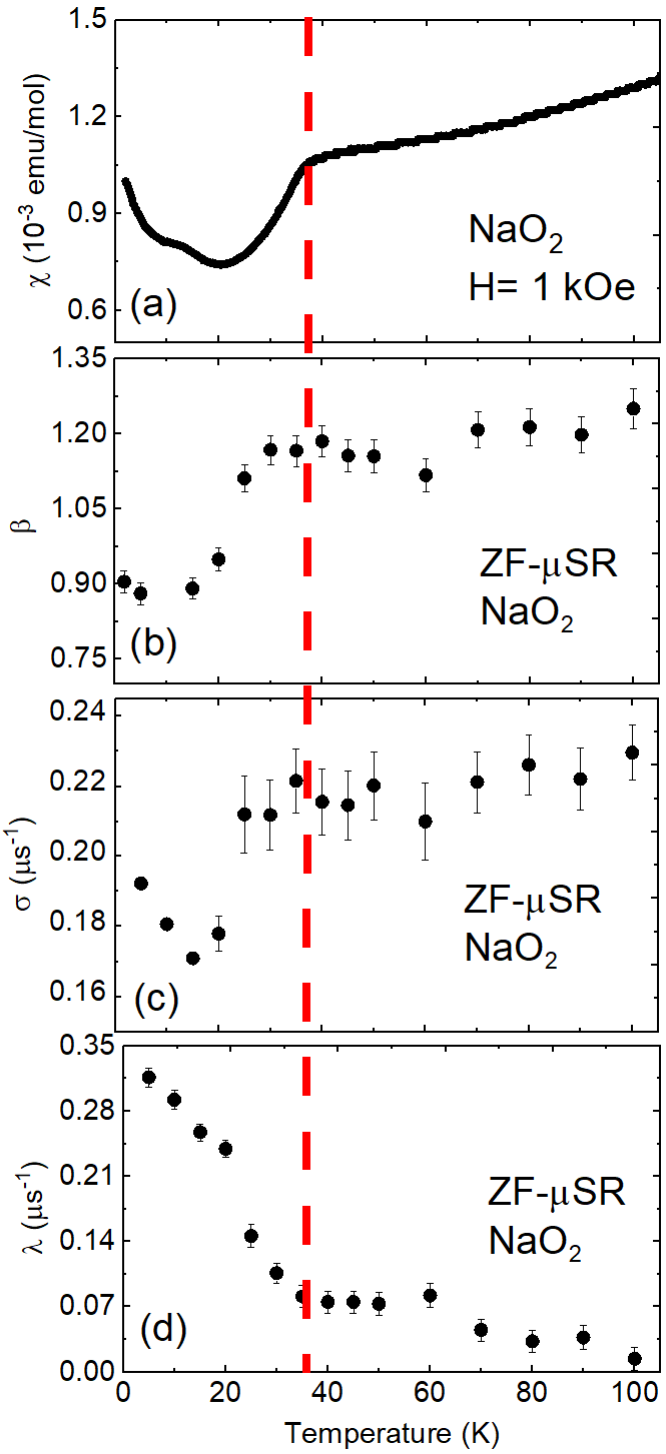

Figure 5.4. (a) Magnetic susceptibility of NaO_2 (b) The temperature dependence of the parameter β (β =1 corresponds to exponential relaxation, β =2 to an Gaussian relaxation and 1< β <2 is the value between exponential and Gaussian relaxation which is extracted from fitting the μSR data using Eq. (5.1)). Using an alternative fitting form (Eq.(5.2)) yields the temperature dependence of (c) the Gaussian relaxation rate, σ and (d) the exponential relaxation rate, λ.

Another μSR experiment was carried out using Variox cryostat at DOLLY, PSI and focused on collecting some data points around predicted spin-gap temperature, T_3. We measured the depolarization rate in ZF close to anomaly observed by magnetic susceptibility at ~40 K using μSR. In Fig. 5.4 (a), χ drops suddenly below T_3. In agreement with the anomaly in the magnetic susceptibility measurement, temperature dependence of the β, σ and λ display a clear anomaly around temperature below about T_3.

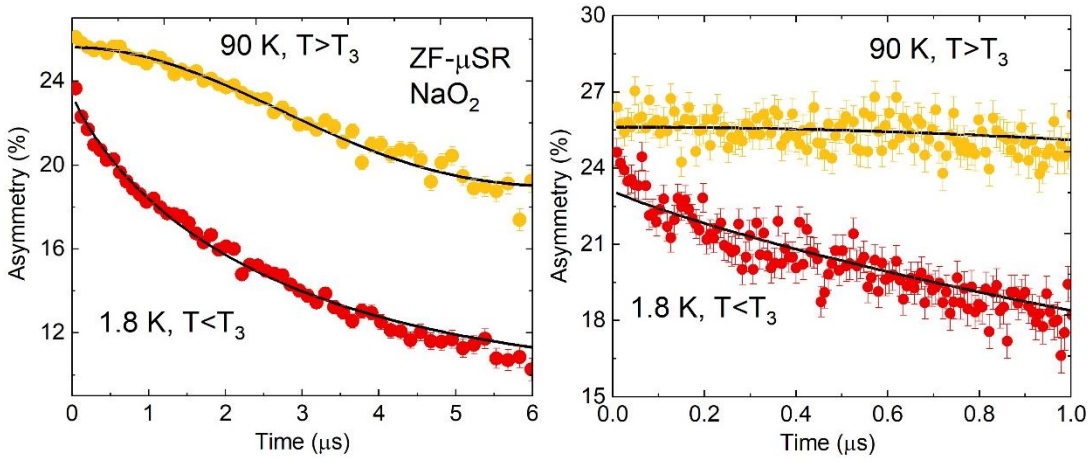

Figure 5.5. The time spectra of NaO_2 at 90 K (a temperature well above T_3) and 1.8 K (a temperature well below T_3) (a) within the long-time region up to 6 μsec and (b) within the short-time region up to 1 μsec.

In Fig. 5.5, we show ZF-μSR data for two-temperatures, one below and the other above T_3. Below T_3, the relaxation of the muon depolarization is well fitted by an exponential function, while above the transition the relaxation is in between exponential and Gaussian. We can follow this crossover in relaxation form by fitting our data over the complete temperature range using a variable lineshape:

$$A(t) = Ae^{-(\alpha t)^{\beta}} \quad \ldots\ldots\ldots\ldots (5.1)$$

where α is a temperature-dependent relaxation rate. The temperature dependence of our fitted values of β is shown in Fig. 5.4 (b) and indicates that the crossover happens between 10 and 30 K, which is somewhat below T_3.

There are two mechanisms which contribute to the muon relaxation, corresponding to the effect of the (1) fluctuating electronic spins (2) neighbouring nuclear spins. We can model this by fitting the muon data by using the following function:

$$A(t) = Ae^{-\lambda t}e^{-(\sigma t)^2} \ldots\ldots\ldots\ldots (5.2)$$

where the Gaussian relaxation arises from the random fields from surrounding nuclear dipoles (static over the muon lifetime) and the exponential relaxation is ascribed to the effect of the fluctuating electronic moments. Their temperature dependences are shown in Fig. 5.4 (c) and 5.4 (d). This expression assumes that the nuclear and electronic sources of relaxation are uncorrelated.

5.3. Discussion

Reports in the literature had suggested that it is rather difficult to synthesize NaO_2 with high purity [143]. Our new synthesis method using ammonia and methylamine as solvent could produce better purity of NaO_2 sample. Another synthesis method should be considered, but insufficient time prevented further exploration.

The magnetic susceptibility result on NaO_2 showed three anomalies indicated by T_1 ~230 K, T_2~200 K and T_3~40 K. T_1 and T_2 are in good agreement with the possible structural transition in NaO_2, while T_3 is predicted to be the spin-gap like transition. Spin gap system is nonmagnetic at the ground state. It is characterized by a finite energy gap between the singlet ground state and the triplet excited states. The observation of decreasing of the susceptibility value toward zero indicates that the ground state exhibits no magnetic field within the sample. The absence of LRO observed by μSR can be an evidence of the nonmagnetic ground state in NaO_2.

One suggested the possibility of formation of spin Peierls in NaO_2 [16]. If the spin-Peierls really exists in NaO_2, it is structurally and magnetically very different from other superoxides. The spin-Peierls system was proposed to have a spin-gap that consists of a S=1/2 antiferromagnetic spin chain with a spin-lattice coupling. Basically, the ground state structure of the spin-Peierls system is a stacking of singlet pairs along the chain. The ground state is non-magnetic because each singlet pair produces no magnetic field. In order to explore more about this possibility, X-ray measurements is needed for observing the degree of dimerization in the NaO_2 system. Our group is still trying to measure the low-temperature structure of this system.

A further changes of crystal structure should be exist below about spin-Peierls transition temperature (T_{SP}) due to the dimerization.

The combined use of μSR and magnetic susceptibility measurements demonstrate that these techniques can be used to explain the possible formation of spin-gap in NaO_2. Our ZF-μSR result indicates the crossover from exponential to Gaussian-like by increasing the temperature. This behavior was also observed in other systems which is a spin-gap system [144, 145]. Above T_3, the result of $\lambda \sim 0$ and $\sigma \sim 0.22$ μs^{-1}. The result $\lambda \sim 0$ at above T_3 indicates that the electronic spins are likely to be fluctuating rapidly (motional narrowing limit) due to μSR time window. Below T_3, the fitted value of σ decreases while λ increases. For the muon case, we observed a crossover from a regime in which the fluctuations are so fast that the relaxation is very weak (motionally narrowing limit) to a regime in which the correlation time of the electronic fluctuations is slow enough. The crossover is observed at a temperature somewhat lower than the predicted spin gap temperature, T_3. Thus the relaxation rate increases as the electronic fluctuation rate decreases, but the crossover to exponential relaxation only happens when the fluctuation rate is slow enough. It may be that the muon spin itself may perturb the local environment so as to break up and interact with nearby singlet pairs, causing some residual relaxation at low temperature [145]. Our μSR result can be a strong supporting data to elucidate the evidence of spin gap in NaO_2.

There are only limited materials which show a spin-Peierls transition. Usually, antiferromagnetic chains form three-dimensional order at low temperature due to interchain coupling. Only in very few materials is the spin-phonon coupling able to dominate the interchain spin-spin coupling and allow the formation of a spin-Peierls ground state. Examples of such materials are mainly organic systems, this is because such materials contain flat organic molecules in columnar stacks. The large interchain separation and weak van der Waals intermolecular interactions favour the dominance of magnetoelastic effects over interchain ordering. In contrast, the chains in corresponding inorganic materials are quite rigid due to the ionic bonding and only a single example of an inorganic spin-Peierls is known [145].

NMR measurement is highly desirable in order to check the formation of spin gap in NaO_2. In case of formation of spin gap from NMR measurement, a sharp decrease in T_1^{-1} must be found below spin gap temperature. Inelastic neutron scattering is also needed in order to observe whether there is a gap in the spin excitation spectrum.

Chapter 6
Summary

6.1. Summary of the current study

The work presented here focuses on synthesis and study of the structure and magnetic properties of alkali-metal superoxides. Chapter 1 presents a summary of previous studies on magnetic alkali-metal superoxides and gives an overview of which compound exist and what is known about their structural and electro-magnetic properties.

The high reactivity of alkali-metal superoxide to moisture in air requires sophisticated synthesis and handling procedures in controlled athmosphere. These procedures are described in detail in Chapter 2. Chapter 2 also describes the techniques that are used to characterize the chemical and physical properties of the synthesized compounds.

Chapter 3 presents a summary on structural and magnetic properties in CsO_2. The result of synchrotron XRD indicates a structural distortion of the unit cell from tetragonal to orthorombic structure at the temperature below about 150 K. The orthorombic structure remains down to 20 K. The dominant feature in the magnetic susceptibility of our polycrystalline CsO_2 is the broadening peak ~30 K that can be fitted well by Bonner-Fisher model which is a characteristic of 1D magnetic interaction. The small anomaly at the temperature below about 10 K is an indication of Neel temperature of this system. The formation of 3D long-range magnetic ordering (LRO) is directly observed by using μSR measurement performed at DOLLY, PSI. The magnetic transition temperature, T_N, estimated from the current μSR study was to be below 10 K, in good agreement with the anomaly observed from magnetic susceptibility measurement. Clearly, this LRO is not the magnetically induced one discussed in the NMR. We picked up the information from fitting result showing there were at least two muon-spin precession frequencies observed in the magnetically ordered state. Furthermore, two probable muon sites in the vicinity of the dumbbell oxygen were found. The magnetic volume fraction of LRO was estimated as 40%. This means that only 2/5 of the total volume is forming LRO and others do not. Based on the LF-μSR experiment, essentially static AF ordered state, that could coexist with moderate dynamic fluctuations, progressively develop below the magnetic ordering temperature. It is hard to judge the presence of TLL

phenomena from our μSR result since almost no change in relaxation rate at the expected TLL regime (15<T<40 K) measured on LF's 2.35 T and 4.7 T.

Chapter 4 presents a summary on structural and magnetic properties in RbO_2. XRD, magnetic susceptibility, high-field magnetization and muon-spin relaxation (μSR) were carried out to investigate lattice symmetry and magnetic properties on one of the series of superoxides, RbO_2. From the room temperature synchrotron XRD result, we confirmed that RbO_2 adopts the structure of CaC_2: space group *I/4mmm*. The structural transition from tetragonal to orthorhombic appeared below about 170 K. This was indicated by the split of the 200 peak to be the 200 and 020 ones. Two structural phase transitions around 170 and 100 K, defined as T_{S1} and T_{S2}, respectively, were observed in conjunction with the appearance of anomalies in the magnetic properties. The structural phase transition at the temperature around 100 K is an indication the transition from orthorhombic to the lower symmetry (monoclinic *I*112/*m*). It is indicated by splitting of some fundamental peaks e.g.: 101, 110 and 112 which could not observe in CsO_2. The sharp peak around 15 K, observed by magnetic susceptibility measurement, indicates the magnetic transition. ZF-and LF-μSR revealed the presence of the 3D long-range AF ordering below T_N∼15 K and that all spins on O_2^- dumbbells were frozen indicating the static spin. High-field magnetization study revealed that the magnetization value of RbO_2 is smaller than that of CsO_2 under external magnetic field 60 T.

Table 6.1 displays the comparison of current result and previous study of the structural phase transition in RbO_2 and CsO_2. The current study has a close agreement with the estimation of structural phase transition obtained by single crystal. Eventhough RbO_2 and CsO_2 are isostructural compound at room temperature, the magnetic properties is almost totally different. The current study revealed that differences in the magnetic properties between RbO_2 and CsO_2 are caused by changes in lattice symmetries. It is suggested that small changes in the orientation of the O_2^- dumbbells could cause change in those electromagnetic properties in superoxides since our XRD result predicted that the lattice symmetry of RbO_2 below T_{S2} is lower compared to that of CsO_2 at low temperature. The temperature dependence of χ in RbO_2 showing no appearance of a broad peak which was observed in CsO_2. This is a large difference from the case of CsO_2 in which the clear peak characterized by the low-dimensional magnetic interaction is observed around 30 K. We found that CsO_2 has a mixed state between the long-range ordered and dynamic fluctuating while RbO_2 shows almost static state whole though the sample. From the result of high-field magnetization, the saturated magnetization can be achieved by applying

field 60 T in CsO_2, while in order to reach the saturated magnetization in RbO_2, the higher applied field might be needed.

Table 6.1. Structural Transition of RbO_2 and CsO_2

Sample		Structure Transition	Temperature (K)	
			Previous Study	Current Study
CsO_2	Single Crystal	Tetragonal	190<T<383	
		Orthorhombic	9.6<T<190	
	Poly Crystal	Tetragonal	70 <T<300	150 <T<300
		Orthorhombic	T≤ 70	T<150
RbO_2	Single Crystal	Tetragonal	190<T<383	
		Orthorhombic	90<T<190	
		Monoclinic	T<90	
	Poly Crystal	Tetragonal		170<T<300
		Orthorhombic		100<T<170
		Monoclinic		T<100

Chapter 5 presents a summary on magnetic properties in NaO_2. The high purity NaO_2 can be synthesized by using solution method (oxidation of the metal dissolved in liquid ammonia and methylamine). The susceptibility measurement confirmed that the clear anomalies were observed at the temperature between 200 K and 230 K, defined as T_1 and T_2, respectively. These anomalies are consistent with the expected structural phase transition from previous report. The magnetic susceptibility, χ, drops sharply at below 40 K, defined as T_3. The sudden change of susceptibility value toward zero is an indication of spin gap state. The absence of muon spin precession down to 0.3 K excludes the presence of long-range magnetic order in NaO_2. Our ZF-μSR result indicates the crossover from exponential to Gaussian-like by increasing the temperature around T_3. In agreement with the anomaly in the magnetic susceptibility measurement, temperature dependence of the β, σ and λ display a clear anomaly around temperature below about T_3. The study of possible of spin-gap state in NaO_2 is needed to be explored by other experimental techniques e.g.: NMR.

With a decrease in the ionic radii, one can expect shorter interatomic/ intermolecular distance, hence stronger magnetic exchange interactions and perhaps higher ordering temperatures. Since the magnetic exchange interactions between oxygen molecules depends strongly on their distance as well as relative displacement, it must affect the magnetic exchange interaction for each system. It is important to remember that cooperative phenomena occur in alkali-metal superoxides where magnetic and molecular order is coupled to one another.

Eventhough those RbO_2, CsO_2 and NaO_2 belong to the same system, the magnetic properties is slightly different in the ground state. The study on p-electron magnetism in alkali-metal superoxides probed by μSR indicates the possibility of controlling the intermolecular interactions by changing the cation. In case of RbO_2, the system tends to situate more three-dimensional magnetic interaction. For CsO_2, it seems that there is a mixture in between N*é*el ordering and quantum condensed state which means that it locates near the border between the one-dimensional and three-dimensional magnetic correlations. On the other hand, NaO_2 is likely similar to the behavior of gapped quantum magnet. Because the ionic shape of alkali-metal is quite spherical and symmetric, it is highly expected that the driving force of the appearance of the lower lattice symmetry is due to changes in the orientation of O_2^- dumbbell axis.

6.2. Future work

This work is a preliminary study of AO_2 especially probed by μSR. The value of internal field obtained from experimental μSR result can be a reference for further study using calculation work. When muon-spin precession is observed, precession frequencies give us information of internal fields originating from the surrounding magnetic moments at muon sites. The muon-site itself is a very important parameter to study the hyperfine interaction between muon and electrons and to discuss ordered states of electronic spins in magnetic materials. These internal fields are estimated on the basis of the dipole-dipole interaction between muon spins and surrounding magnetic moments. Such combined studies involving experimental and computational techniques can allow us to discuss the spin structures and also estimation of magnetic moment.

The crystal structure in the ground state is essential to be clarified. Therefore, the further analysis in the XRD result on RbO_2 especially below T_{S2} will be continued. As well as RbO_2, the synchrotron XRD measurement in NaO_2 will be continued in order to check its low-temperature structure. From the view point of magnetic properties, other experimental techniques including NMR and inelastic neutron scattering are indispensable to reveal the possible formation of spin gap in NaO_2.

Beside that, in order to explain the exact atomic position including the tilting of dumbbell and spin structure, neutron diffraction measurement is very important to be performed. The estimation of magnetic exchange interaction is also inevitable in order to elucidate the magnetic interaction in AO_2 system.

References

[1] J. J. Attema, G. A. de Wijs, G. R. Blake, and R. A. de Groot, *J. Am. Chem. Soc* **127**, 16325-16328 (2005)

[2] M. Takahashi, P. Turek, Y. Nakazawa, M. Tamura, K. Nozawa, D. Shiomi, M. Ishikawa, and M. Kinoshita, *Physical Review Letter* **67** (1991)

[3] S. J. Blundell, P. A. Pattenden, F. L. Pratt, R. M. Valladares, T. Sugani, and W. Hayes, *Europhys. Lett.* **31**, 573 (1995)

[4] F. L. Pratt, P. J. Baker, S. J. Blundell, T. Lancaster, S. Ohira-Kawamura, C. Baines, Y. Shimizu, K. Kanoda, and I. Watanabe, *Nature* **471**, 612 (2011)

[5] K. Shimizu, K. Suhara, M. Ikumo, M. I. Eremets, and K. Amaya, *Nature* **395** (1998)

[6] H. G. Smith, R. M. Nicklow, L. J. Raubenheimer, and M. K. Wilkinson, *Journal of Apllied Physics* **37**, 1047-1049 (1966)

[7] S. D. Mahanti and A. U. Khan, *Solid State Communications* **18**, 159-162 (1976)

[8] M. Rosenfeld, M. Ziegler, and W. Känzig, *Helvetica Physica Acta* **51**, 298-320 (1978)

[9] W. Hesse, M. Jansen, and W. Schnick, *Prog. Solid. St. Chem* **19**, 47-110 (1989)

[10] S. Riyadi, B. Zhang, R.A. de Groot, A. Caretta, P. H. M. Van Loosdrecht, T. T. M. Palstra, and G. R. Blake, *Physical Review Letters* **108**, 217206 (2012)

[11] G. F. Carter and D. H. Templeton, *Contribution from the Dept. Of Chemistry and Radiation Lab* (1953)

[12] A. Zumsteg, M. Ziegler, W. Känzig, and M. Bösch, *Phys. Cond. Matter* **17**, 267-291 (1974)

[13] S. D. Mahanti and G.Kemeny, *Physical Review B* **20**, 2105-2117 (1979)

[14] S. S. Todd, *Minerals Thermodynamics Branch Region* **III**, 1229-1231 (1953)

[15] M. Labhart, D. Raoux, W. Känzig, and M. Bösch, *Physical Review B* **20**, 53-70 (1979)

[16] M. A. Bösch, M. E. Lines, and M. Labhart, *Physical Review Letters* **45**, 140-143 (1980)

[17] T. Knaflič, M. Klanjšek, A. Sans, P. Adler, M. Jansen, C. Felser, and D. Arčon, *Physical Review B* ***91****, 174419 (2015)*

[18] M. Klanjšek, D. Arčon, A. Sans, P. Adler, M. Jansen, and C. Felser, *Physical Review Letters* ***115****, 057205 (2015)*

[19] S. Blundell, *Magnetism in Condensed Matter*, Oxford University Press (2001)

[20] I. Tsukada, J. Takeya, T. Masuda, and K. Uchinokura, *Physical Review B* **62**, 10 (2000)

[21] F. M. Woodward, A. S. Albrecht, C. M. Wynn, and C. P. Landee, *Physical Review B*, 144412 (2002)

[22] M. Hase, I. Terasaki, and K. Uchinokura, *Physical Review Letter* **70**, 3651-3654 (1993)

[23] B. W. Lowett, S. J. Blundell, F. L. Pratt, Th. Jestadt, and W. Hayes, *Physical Review B* **61**, 12241-12248 (2000)

[24] J. W. Bray, H. R. Hart, L. V. Interrante, I.S. Jacobs, J.S. Kasper, G. D. Watkins, S. H. Wee, and J. C. Bonner, *Physical Review Letters* **35**, 744 (1975)

[25] I. Bose, *arXiv:cond-mat/0502019v1* (2008)

[26] B. Lake, D. A. Tennat, C. D. Frost, and S. E. Nagler, *Nature Materials* **4**, 329-334 (2005)

[27] M. Hagiwara, H. Tsujii, C. R. Rotundu, B. Andraka, Y. Takano, N. Tateiwa, T. C. Kobayashi, T. Suzuki, and S. Suga, *Physical Review Letters* **96**, 147203 (2006)

[28] T. Isono, T. Terashima, K. Miyagawa, K. Kanoda, and S. Uji, *Nature Communications* **7**, 13494 (2016)

[29] M. J. Harris, S. T. Bramwell,. F. McMorrow, T. Zeiske, and K. W. Godfrey, *Phys. Rev. Lett.* **79**, 2554 (1997)

[30] Y. J. Uemura, T. Yamazaki, D. R. Harshman, M. Senba, and E. J. Ansaldo, *Phys. Rev. B 31*, 546 (1985)

[31] M. Faraday, *Experimental Researches in Electricity*, Series **XXV** Vol. 3 (Taylor and Francis, London, 1855).

[32] G. D. Morris, J. H. Brewer, S. R. Dunsiger and M. Montour, *Hyperfine Interactions* **104**, 381-385 (1997)

[33] I. N. Goncharenko, O. L. Makarova, and L. Ulivi, *Phys. Rev. Lett.* **93**, 055502 (2004).

[34] F. Gorelli, M. Santoro, L. Ulivi, and M. Hanfland, *Phys. Rev. B* **65,** 172106 (2002)

[35] M. F. Collins, *Proc. Phys. Soc. London* **89**, 415 (1966)

[36] V. Storchak, B. F. Kirillov, A. V. Pirogov, V. N. Duginov, V. G. Grebinnik, V. G. Ol'shevsky, A. B. Lazarev, V. Yu. Pomyakushin, S. N. Shilov, and V. A. Zhukov, *Hyperfine Interactions* **85**, 345-350 (1994)

[37] S. Pilla, J. A. Hamida, K. A. Muttalib, and N. S. Sullivan, *Phys. Rev. B* **77,** 224108 (2008)

[38] C. Uyeda, K. Sugiyama and M. Date, *Journal of the Physical Society of Japan* **54**, 1107-1115 (1985)

[39] T. Nomura, Y. H. Matsuda, S. Takeyama, A. Matsuo, and K. Kindo, *Physical Review Letters* **112**, 247201 (2014)

[40] S. Kitagawa, *Physics* **7**, 63 (2014)

[41] M. Obata, M. Nakamura, I. Hamada, and T. Oda, *Journal of the Physical Society of Japan* **84**, 024715 (2015)

[42] T. Ishikawa, K. Mukai, and K. Shimizu, *High Pressure Research* **32**, 4 (2012)

[43] I. Solovyev, *New Journal of Physics* **10**, 013035 (2008)

[44] M. Kim, *PhD Thesis* (2014)

[45] S. C. Abrahams, R. L. Collins, and W. N. Lipscomb, *Acta Cryst* **4**:15, 1951.

[46] E.R. Ylvisaker, *PhD Thesis* (2008)

[47] J. Winterlik, G. H. Fecher, C. A. Jenkins, S. Medvedev, and C. Felser, *Physical Review B* **79**, 214410 (2009)

[48] M. Hayyan, M. A. Hashim, and M. Alnashef, *Chemical Review* **116**, 3028-3085 (2016)

[49] E. W. Neuman, *J. Chem. Phys* **2**, 31 (1934)

[50] L. Pauling, *Trends Biochem. Sci* **4**, N270 (1969)

[51] https://www.askiitians.com/iit-jee-s-and-p-block-elements/alkali-metals/

[52] R. Kovacik, P. Werner, K. Dymkowski, and C. Ederer, *Phys. Rev. Lett* **86**, 075130 (2012)

[53] R. Kovacik and C. Ederer, *Phys. Rev. B* **80**, 140411 (2009)

[54] E. R. Ylvisaker, R. R. P. Singh, and W. E. Pickett, *Phys. Rev. B* **81**, 180405 (2010)

[55] O. Arcelus, N. Suaud, N. A. Katcho, and J. Carrasco, *The Journal of Chemical Physics* **146**, 184301 (2017)

[56] M. Kim and B. I. Min, *Physical Review B* **89**, 121106 (2014)

[57] K. I. Kugel and D. I. Khomskii, *Sov. Phys.-Usp* **25**, 231 (1982)

[58] G. F. Carter and D. H. Templeton, J. Am. Chem. Soc. 75, 5247 (1953)

[59] S. K. Ghosh and P. K. Chattaraj, *Concepts and Methods in Modern Theoretical Chemisty, Taylor and Francis Group* (2013)

[60] D. H. Templeton and C. H. Dauben, *J. Am. Chem. Soc.* **72**, 2251 (1950)

[61] M. E. Lines and M. A. Bosch, *Phys. Rev. B* **23**, 263 (1981)

[62] A.K. Nandy, P. Mahadevan, P. Sen, and D. D. Sarma, *Phys. Rev. Lett.* **105**, 056403 (2010)

[63] M. Kim, B. H. Kim, H. C. Choi, and B. I. Min, *Phys. Rev. B* **81**, 100409(R) (2010)

[64] M. Miyajima, F. Astuti, T. Kakuto, A. Matsuo, D. P. Sari, R. Asih. K. Okunishi, T. Nakano, Y. Nozue, K. Kindo, I. Watanabe, and T. Kambe, *Journal of the Physical Society of Japan* **87**, 063704 (2018)

[65] R. B. Griffiths, *Phys. Rev* **133**, A768 (1964)

[66] C. Berthier, L. P. Lévy, and G. Martinez, *High Magnetic Field "Applications in Condensed Matter Physics and Sprectroscopy"*, (Springer, Paris 2002)

[67] T. Matsushita, N. Hori, S. Takata,N. Wada, N. Amaya, and Y. Hosokoshi, *Phys. Rev. B* **95**, 020408(R) (2017)

[68] S. Simizu, J.-Y. Chen, and S. A. Friedberg, *Journal of Applied Physics* **55**, 2398 (1984)

[69] E. E. Kaul, H. Rosner, V. Yusankhai, J. Siscelschmidt, R. V. Shpanchenko, and C. Geibe, *Phys. Rev. B* **67**, 174417 (2003)

[70] M. Herak, A. Zorko, M. Pregelj, O. Zaharko, G. Posnjak, Z. Jagličič, A. Potočnik, H. Luetkens, J. van Tol, A. Ozarowski, H. Berger, and D. *Ar*čon, *Physical Review B **87**, 104413 (2013)*

[71] P. Manuel, D. T. Adroja, P. Lindgard, A. D. Hillier, P. D. Battle, W. -J. Som, and M.-H. Whangbo, *Phys. Rev. B* **84**, 174430 (2011)

[72] N. D. Mermin and H. Wagner, *Phys. Rev. Lett.* **17**, 1133 (1966)

[73] S. Tomonaga, *Prog. Theor. Phys.* **5**, 544 (1950)

[74] J. M. Luttinger, *J. Math. Phys.* **15**, 609 (1963)

[75] F. D. M. Haldane, *Phys. Rev. Lett.* **45**, 1358 (1980)

[76] M. Hagiwara, H. Tsujii, C. R. Rotundu, B. Andraka, Y. Takano, T. Suzuki, and S. Suga, *Modern Physics Letter B* **21**, 965-976 (2007)

[77] N. Kawakami, *AAPPS Bulletin* **16** (2006)

[78] J. S. Lord, I. McKenzie, P. J. Baker, S. J. Blundell, S. P. Cottrell, S. R. Giblin, J. Good, A. D. Hillier, B. H. Holsman, P. J. C. King, T. Lancaster, R. Mitchell, J. B. Nightingale, M. Owczarkowski, S. Poli, F. L. Pratt, N. J. Rhodes, R. Scheuermann, and Z. Salman, *Rev. Sci. Instrum.* **82**, 073904 (2011)

[79] N. Ishimura and H. Shiba, *Prog. Theor. Phys.* **57**, 1862 (1977)

[80] J. Feldman J. Magnen, V Rivasseau, E. Trubowitz, *Europhys. Lett.* **24**, 437 (1993)

[81] T. Giamarchi, Quantum Physics in One Dimension (Oxford Univesity Press, Oxford 2004)

[82] G. Morandi, P. Sodano, A. Tagliacozzo, and V. Tognetti, *Field Theories for Low-Dimensional Condensed Matter Physics "Spin Systems and Strongly Correlated Electrons"*, (Springer series in Solid State Physics, New York 2000)

[83] I. V. Solovyev, Z. V. Pchelkina, and V. V. Mazurenko, *CrystEngComm* **16**, 522 (2014)

[84] M. Jansen, R. Hagenmayer, and N. Korber, *C. R. Acad. Sci., Ser. Iic: Chim* **2**, 591 (1999)

[85] J. Winterlik, G. H. Fecher, and C. Felser, *J. Am. Chem. Soc* **129**, 6990-6991 (2007)

[86] A. Yaouanc and P. D. de R*éotier, "Muon Spin Rotation, Relaxation, and Resonance; Applications to Condensed Matter, (New York: Oxford University Press Inc., 2011)*

[87] T. Prokscha, *Muon Properties and Muon Production*. *https://indico.psi.ch*

[88] M. T. F. Telling et al., *Physics Procedia* **30** (2012) 86-90

[89] Jeff E. Sonier, Muon Spin Rotation/ Relaxation/ Resonance (μSR). http://www.chem.ubc.ca

[90] S. Sanna, G. Allodi, G. Concas, A. D. Hillier, and R. De Renzi, *Phys. Rev. Lett.* **20**, 207001 (2004)

[91] A. T. Savici, Y. Fudamoto, I. M. Gat, T. Ito, M. I. Larkin, Y. J. Uemura, G. M. Luke, K. M. Kojima, Y. S. Lee, M. A. Kastner, R. J. Birgeneau, and K. Yamada, *Phys. Rev. B* **66**, 014524 (2002)

[92] J. S. Möller, T. Lancaster, S. J. Blundell, F. L. Pratt, P. J. Baker, F. Xiao, R. C. William, W. Hayes, M. M. Turnbull, and C. P. Landee, *Phys. Rev. B* **95**, 020402 (R) (2017)

[93] B. W. Lovett, S. J. Blundell, F. L. Pratt, T. Jestadt, W. Hayes, S. Tagaki, and M. Kurmoo, *Phys. Rev. B.* **61**, 12241 (2000)

[94] P. J. Baker, S. J. Blundell, F. L. Pratt, T. Lancaster, M. L. Brooks, W. Hayes, M. Isobe, Y. Ueda, M. Hoinkis, M. Sing, M. Klemm, S. Horn, and R. Claessen, *Phys. Rev. B* **75**, 094404 (2007)

[95] K. Wohlfeld, M. Daghofer, and A. M. Oles, *EPL* **96**, 27001 (2011)

[96] J. P. Perdew, K. Burke, and M. Ernzerhof, *Phys. Rev. Lett.* **77**, 3865 (1996)

[97] www.castep.org

[98] http://link.aps.org/supplemental/10.1103/PhysRevLett.108.217206

[99] S. E. Stephanou, W. H. Schechter, W. J. Argersinger, and J. Kleinberg, *Journal of the American Chemical Society* **71**, 1819 (1949)

[100] S. Giriyapura, *PhD Thesis* (2012)

[101] B. H. Toby, *Journal of Applied Crystallography* **34**, 210 (2001)

[102] O. Yildirim, *PhD Thesis* (2015)

[103] https://www.psi.ch/smus/dolly

[104] F. L. Pratt, *Physics B* **710**, 289-290 (2000)

[105] https://www.isis.stfc.ac.uk/Pages/Argus.aspx

[106] https://www.isis.stfc.ac.uk/Pages/Hifi.aspx

[107] P. J. Baker, T. Lancaster, S. J. Blundell, W. Hayes, F. L. Pratt, M. Itoh, S. Kuroiwa, and J. Akimitsu, *J. Phys.: Condens. Matter* **20**, 465203 (2008)

[108] F. Bernardini, P. Bonfa, S. Massidda, and R. De Renzi, *Phys. Rev. B* **87**, 115148 (2013)

[109] J. S. Möller, P. Bonfa, D. Ceresoli, F. Bernardini, and S. J. Blundell, *Physica Scripta* **88**, 068510 (2013)

[110] P. Bonfa, *J. of Phys.: Cond. Matter* **25**, 505901 (2015)

[111] J. H. Brewer, S. R. Kreitzman, D. R. Noakes, E. J. Ansaldo, D. R. Harshman, and R. Keitel, *Phys Rev. B* **33**, 7813 (R) (1986)

[112] D. R. Noakes, E. J. Ansaldo, S. R. Kreitzman, and G. M. Luke, *J. of Appl. Phys.and Chem. of Solids* **54**, 785 (1993)

[113] D. R. Noakes, E. J. Ansaldo, and G. M. Luke, *J. of Appl. Phys.* **73**, 5666 (1993)

[114] J. H. Brewer, R. F. Kiefl, J. F. Carolan, P. Dosanjh, and W. N. Hardy, *Hyp. Int.* **63**, 177 (1990)

[115] G. Kresse and J. Hafner, *Phys. Rev. B* **47**, 558 (1993); ibid. **49**, 14 251 (1994), *J. Phys.: Condens. Matt.* **6**, 8245 (1994)

[116] F. Giustino, "Material Modelling using Density Functional Theory: Properties and Prediction", Oxford: OUP Oxford (2014)

[117] B. B. Laird, R. B. Ross, and T. Ziegler, " Density-Functional Methods in Chemistry: An Overview", Washington DC: American Physical Society (1996)

[118] B. Nachumi, Y. Fudamoto, A. Keren, K. M. Kojima, M. Larkin, N. Ichikawa, M. Goto, H. Takagi, S. Uchida, M. K. Crawford, E. M. McCarron, D. E. MacLaughlin, and R. H. Heffner, *Phys. Rev. B* **58**, 8760 (1998)

[119] S. Riyadi, S. Giriyapura, R. A. de Groot, A. Caretta, P. H. M. Van Loosdrecht, T. T. M. Palstra, and G. R. Blake, *Chem. Mater.* **23**, 1578-1586 (2011)

[120] T. Ami, M. K. Crawford, and R. L. Harlow, *Phys. Rev. B* **51**, 5994-6001 (1995)

[121] Z. He and Y. Ueda, Phys. Rev. B 77, 052402 (2008)

[122] I. B. Rutel, S. A. Zyvagin, J. S. Brooks, J. Krzystek, P. Kuhns, A. P. Reyes, E. Jobiliong, B. H. Ward, J. A. Schlueter, R. W. Winter, and G. L. Gard, *Phys. Rev. B* **67**, 214417 (2003)

[123] B. C. Keith, C. P. Landee, T. Valleau, M. M. Turnbull, and N. Harrison, *Phys. Rev. B* **84**, 104442 (2011)

[124] R. Feyerherm, S. Abens, D. Gunther, T. Ishida, M. Mei*ßner*, M. Meschke, T. Nogami, and M. Steiner, *Journal of Physics: Condensed Matter* **12**, 8495 (2000)

[125] J. C. Bonner and M. E. Fisher, *Phys. Rev.* **135**, A640 (1964)

[126] P. D.C. Dietzel, R. H. Kremer, and M. Jansen, *J. Am. Chem. Soc.* **126**, 4689 (2004)

[127] M. Mansson, K. Prsa, J. Sugiyama, H. Nozaki, A. Amato, K. Omura, S. Kimura, and M. Hagiwara, *Physics Procedia* **30**, 146-150 (2012)

[128] M. I. Darby, *Brit. J. Appl. Phys.* **18**, 1415-1417 (1967)

[129] B. A. Frandsen, L. Liu, S. C. Cheung, Z. Guguchia, R. Khasanov, E. Morenzoni et.al, *Nature Communications* **7**, 12519 (2016)

[130] Y. Kono, T. Sakakibara, C. P. Aoyama, C. Hotta, M. M. Turnbull, C. P. Landee, and Y. Takano, *Phys. Rev Lett.* **114**, 037202 (2015)

[131] Dudarev et al., *Sov. Phys. Crystallogr. (English Translation)* **18**, 477 (1974)

[132] P. D. C. Dietzel, R. H. Kremer, and M. Jansen, *J. Am. Chem. Soc* **126**, 4689 (2004)

[133] A.J. Steele, T. Lancaster, S. J. Blundell, P. J. Baker, F. L. Pratt, C. Baines, M. M. Corner, H. I. Southerland, J. L. Manson, J. A. Schlueter, *Phys. Rev. B* **84**, 064412 (2011).

[134] M. F. Collins, Magnetic critical scattering, Oxford Univ. Press, Oxford (1989).

[135] T. Saito, A. Oosawa, T. Goto, T. Suzuki, and I. Watanabe, *Phys. Rev. B* **74**, 134423 (2006).

[136] Y. Takabayashi, A. Y. Ganin, M. J. Rosseinsky, and K. Prassides, Chem. Commun., 870-872 (2007)

[137] Z. He, T. Taniyama, and M. Itoh, *Phys Rev. B* **73**, 212406 (2006)

[138] K. Katayama, N. Kurita, and H. Tanaka, *Phys. Rev. B* **91**, 214429 (2015)

[139] M. Miyajima, ICMM poster (2016)

[140] M. Isobe, E. Ninomiya, A. N. Vasil'ev, and Y. Ueda, *J. Phys. Soc. Jpn.* **71**, 1423 (2002).

[141] A. Seidel, C. A. Marianetti, F. C. Chou, G. Ceder, and P.A. Lee, *Phys. Rev. B* **67**, 020405 (R) (2002)

[142] Y. Fudamoto, K. M. Kojima, M. I. Larkin, G. M. Luke, J. Merrin, B. Nachumi, Y. J. Uemura, M. Isobe, and Y. Ueda, *Phys. Rev. Lett.* **83**, 3301 (1999)

[143] S. E. Stephanou, W. H. Schechter, W. J. Argersinger, and J. Kleinberg, *Journal of the American Chemical Society* **71**, 1819 (1949)

[144] Th. Jestadt, R. I. Bewley, S. J. Blundell, W. Hayes, B. W. Lowett, F. L. Pratt, and R. C. C. Ward, *J. Phys.: Condens. Matter* **10**, L259-L263 (1998)

[145] S. J. Blundell, F. L. Pratt, P. A. Pattenden, M. Kurmoo, K. H. Chow, S. Takagi, Th. Jestadt, and W. Hayes, *J. Phys.: Condens. Matter* **9**, L119-L124 (1997)